Wave phenomena in one-dimensional space or time varying media

Ioannis-Markos Kiorpelidis

COLLEGE SCIENCES DOCTORAL DE L'INGENIERIE PAYS DE LA LOIRE ET DES SYSTEMES

Le Mans Université

HELLENIC REPUBLIC
National and Kapodistrian University of Athens
EST. 1837

THESE DE DOCTORAT

DE
LE MANS UNIVERSITE
UNIVERSITÉ NATIONALE ET CAPODISTRIANNE D'ATHÈNES
SOUS LE SCEAU DE
LA COMUE ANGERS – LE MANS

ECOLE DOCTORALE N° 602
Sciences de l'Ingénierie et des Systèmes
Spécialité : Acoustique
Thèse n° 2023LEMA1032

Par
Ioannis-Markos KIORPELIDIS

Wave phenomena in one-dimensional space or time varying media

Thèse présentée et soutenue à Athènes, le 18 Decémbre 2023
Unité de recherche : UMR CNRS 6613, Laboratoire d'Acoustique de l'Université du Mans (LAUM)

Rapporteurs avant soutenance :

Phivos Mavropoulos	Professeur, Université Nationale et Capodistrianne d'Athènes
Aris Moustakas	Professeur Agrègè, Université Nationale et Capodistrianne d'Athènes

Composition du Jury :

Président :	Fotios Diakonos	Professeur, Université Nationale et Capodistrianne d'Athènes
Examinateurs :	Nikolaos Stefanou	Professeur, Université Nationale et Capodistrianne d'Athènes
	Efstathios Stiliaris	Professeur, Université Nationale et Capodistrianne d'Athènes
	Vassos Achilleos	Chercheur CNRS, Le Mans Université
	Konstantinos Makris	Professeur Agrègè, Université de Crète
Dir. de thèse :	Vincent Pagneux	Directeur de Recherche CNRS, Le Mans Université
	Fotios Diakonos	Professeur, Université Nationale et Capodistrianne d'Athènes
Co-dir. de thèse :	Georgios Theicharis	Chercheur CNRS, Le Mans Université

To Eirini

Abstract

The interaction of waves with media possessing spatial or/and temporal fluctuations leads to interesting phenomenology. Within this framework, in the present thesis four wave phenomena are studied: two occurring in spatially-varying media and two in time-varying media. We begin by exploring wave scattering by a finite spatially-periodic setup that is subject to perturbation. Our focus is on perfect transmission resonances (PTRs) and we develop a method for preserving them under asymmetric perturbations. The performed analysis reveals a pairwise connection between PTRs of a spatially-periodic scattering setup with mirror symmetric cells. In the same context of spatially varying media, we compute the localization length of the topological edge modes that are supported in a mechanical mass-spring chain possessing random fluctuations of its stiffness parameters. In the presence of strong chiral disorder the localization length diverges, implying a topological phase transition that is induced purely by disorder. As a next step we consider the case where the couplings of the mechanical mass-spring chain vary with time in a deterministic way. Then this time-varying system can serve as a platform for transferring a topological edge mode. Going beyond the adiabatic limit, we design a protocol for the time-varying couplings that results in a fast and robust transfer and even more leads to amplification of the transferred edge mode. To shed light into the phenomenon of amplification in a time-varying platform, we explore the propagation of a wave in a medium with time-periodic refractive index and with wave dynamics governed by the Mathieu equation. The wave exhibits transient amplification due to the non normal nature of the propagator matrix and we provide numerical evidence that the global amplifying features are provided merely by the monodromy matrix.

Acknowledgments

First and foremost, I would like to thank my supervisors Profs. Fotios Diakonos, Vincent Pagneux, and Georgios Theocharis. I've had the privilege of knowing them since my undergraduate studies and receiving their guidance throughout these years. They have shown me endless support and patience during this journey and their influence goes beyond my scientific growth and reaches into my personal development. I am deeply grateful for them.

I would also like to thank Prof. Nikolaos Bakas, not only for the warm hospitality and care that he showed me at the University of Ioannina, but even more for his outstanding scientific mentorship. I consider him my fourth supervisor.

I want to thank as well Prof. Vassos Achilleos for our wonderful collaborations and Prof. Olivier Richoux who has always been more than kind and helpful to me. I also thank Profs. Dimitrios Frantzeskakis and Pierre Delplace, members of my CSI committee, who were following my progress with attention and always encouraged me.

Further, I want to thank Dr. Nikolaos Palaiodimopoulos and Dr. Panayiotis Kalozoumis for their guidance in academia and for their good friendship all of these years. I also thank Dr. Rajesh Chaunsali and Dr. Ioannis Brouzos for the valuable collaborations we had at the early stages of this thesis.

I would like to thank Mrs Eleni Holeva for drafting the cotutelle contract and helping me numerous times. She had a key role and without her this thesis would have never been made.

Additionally, I want to thank Giannis and Tolis for their hospitality and the fun we had in Le Mans and also Michalis, Alexandros, Nathan and Eugenios for all the good times we shared in Ioannina. I thank my friends in Lefkada: Konstantina, Makis, Vaggelis, Christos, Dafni and Mariza for all the good moments we had the past few years and especially Stella for all the wonderful memories. A special thanks goes to my friends Kostas and Panagiotis because our friendship remains strong, no matter how much time passes or how far apart we are.

Concluding, I would like to thank my family: my mother Elsa, my father Giorgos, my sister Eirini, my aunt Loula and my uncle Giorgos, for their love and support and for always being there for me. Lastly, I want to thank my partner in life Eirini Chorti, for so many reasons that it's really difficult to put them into words; thank you for everything, this thesis is dedicated to you.

Contents

Introduction **1**

1 Perfect transmission resonances of perturbed scattering systems **8**

1.1 Introduction . . . 8

1.2 Scattering by a periodic system with mirror symmetric cells . . . 8

1.2.1 Perfect transmission resonances . . . 10

1.2.2 Implications of mirror symmetry . . . 11

1.3 Perturbing the potential . . . 12

1.3.1 Perturbation expansion . . . 12

1.3.2 Preserving all PTRs . . . 14

1.3.3 Preserving one PTR . . . 15

1.4 Particular classes of perturbations that preserve two PTRs . . . 16

1.4.1 Perturbation at the centers of the cells . . . 16

1.4.2 Perturbation at the edges of the cells . . . 18

1.5 Concluding remarks . . . 19

2 Localization properties of a disordered dimer chain **20**

2.1 Introduction . . . 20

2.2 Topological features of a dimer chain . . . 21

2.3 Finite dimer chain . . . 25

2.3.1 Equations of motion . . . 25

2.3.2 Eigenanalysis . . . 26

2.4 Disorder analysis . . . 28

2.4.1 Chiral disorder . . . 28

2.4.2 Non-correlated disorder . . . 29

2.5 Localization properties . . . 30

2.5.1 Chiral disorder . . . 31

2.5.2 Non-correlated disorder . . . 36

2.6 Concluding remarks . . . 37

3 State transfer in periodic time-varying mechanical lattices 38
3.1 Introduction . . . 38
3.2 Finite dimer chain with odd masses . . . 38
3.2.1 Small vibrations . . . 39
3.2.2 Eigenanalysis . . . 40
3.3 Basics for state transfer . . . 41
3.3.1 Energy . . . 41
3.3.2 Fidelity . . . 42
3.3.3 Adiabatic invariant . . . 43
3.4 Transfer protocols . . . 44
3.4.1 Constrained protocols . . . 44
3.4.2 Non-constrained protocols . . . 48
3.4.3 Disorder analysis . . . 51
3.5 Energy amplification . . . 53
3.6 Concluding remarks . . . 54

4 Transient amplification for the Mathieu equation without parametric instability 55
4.1 Introduction . . . 55
4.2 Wave propagation in Floquet media . . . 55
4.2.1 Unstable and stable solutions of the Mathieu equation . . . 56
4.2.2 Review of Mathieu equation . . . 57
4.3 Measuring the transient amplification . . . 59
4.3.1 Choice of variables . . . 60
4.3.2 Choice of measure . . . 62
4.3.3 Pseudospectrum analysis . . . 64
4.3.4 Petermann factors . . . 66
4.4 Impact of the initial time τ_0 . . . 67
4.4.1 Maximum transient amplification . . . 69
4.5 Concluding remarks . . . 71

5 Summary and perspectives 72

A Mirror symmetric cells 76
A.1 Centers of the cells . . . 76
A.2 Edges of the cells . . . 79

B Numerical computation of the localization length 81

C Adiabatic state transfer 83

D Approximation and closed form formula **87**

Bibliography **90**

Introduction

A. Some features of spatial media

Exploring how waves interact with media that display structures in space, not only advances technology but also deepens our understanding for the natural world. This interaction between waves and spatial media gives rise to a wide and diverse range of phenomena. In the first part of this thesis we focus our attention on perfect transmission resonances (PTRs) and on wave localization in disordered topological lattices.

A1. Periodic media and perfect transmission resonances

The investigation of the wave behavior in periodic media has certainly attracted great interest in physics over the years. This research contains the study of the wave propagation in infinite periodic media [1] and the wave scattering by finite periodic ones [2]. It is known that the energies for which the wave propagation is allowed in a one-dimensional infinite periodic medium form bands that are separated by gaps. Namely, the energy spectrum shows a band structure form [3] (see Fig. 1(a) for an example). Fingerprints of a band structure form can be observed in the transmission spectrum of a one-dimensional finite periodic medium [4, 5]. Specifically, for certain energies of the wave that scatters by such a medium the transmission coefficient is close to zero (transmission gaps) and for certain other energies the transmission coefficient is close to one (transmission bands). The positions of transmission bands (gaps) match with the corresponding energy levels for which the wave propagation is allowed (prohibited) in the corresponding infinite medium [6]. Moreover, within each of these transmission bands the transmission coefficient becomes exactly equal to 1 at least $N-1$ times (N is the number of the cells that comprise the finite periodic medium) [2,4,5,7] (see Fig. 1(b)).

The case of transmission equal to one is known as a perfect transmission resonance (PTR). Specifically, a PTR refers to the following situation

PTR: A wave (with real wave number k) perfectly transmits through a medium that it is incident to.

The appearance of PTRs is not limited in periodic media since aperiodic scattering setups that possess global mirror symmetry usually support PTRs as well [8–11]. Furthermore, it has been

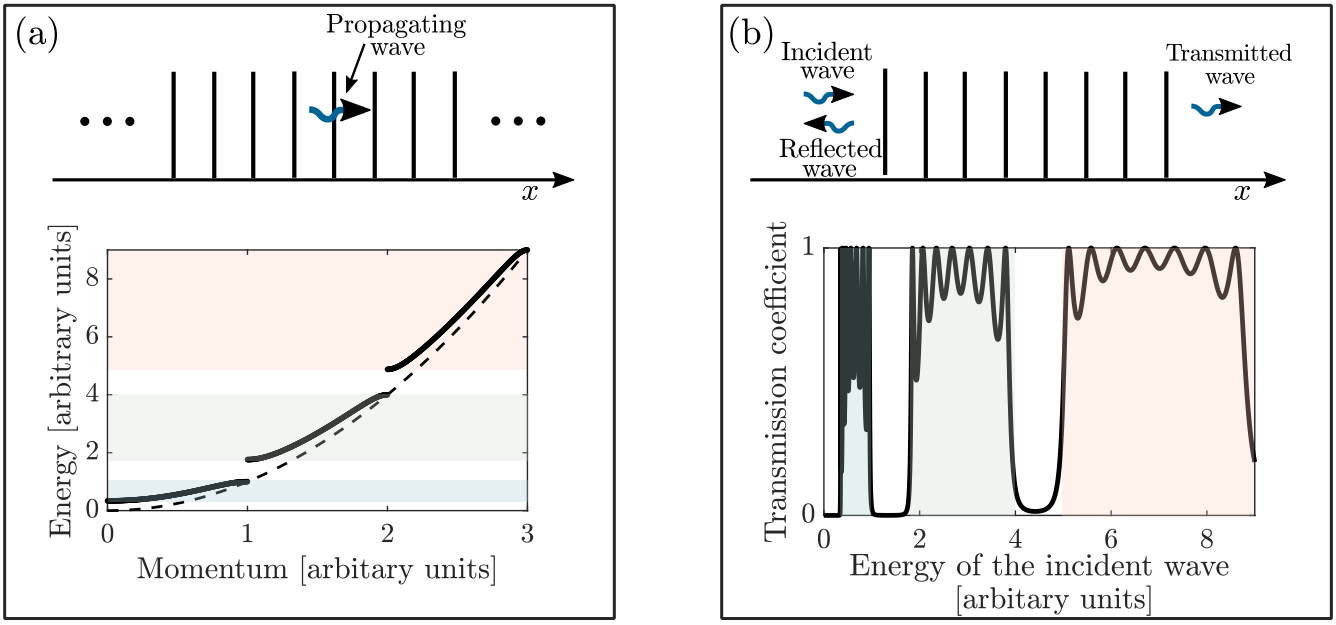

Figure 1: (a) Upper: Schematic description of the propagation of a wave in an infinite array of delta Dirac functions. Lower: The energies for which the propagation is allowed form bands. (b) Upper: Schematic description of the scattering of an incident wave by a finite array with 8 Dirac scatterers. Lower: Corresponding transmission coefficient T as a function of the energy of the incident wave. The PTRs are the peaks that correspond to $T = 1$.

found that even the global mirror symmetry is not a necessary condition for the appearance of PTRs [12] and asymmetric systems that support PTRs have also been reported [12–16]. The latter results open up many research directions for the design of asymmetric media that possess desired PTRs in their transmission spectra, for instance in ref. [17] the design of a locally symmetric medium that supports PTRs has been accomplished based on the transfer matrix method [18].

When a symmetric scattering setup that exhibits PTRs is perturbed, then its PTRs are a priori lost because its symmetry is broken. However, this subject is much less studied and it is certainly interesting to apply the perturbation theory for this investigation. To this end, in Chapter 1 we will perturb a finite periodic scattering setup that supports bands with $N-1$ PTRs and we will apply the techniques of the regular perturbation analysis. We will demonstrate a semianalytical approach that we developed, based on which we are able to design an asymmetric perturbation that preserves a desired PTR of the unperturbed setup. Surprisingly, our study led to the discovery of a connection between two apparently independent PTRs of a class of finite periodic media (those whose building block has parity symmetry). This connection implies that if one PTR among the $N-1$ of a band is preserved under some perturbations, then another PTR is automatically preserved as well.

A2. Topological properties

Another characteristic of periodic media has been revealed in recent years, by employing the concepts of topology [19]. It has been found that in various cases the band diagrams are characterized by quantities that are invariant under deformations that leave the gaps open [20]. It has also been established that these invariant quantities – which are referred as topological invariants – originate from the Berry phase [21, 22]. An inherent feature of media with non-trivial topological invariants is that they support states that are localized at their boundaries (edges) [23, 24]. These edge states typically appear within the band gaps and a key advantage of them is that they are robust against various forms of disorder [20, 25], something that points them toward various potential applications. Moreover, even though edge states and a non-trivial topology were first captured within a quantum framework – in the context of the quantum Hall effect [26] – up to this day, topological phases have been realized in a very wide range of systems, including mechanic [27–32], acoustic [33–38], photonic [39–44] and hydrodynamic [45–47] ones.

At the same time, the impact of random disorder in a medium with topological properties has also been examined. First of all, it is known that a wave cannot undergo diffusion in a disordered medium (in which the disorder is strong and random) and gets localized within it [48] (see Fig. 2). This is the well known phenomenon of the Anderson localization [49]. Along this line, it has been found that when a periodic medium with topological properties is disordered, then a topological phase transition from trivial to non-trivial may be caused [50–56]. This topological phase transition has been named topological Anderson insulator and has been experimentally verified in acoustic systems [57], in photonic ones [58] and in atomic wires [59]. In addition, this topological phase transition is accompanied by a divergence of the localization length of the edge states, which is of particular interest in the context of the Anderson localization.

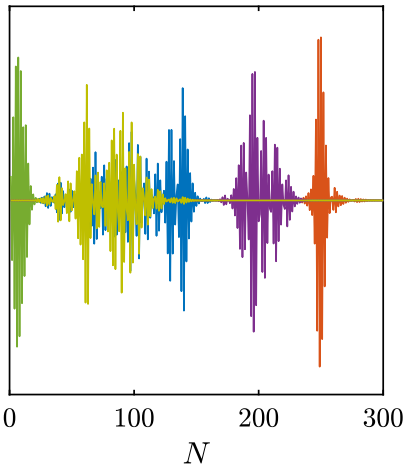

Figure 2: Shown here are five eigenstates of a disordered Hamiltonian (correspond to the five curves with different colors). The size of the disordered system is $N = 300$ sites. All these eigenstates are localized. The energies of these eigenstates are close in the energy spectrum, however their spatial extent is different.

Most of the investigations regarding the topological Anderson insulator have been conducted in quantum systems. We will show in Chapter 2 that such transitions take place even in disordered mechanical systems. In particular, we found that the localization length of the edge states that are supported in a mass-spring dimer lattice (due to a non-trivial topology), diverge in the presence of a strong disorder. Moreover, we revealed that the form of the disorder that is applied (random or correlated) has a strong impact at the manifestation of these phenomena.

B. Time-modulated media

Similar to spatially varying media, time-varying media – media whose properties vary with time – host novel phenomena and enrich our scientific knowledge. They play a crucial role for wave manipulation and for optimizing dynamic processes. In the second part of this thesis we investigate non-adiabatic state transfers and wave amplifying phenomena in such time-varying media.

B1. Non-adiabatic state transfer

The existence of edge states and their robustness against various forms of disorder, are features of platforms with topological properties that make them ideal for implementing a transferring process [20]. Generally speaking, the state transfer – the transfer of some information from one location to another (see Fig. 3) – is a subject of great importance and has been accomplished via photons [60], in linear spin chains [61, 62], in quantum dots [63] and in many other platforms. However, more recent studies have explored the state transfer under the prism of topology [64–68], in order to exploit the robustness of the edge states against imperfections of the transferring network. Most of these recent studies, build upon the concept of Thouless adiabatic pumping [69], that is the quantized charge transport in a one-dimensional periodic potential that is slowly varied in time and in a cyclic manner. Thouless adiabatic pumping has been realized in several systems with a non-trivial topology, including cold atoms [70–73], photonic [74–76], artificial spin systems [77, 78], quantum dots [79, 80], mechanical metamaterials [81–83], acoustic ones [84], etc.

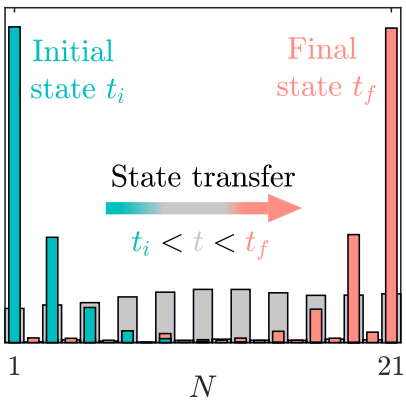

Figure 3: Schematic description of the transfer of an edge state across a lattice with $N = 21$ sites.

At the same time, there are several methods that have been developed in order to speed up adiabatic transfer processes, in order to overcome the lossy factors that these adiabatic processes are subject to, due to the slow time scales. These methods are known as "Shortcuts to Adiabaticity" [85, 86] and the general idea behind these methods is to produce the same final state – given the same initial state – as an adiabatic process does, by exploiting the non-adiabatic excitations that take place when the parameters of a system vary rapidly in time. Two such techniques that are widely used are the counteradiabatic driving (or transitionless driving) [87–90] (see ref. [91, 92] for the experimental realization of a counteradiabatic driving process) and the inversed engineering based on the Lewis-Riesenfeld invariants [93, 94]. There are other methods that also enable fast transfers and which are known as optimal control ones [95]. In these optimal control methods the objective is to find time-dependent control parameters that maximize a specific cost function, typically known as fidelity, under specific constraints. This is accomplished through the use of numerical techniques

that update the control parameters iteratively, until the cost function is maximized (with respect to some bound).

The counteradiabatic driving [96] and the optimal control methods [97] have been applied for the fast transfer of edge states in quantum topological lattices. In Chapter 3 we will show – using an optimal control method – that a fast transfer of an edge state is possible in a mechanical lattice as well. We will also demonstrate that the transfer is not only fast but also robust against disorder in the transfer network. An interesting finding of this study is that the transferred state can be amplified or disamplified, due to the absence of unitarity in the time-varying lattice that we considered (which is a non-autonomous system).

B2. Amplification in time-varying media

During the past decade, there has been noted a significant interest for the exploration of wave propagation in time-varying media [98,99]. This interest is attributed to a lot of fascinating features that such time-varying media display, as for instance band structures in their dispersion diagrams and non-trivial topological properties [100]. Moreover, wave phenomena like time-reflection and time-refraction [101, 102] that are captured in such media [103], also play a significant role in generating this great interest. And there is no doubt that one of their most fascinating effects, is their ability to amplify the energy of the waves that propagate in them [104]. The amplification in such time-varying media is usually (but not always - see ref. [105]) related with parametric instabilities [106].

Parametric instabilities can emerge in any dynamical system when a parameter of a system is modulated periodically in time with an appropriate frequency. A well known example is the Faraday instability in fluid mechanics [107, 108]: when a tank with a fluid layer is vertically oscillated then waves at the surface of the fluid emerge, which are called Faraday waves. The parametric instabilities are usually studied under the prism of Floquet analysis [109], since this theory derives the stability properties of the solutions and the unstable solutions are related with the parametric instabilities. Along the line of amplification there is a mechanism – that is well known in the field of hydrodynamics and emerges in static systems as well, not necessarily in time-varying ones [110] – that leads to transient amplification of stable solutions [111]. The stable solutions of a system can be transiently amplified when the matrix that propagates the initial conditions forward in time is non-normal, having thus non-orthogonal eigenvectors [112, 113]. The description of these transient amplifying features need particular tools and multiple methods are being used, as for instance the singular value decomposition [114]. Especially, one of the tools

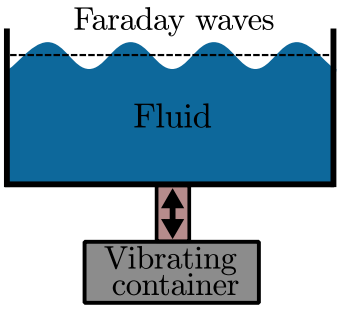

Figure 4: Schematic description of Faraday instability.

that has been developed in this direction and is widely used, is the ϵ-pseudospectrum [110].

The ϵ-pseudospectrum can been utilized in the context of wave propagation in time-varying media, since phenomena of non-normal nature are often captured in these media. We will present such a description in Chapter 4. In particular, we used the ϵ-pseudospectrum toolbar and we quantified the transient amplification that a wave that propagates in an infinite harmonically modulated medium could undergo. We considered the modulation of the medium to be carried out in a way such that the Mathieu equation [115] governs the wave dynamics [116, 117].

C. Plan of the Thesis

In this thesis we try to get an understanding of the above wave phenomena by studying four different problems. Specifically: In Chapter 1 we investigate the robustness to asymmetric perturbation of the PTRs that are supported in a finite periodic scattering system that is build from a mirror symmetric cell. As a first step, we calculate the correction at the wave numbers of the incident waves that correspond to these PTRs (in first order perturbation theory). Subsequently, we consider a perturbation that consists of Dirac scatterers and we show how PTRs could still appear in the perturbed case with a suitable design of the perturbation. Finally, we reveal a connection between two apparently independent PTRs of the unperturbed setup, which lies in the mirror symmetry of the cells.

In Chapter 2 we study the localization properties of a disordered 1D dimer mass-spring chain. In the absence of disorder, the dimer chain that we consider consists of same masses and springs with alternating stiffness values. Such a dimer chain possesses a so called chiral symmetry and non-trivial topological features. As a result, edge states are supported in a corresponding finite dimer chain. We apply two forms of disorder in a finite dimer chain: the first form retains its chiral symmetry while the second one breaks it and we compute the localization length of the edge states using the transfer matrix method.

The model that we use in Chapter 3 is again a dimer mass-spring chain. However, in this Chapter we use this setup under a different prism, since our goal here is to transfer an edge state through the chain. To achieve such a transfer we let the spring couplings to vary with time, making thus the chain time-dependent (the chain that we use in Chapter 2 is static). We are also interested to achieve the transfer fast and to that end we use an optimal control method. We design several protocols for the time-varying couplings and we show how to reduce the transfer time. Furthermore, we explore the impact of disorder to these transfer protocols in order to deduce whether the gain in transfer speed comes with a cost in robustness.

In Chapter 4 we consider the propagation of a wave in an infinite medium that is periodically modulated in time, in a way so that the Mathieu equation emerges [116, 117]. The Mathieu equation contains both stable and unstable regions in the parameter space [115] and we explore the amplification features of its stable solutions. We search for the maximum possible transient

amplification by optimizing the initial conditions as well as the initial start of the process. We also make use of several quantities of the ϵ-pseudospectrum of the monodromy matrix – the matrix that propagates the initial conditions over one period – and we provide numerical evidence that the knowledge of the monodromy matrix is sufficient to derive the overall maximum amplification.

Finally in Chapter 5 we conclude our findings and we discuss our future perspectives. This thesis is accompanied by four appendices. Each one of these appendices corresponds to each one of the four chapters. Particularly: In Appendix A we provide the analytic proofs of some relations that are given in Chapter 1. In Appendix B we give some details regarding the transfer matrix method that we use in Chapter 2. In Appendix C, we prove – using the WKB method [118] – that if the couplings of the dimer chain that we consider in Chapter 3 vary slowly in time, then the transfer process is done successfully. Finally, in Appendix D we provide closed form expressions that help us to get a deeper understanding of some results that are presented in Chapter 4.

Chapter 1

Perfect transmission resonances of perturbed scattering systems

1.1 Introduction

A one-dimensional periodic scattering setup is known to possess a transmission spectrum that has a band-like structure form [5]. Within each of the bands, the transmission becomes exactly one at least $N-1$ times, where N is the number of cells of the setup. The case of transmission 1 is known as a perfect transmission resonance (PTR). When such a periodic scattering setup is perturbed, then the PTRs that it supports are a priori lost.

In this Chapter, we investigate the PTRs of a perturbed 1D finite periodic system with mirror symmetric cells. For this investigation we use the transfer matrix method and the classical perturbation analysis.

1.2 Scattering by a periodic system with mirror symmetric cells

We begin by considering the scattering in one dimension by a mirror symmetric potential barrier $V(x)$. The potential $V(x)$ is real and zero outside the region $[-d/2, d/2]$. For a schematic illustration of such a potential and of the scattering process see Fig. 1.1(a). The waves involved satisfy the stationary Schrödinger equation

$$\psi'' + \left[k^2 - V(x)\right]\psi = 0, \tag{1.1}$$

where ψ is the wave function, prime denotes differentiation with respect to x and k is the wave number of the waves in the regions outside of the scattering area (which is free). At the left side of the barrier the wave function is given by $\psi_L = \psi_L^+ + \psi_L^-$ where $\psi_L^+ = Ae^{ikx}$ and $\psi_L^- = Be^{-ikx}$

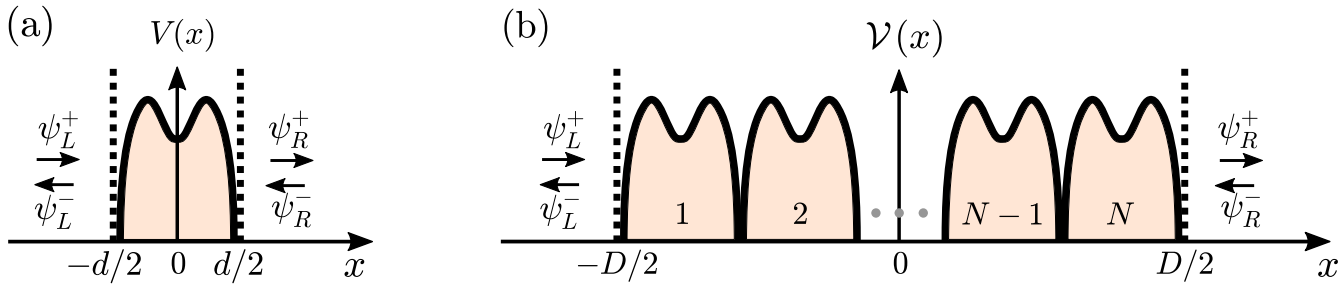

Figure 1.1: (a) Schematic description of scattering by a mirror symmetric potential $V(x)$. (b) Corresponding schematic description of scattering by a finite periodic potential $\mathcal{V}(x)$ that is build by the repetition N times in space of the barrier that is shown in (a).

and similarly at the right side of the barrier the wave function is $\psi_R = \psi_R^+ + \psi_R^-$ where $\psi_R^+ = Ce^{ikx}$ and $\psi_R^- = De^{-ikx}$.

By invoking the boundary conditions at the two edges of the setup, namely at the points $x = \pm d/2$, we find two linear relations for the wave function

$$\begin{pmatrix} \psi_R^+ \\ \psi_R^- \end{pmatrix}\Bigg|_{x=d/2} = \mathbf{M} \begin{pmatrix} \psi_L^+ \\ \psi_L^- \end{pmatrix}\Bigg|_{x=-d/2} . \tag{1.2}$$

The matrix $\mathbf{M}$ is called transfer matrix and is given by

$$\mathbf{M} = \begin{pmatrix} 1/t^* & r/t \\ (r/t)^* & 1/t \end{pmatrix}, \tag{1.3}$$

where t and r are the transmission and reflections coefficients accordingly.[1] The probability that the wave is transmitted (reflected), is the transmission (reflection) coefficient and is given by $T = |t|^2$ ($R = |r|^2$).

If we repeat the barrier $V(x)$ that is illustrated in Fig. 1.1(a) N times in space, then we build the potential $\mathcal{V}(x)$ that is shown in Fig. 1.1(b). Similarly to the single barrier case, the transfer matrix of this finite periodic setup relates the fields $\psi_{L,R}^{\pm}$ at the two edges of the scattering region (these edges are the $-D/2$ and $D/2$ this time, with $D = Nd$). Furthermore, the transfer matrix of this finite periodic setup is given by the N times multiplication of the transfer matrix that is given in Eq. (1.3), it is namely the $\mathbf{M}^N$. With the use of the Chebychev identity [2], we get that

[1] To find the physical meaning of the coefficients r and t we consider the scattering only from the one side of the barrier. For instance, if we consider the scattering from the left side of the barrier (we set $\psi_R^- = 0$ and the incoming wave is the ψ_L^+), then we get that $\psi_R^+(x = d/2) = t\psi_L^+(x = -d/2)$ and $\psi_L^-(x = -d/2) = r\psi_L^+(x = -d/2)$. For that reason, the quantities t and r are called the transmission and reflections coefficients accordingly. We note here, that the transfer matrix $\mathbf{M}$ contains in general two reflection amplitudes r and $\tilde{r}$ when the scattering by the two sides of the barrier are considered. However, when the barrier is mirror symmetric, as in our problem, then the two reflection amplitudes are the same. For a detailed discussion see ref. [119].

$\mathbf{M}^N$ is given by

$$\mathbf{M}^N = \begin{pmatrix} 1/t_N^* & r_N/t_N \\ -r_N/t_N & 1/t_N \end{pmatrix} = \begin{pmatrix} \frac{1}{t^*}\frac{\sin(N\phi)}{\sin(\phi)} - \frac{\sin((N-1)\phi)}{\sin(\phi)} & \frac{r}{t}\frac{\sin(N\phi)}{\sin(\phi)} \\ -\frac{r}{t}\frac{\sin(N\phi)}{\sin(\phi)} & \frac{1}{t}\frac{\sin(N\phi)}{\sin(\phi)} - \frac{\sin((N-1)\phi)}{\sin(\phi)} \end{pmatrix} \tag{1.4}$$

where $\phi = \frac{1}{2}\mathrm{Tr}(\mathbf{M}) = \mathrm{Re}\left[\frac{1}{t}\right]$ is the Bloch phase of the infinite periodic system and is related with the wave number k.

1.2.1 Perfect transmission resonances

A nice expression for the transmission coefficient $T_N = |t_N|^2$ of the finite periodic system is given by (see for instance ref. [6])

$$T_N = \frac{1}{1 + \left(\frac{1}{T} - 1\right)\frac{\sin^2(N\phi)}{\sin^2(\phi)}}. \tag{1.5}$$

Notice that for $\phi_n = n\pi/N +$ mod (2π) with $n = 1, 2, ..., N-1$ then $T_N = 1$. Besides, whenever $T = 1$ then $T_N = 1$ as well.

As an illustration we consider the scattering from the left side of the setup that is shown in Fig. 1.2(a). Notice that this setup consists of 8 rectangular barriers (further details are given in the caption). In Fig. 1.2(b) we present the corresponding transmission spectrum $T_N(k)$. Clearly, the transmission spectrum shows a band-like structure form, while each band consists of at least $N-1$ PTRs (the transmission coefficient T_N is equal to 1). We stress here that this band structure form is related only with the periodicity of the system and not with its mirror symmetry (the mirror

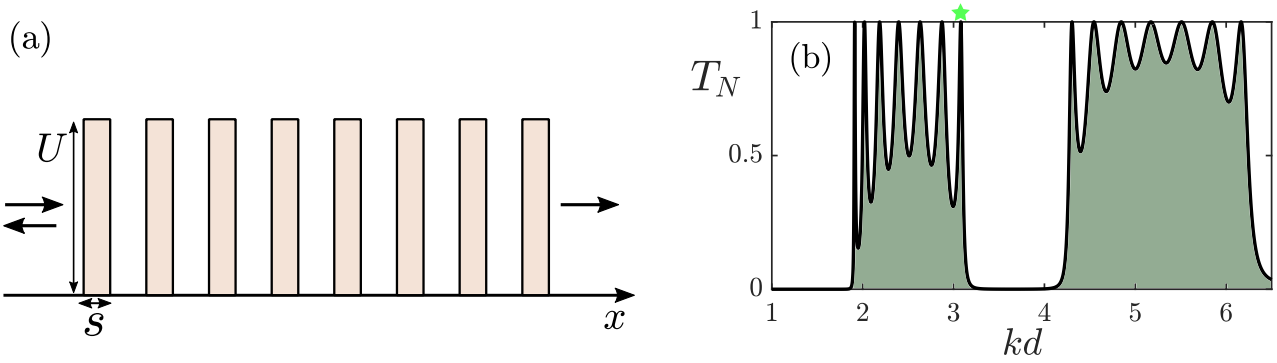

Figure 1.2: (a) Scattering from the left side of a setup that consists of 8 rectangular barriers. The length of each barrier is $s = d/6$ and therefore the free space between two neighboring barriers has length $5d/6$ (notice that this figure does not represent such distances). We set the heights $U = \max_x V(x)$ of the barriers at $d^2U = 27$. (b) Transmission coefficient T_N as a function of kd when scattering by the setup that is shown in (a) is considered.

symmetry imposes some extra conditions that we will see in the following). All one-dimensional finite periodic scattering setups have transmission spectrum with a similar structure, that is due to Eq. (1.5).

1.2.2 Implications of mirror symmetry

As will appear in the following, the symmetry of the wave function has an implication at the formulas that we obtain when the potential $\mathcal{V}(x)$ is perturbed. From now on we denote with $\psi_n(x)$ the wave function that corresponds to the PTR number n. Due to the mirror symmetry of the scattering setup, the real part $\mathrm{Re}[\psi_n(x)]$ can become symmetric and the imaginary part $\mathrm{Im}[\psi_n(x)]$ can become antisymmetric with respect to the axis where the potential $\mathcal{V}(x)$ is also symmetric. Throughout this work, we set this axis to be at $x = 0$. More specifically, if we set the amplitude A of the incoming wave (we consider scattering from the left side of the setup and therefore the incoming wave is given by $\psi_L^+ = Ae^{ikx}$) equal to

$$A = \begin{cases} e^{ik_n D/2}, & \text{for even } n \\ e^{ik_n D/2 - i\pi/2}, & \text{for odd } n \end{cases} \tag{1.6}$$

where k_n is the wave number that corresponds to the PTR number n, then the real part of ψ_n is symmetric and the imaginary part is antisymmetric around $x = 0$. In Fig. 1.3(a) we show the real and imaginary parts of the wave function that correspond to the last PTR ($n = 7$) of the first band that is shown in Fig. 1.2(b) (this PTR is indicated with the green star), when we set $A = e^{ik_7 H/2 - i\pi/2}$. Clearly the real part is symmetric and the imaginary part is antisymmetric. In Fig. 1.3(b) we show the corresponding real and imaginary parts of the wave function for a choice of A that is not equal to $e^{ik_7 H/2 - i\pi/2}$. In this case the real and imaginary parts of the wave function are not symmetric.

We close this section by noting that the wave function $\psi_n(x)$ is found from the solution of the Schrödinger equation Eq. (1.1) with boundary conditions

$$\begin{aligned} \left.\frac{d\psi_n(x)}{dx}\right|_{x=-D/2} - ik_n\psi_n(-D/2) = 0 \\ \left.\frac{d\psi_n(x)}{dx}\right|_{x=D/2} - ik_n\psi_n(D/2) = 0 \end{aligned} . \tag{1.7}$$

Notice that for the case of a mirror symmetric potential $\mathcal{V}(x)$, Eq. (1.1) and the boundary conditions in Eq. (1.7) form an eigenvalue problem that is $\mathcal{PT}$-symmetric [120,121], where $\mathcal{P} : x \to -x$ is the parity operator and $\mathcal{T} : z \to z^*$ is the time reversal operator.

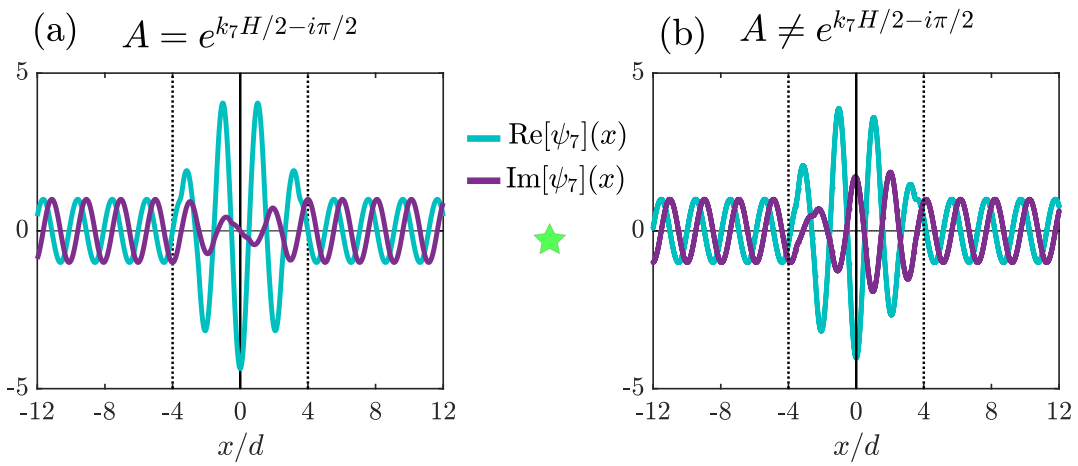

Figure 1.3: (a) Real and imaginary parts of the wave function $\psi_7(x)$ that corresponds to the PTR number $n = 7$ that is shown in Fig. 1.2(b) and is indicated with a green star. The amplitude of the incoming wave is $A = e^{ik_7 H/2 - i\pi/2}$ where k_7 is the wave number of the 7^{th} PTR in the first band. (b) Same as (a) but for $A \neq e^{ik_7 H/2 - i\pi/2}$.

1.3 Perturbing the potential

Consider now that a finite periodic and mirror symmetric potential $\mathcal{V}_0(x)$ – as the one that is illustrated in Fig. 1.1(b) – is perturbed. After the perturbation, the scattering region is described by the potential

$$\mathcal{V}(x) = \mathcal{V}_0(x) + \epsilon \mathcal{V}_1(x) \tag{1.8}$$

with $\epsilon << 1$. We assume that the perturbing potential $\mathcal{V}_1(x)$ is non-zero only inside the region $[-D/2, D/2]$, that is inside the unperturbed scattering region. The goal of this part is to examine the influence of the perturbation at the wave numbers of the unperturbed system that correspond to the PTRs, namely at the wave numbers $k_{0,n}$. Hereafter, the index 0 denotes the unperturbed system and the index n denotes a PTR, $n = 1, 2, ..., N-1$.

1.3.1 Perturbation expansion

The wave number and the wave function that correspond to the PTR number n change as

$$k_n = k_{0,n} + \epsilon k_{1,n} + \dots \tag{1.9}$$

$$\psi_n(x) = \psi_{0,n}(x) + \epsilon \psi_{1,n}(x) + \dots \tag{1.10}$$

We plug these forms, along with the potential $\mathcal{V}(x)$ that is given in Eq. (1.8), into the Schrödinger equation Eq. (1.1) and at the corresponding boundary conditions that are given in Eq. (1.7) and we collect in powers of ϵ. Clearly, the $\psi_{0,n}(x)$ and $k_{0,n}$ satisfy the zero order problem, which we

write again for convenience:

$$\frac{d^2\psi_{0,n}(x)}{dx^2} + \left(k_{0,n}^2 - \mathcal{V}_0(x)\right)\psi_{0,n}(x) = 0 \tag{1.11}$$

and

$$\begin{aligned} \left.\frac{d\psi_{0,n}(x)}{dx}\right|_{x=-D/2} - ik_{0,n}\psi_{0,n}(-D/2) = 0 \\ \left.\frac{d\psi_{0,n}(x)}{dx}\right|_{x=D/2} - ik_{0,n}\psi_{0,n}(D/2) = 0 \end{aligned} . \tag{1.12}$$

After a few manipulations, we find that the first order term $\psi_{1,n}(x)$ is given by the solution of the equation

$$\frac{d^2\psi_{1,n}(x)}{dx^2} + \left(k_{0,n}^2 - \mathcal{V}_0\right)\psi_{1,n} = -\left(2k_{0,n}k_{1,n} - \mathcal{V}_1\right)\psi_{0,n} \tag{1.13}$$

while it satisfies the boundary conditions

$$\begin{aligned} \left.\frac{d\psi_{1,n}(x)}{dx}\right|_{x=-D/2} - ik_{0,n}\psi_{1,n}(-D/2) = ik_{1,n}\psi_{0,n}(-D/2) \\ \left.\frac{d\psi_{1,n}(x)}{dx}\right|_{x=D/2} - ik_{0,n}\psi_{1,n}(D/2) = ik_{1,n}\psi_{0,n}(D/2). \end{aligned} \tag{1.14}$$

The latter boundary conditions are not guaranteed to give a PTR: for the PTR number n to be preserved perturbatively (only in first order and not in higher order), the imaginary part of the wave number $k_{1,n}$ has to be zero.

For the calculation of $k_{1,n}$, we apply the classical solvability condition, namely we multiply Eq. (1.13) with $\psi_{0,n}(x)$ and we integrate in the scattering region, which leads to the equation

$$\int_{-D/2}^{D/2}\psi_{0,n}(x)\frac{d^2\psi_{1,n}(x)}{dx^2}dx = \left[\psi_{0,n}(x)\frac{d\psi_{1,n}(x)}{dx} - \frac{d\psi_{0,n}(x)}{dx}\psi_{1,n}(x)\right]_{-D/2}^{D/2} + \int_{-D/2}^{D/2}\frac{d^2\psi_{0,n}(x)}{dx^2}\psi_{1,n}(x)dx \tag{1.15}$$

By inserting Eq. (1.11)-(1.14) in Eq. (1.15) we find the expression for the wave number $k_{1,n}$,

$$k_{1,n} = \frac{\displaystyle\int_{-D/2}^{D/2}\mathcal{V}_1\psi_{0,n}^2 dx}{i[\psi_{0,n}^2(D/2) - \psi_{0,n}^2(-D/2)] + 2k_{0,n}\displaystyle\int_{-D/2}^{D/2}\psi_{0,n}^2 dx}, \tag{1.16}$$

where $\psi_{0,n}$ is the wave function of the unperturbed system (thus the index 0).

For the derivation of Eq. (1.16) the potential $\mathcal{V}_0$ does not need to be periodic or mirror symmetric. Yet, if $\mathcal{V}_0$ is mirror symmetric then the real/imaginary parts of the wave function $\psi_{0,n}$ become symmetric if we multiply $\psi_{0,n}$ with a suitable phase (see Section 1.2.2). Using symmetric real/imaginary parts of $\psi_{0,n}$ we can show that the denominator in Eq. (1.16) is real and therefore

the imaginary part of $k_{1,n}$ is given by

$$\mathrm{Im}[k_{1,n}] = \mathcal{C} \int_{-D/2}^{D/2} \mathcal{V}_1 \mathrm{Re}[\psi_{0,n}] \mathrm{Im}[\psi_{0,n}] dx \tag{1.17}$$

with $\mathcal{C}$ real. As we noted before, we are interested in $\mathrm{Im}[k_{1,n}]$ because if it is zero then the PTR number n of the unperturbed setup remains as a PTR after the perturbation (in first order). The real part of $k_{1,n}$ shows whether a PTR is shifted right or left in the transmission spectrum when $\mathrm{Im}[k_{1,n}] = 0$.

1.3.2 Preserving all PTRs

Notice that if $\mathcal{V}_1$ is mirror symmetric (even function with respect to $x = 0$) then $\mathrm{Im}[k_{1,n}] = 0$ for all n, because the quantity $\mathrm{Re}[\psi_{0,n}]\mathrm{Im}[\psi_{0,n}]$ is odd for all n. Therefore, all the PTRs of the unperturbed system are preserved (in first order) after the addition of such a mirror symmetric perturbation.

For an illustration, we consider the scattering from the left side of the setup that is shown in Fig. 1.4(a). In Fig. 1.4(b) we present the corresponding transmission spectrum. Notice that bands with $N - 1 = 7$ PTRs appear again as it was the case in Fig. 1.2(b). However, these PTRs do not appear at the same wave numbers as the ones that are shown in Fig. 1.2(b), since the real part of $k_{1,n}$ is in general not zero.

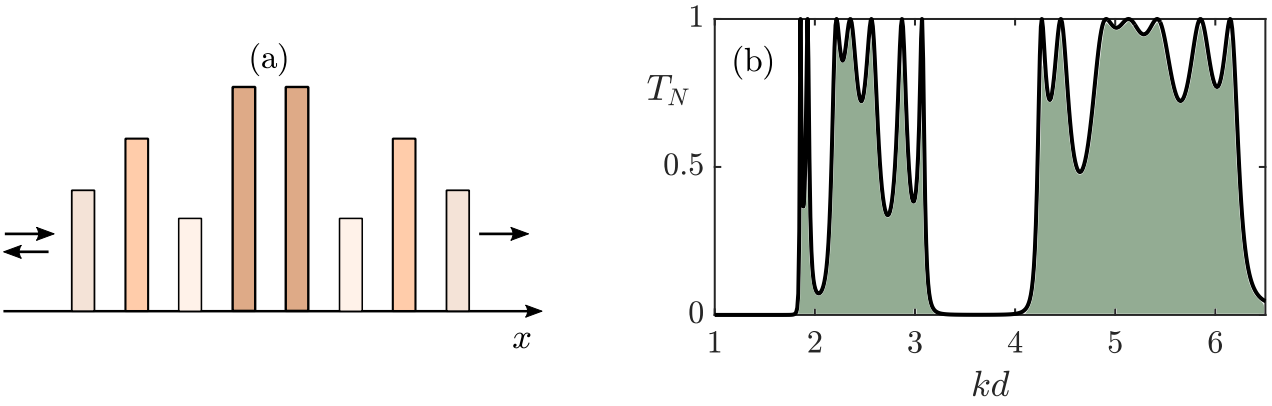

Figure 1.4: We set the parameter ϵ of the perturbation at $\epsilon = 0.1$. (a) The unperturbed setup is the same as in Fig. 1.2(b) and we consider that only the strengths of the barriers are perturbed (all the distances are the same as in Fig. 1.2(b)). The perturbations at the first and last barriers satisfy $d^2U_1 = d^2U_8 = -27$. We set the perturbations at the rest barriers at: $d^2U_2 = d^2U_7 = 0$, $d^2U_3 = d^2U_6 = -72$ and $d^2U_4 = d^2U_5 = 27$. (b) Transmission spectrum of the setup that is shown in (a).

1.3.3 Preserving one PTR

In this part we show how to design perturbing potentials $\mathcal{V}_1(x)$ that preserve specific PTRs (not all of them as an even $\mathcal{V}_1$ does). To that end we use Eq. (1.17) and we design $\mathcal{V}_1$ so that $\mathrm{Im}[k_{1,n}] = 0$ for a specific PTR (number n). However, it is not a trivial task to design such a $\mathcal{V}_1$. We can simplify the analysis though and make this design easy if we choose $\mathcal{V}_1$ to be a sum of Dirac scatterers,

$$\mathcal{V}_1 = \sum_{m=1}^{M} c_m \delta(x - w_m) \tag{1.18}$$

where M is the number of Dirac scatterers that we place inside the unperturbed scattering region, c_m are their strengths and $w_m \in [-D/2, D/2]$ are their positions.

In order to see clearly why the design is now easy, notice first that Eq. (1.17) with $\mathcal{V}_1$ a sum of Dirac functions gets the form

$$\mathrm{Im}[k_{1,n}] = \mathcal{C} \sum_{m=1}^{M} c_m \mathrm{Re}[\psi_{0,n}(w_m)] \mathrm{Im}[\psi_{0,n}(w_m)]. \tag{1.19}$$

The wave function $\psi_{0,n}(x)$ is known. So, we can search for the strengths of the Dirac scatterers that result in $\mathrm{Im}[k_{1,n}] = 0$ for a specific n.

As an illustration, suppose that we add two delta scatterers at a finite periodic potential, as the one that is shown in Fig. 1.1(b). We place the first scatterer in the region of the barrier number i and the second scatterer in the region of the barrier number j. Then for the n^{th} PTR to be preserved after the addition of the two scatterers the following condition must hold (we drop the index n)

$$c_i \times \mathrm{Re}[\psi_0(w_i)] \mathrm{Im}[\psi_0(w_i)] + c_j \times \mathrm{Re}[\psi_0(w_j)] \mathrm{Im}[\psi_0(w_j)] = 0, \tag{1.20}$$

Now, we can set the strength of one of the two scatterers at some value and we can find the strength of the other scatterer so that Eq. (1.20) holds.

In Fig. 1.5 we present an example. Figure 1.5(a) shows the scattering setup that we consider and Fig. 1.5(b) shows the corresponding transmission spectrum of this setup. Notice that the scatetring setup consists of 8 rectangular barriers and 2 Dirac scatterers. We place the first Dirac scatteter in the region of the first rectangular barrier and the second Dirac scatteter in the region of the second rectangular barrier. We note here that we do not place the Dirac scatterers in the centers of the barriers (for the details see the caption). We set the strength of the first delta function, c_1, to some arbitrary value and calculate c_2 from Eq. (1.20) so that the PTR number $n = 7$ is preserved after the perturbation. Evidently, with a look at the transmission spectrum that is shown in Fig. 1.5(b) (notice that we only show the first band) we get that the PTR number $n = 7$ is indeed preserved, while the rest of the PTRs are not.

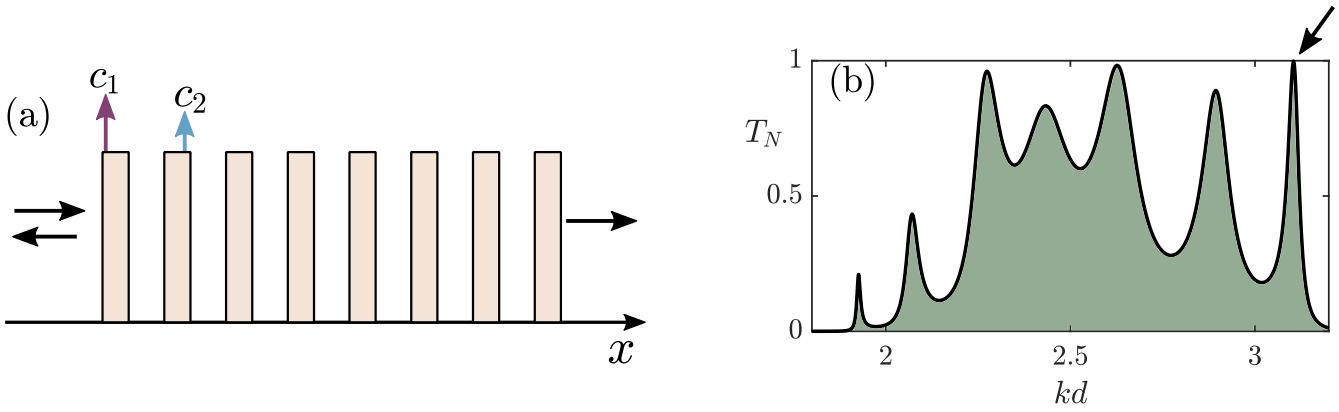

Figure 1.5: We set the parameter ϵ of the perturbation at $\epsilon = 0.1$. (a) Schematic description of scattering by a setup that consists of rectangular barriers and 2 delta scatterers. The height of the barriers, the lengths and the free space between two neighboring barriers are the same as in Fig. 1.2(b). The distance between the first Dirac scatterer and the left edge of the first barrier is $0.1s$ (recall that s is the length of each barrier). The strength of the first Dirac scatterer is set at $dc_1 = 4.8$. The distance between the second Dirac scatterer and the right edge of the second barrier is $0.05s$. The strength of the second Dirac scatterer is found from Eq. (1.20) in order for the PTR number $n = 7$ to be preserved after the addition of the two delta scatterers. (b) Transmission spectrum of the setup that is shown in (a). Notice that only the PTR number $n = 7$ is preserved (it is indicated with the arrow).

1.4 Particular classes of perturbations that preserve two PTRs

In this part we design again perturbations with Dirac scatterers that preserve desired PTRs. The difference now is that we place the Dirac scatterers either in the centers or at the edges of the cells of the unperturbed system.

1.4.1 Perturbation at the centers of the cells

We start this part with the presentation of an example. The scattering setup that we consider is illustrated in Fig. 1.6. Notice that it consists of 8 rectangular barriers and 2 Dirac scatterers. The first Dirac scatterer is placed at the center of the first barrier and the second Dirac scatterer at the center of the third barrier. In Fig. 1.6(b)-(d) we show the transmission of this setup, for three different choices of the strength c_3. In Fig. 1.6(b) we choose the strength c_3 so that the first PTR ($n = 1$) is preserved. The result is that apart from the first PTR, the PTR that corresponds to the index $n = 7$ is also preserved. In Fig. 1.6(c) we choose the strength c_3 so that the second PTR is preserved after the perturbation. Notice that the symmetric PTR ($n = 6$) is preserved as well. Similarly, in Fig. 1.6(d) we choose the strength c_3 so that the third PTR is preserved after the perturbation. Notice that PTR number $n = 5$ is also preserved. These results suggest that there

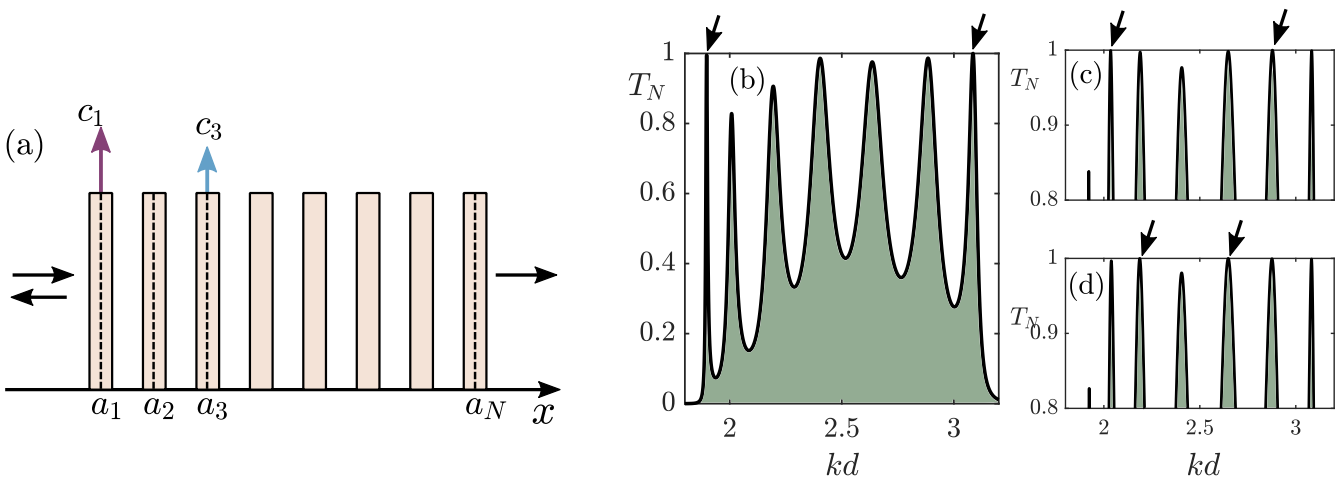

Figure 1.6: We set the parameter ϵ of the perturbation at $\epsilon = 0.1$. (a) Schematic description of scattering by a setup that consists of rectangular barriers and 2 delta scatterers that are placed at the center of the first and third barrier respectively. Again, the heights of the barriers, the lengths and the free space between two neighboring barriers are the same as in Fig. 1.2(b). (b)-(d) Transmission of the setup that is shown in (a) for three different choices of c_3. The arrows above the transmission spectra show which PTRs are preserved after the perturbation. In (b) we set the strength of the first scatterer equal to $dc_1 = 12$. The strength c_3 is given by Eq. (1.20) so that the PTR number number $n = 1$ is preserved. Notice that the PTR number $n = 7$ is preserved as well. In (c) we set $dc_1 = 4.5$ and we calculate the strength c_3 so that PTR number number $n = 2$ is preserved. Indeed this PTR is preserved. The symmetric PTR, $n = 6$, is preserved as well. In (d) $dc_1 = 2.4$ and c_3 is designed to preserve the PTR number $n = 3$. Notice that the symmetric PTR $n = 5$ is also preserved.

is a connection between the PTRs number n and $N - n$ in each band.

This connection lies in a symmetry between the quantities $K(n, m) = \mathrm{Re}[\psi_{0,n}(a_m)]\mathrm{Im}[\psi_{0,n}(a_m)]$ and $K(N - n, m) = \mathrm{Re}[\psi_{0,N-n}(a_m)]\mathrm{Im}[\psi_{0,N-n}(a_m)]$ where a_m are the centers of the cells and $m = 1, 2, ..., N$. In Appendix A we prove that for any periodic system with mirror symmetric cells the following relation holds (to the best of our knowledge the analytic results given in this and in the next subsections are not known in the bibliography and are stated here for the first time)

$$\mathrm{Re}[\psi_{0,n}(a_m)]\mathrm{Im}[\psi_{0,n}(a_m)] = f(\phi_n)g(m, \phi_n) \tag{1.21}$$

where

$$g(m, \phi_n) = \sin^2[(N - m)\phi_n] - \sin^2[(m - 1)\phi_n] \tag{1.22}$$

and

$$\phi_n = \frac{n\pi}{N} \tag{1.23}$$

is the Bloch phase of the n^{th} PTR. Notice that if we interchange n with $N - n$ then for the Bloch

phases ϕ_{N-n} and ϕ_n we get that

$$\phi_{N-n} = \pi - \phi_n \tag{1.24}$$

and it is easy to see that the functions $g(m, \phi_n)$ and $g(m, \phi_{N-n})$ are the same. Importantly, $f(\phi_n)$ does not depend on the index m. The fact that $g(m, \phi_n)$ and $g(m, \phi_{N-n})$ are the same and that $f(\phi_n)$ does not depend on the index m concludes our proof since the sum in Eq. (1.19) is on the index m.

We note here that the relations that are given in Eq. (1.21)-(1.23) hold for any one-dimensional periodic system with mirror symmetric cells. Therefore, we have proven that if we place Dirac scatterers at the centers of a periodic setup with mirror symmetric barriers and the PTR number n is preserved, then the PTR number $N - n$ will also be preserved.

1.4.2 Perturbation at the edges of the cells

Now, we consider the case where the Dirac scatterers are placed at the edges of the cells. We denote the locations of the edges of the cells as b_m, $m = 0, 1, 2, ..., N$. Similarly to the previous part, we analyze the quantity $\mathrm{Re}[\psi_{0,n}(b_m)]\mathrm{Im}[\psi_{0,n}(b_m)]$we show that it is written in the form (see Appendix A),

$$\mathrm{Re}[\psi_{0,n}(b_m)]\mathrm{Im}[\psi_{0,n}(b_m)] = \tilde{f}(\phi_n)\tilde{g}(m, \phi_n) \tag{1.25}$$

where $\phi_n = n\pi/N$ is again the Bloch phase of the n^{th} PTR. Notice that the function $\tilde{f}(\phi_n)$ does not depend on the index m – position of a Dirac scatterer. The function $\tilde{g}(m, \phi_n)$ is given by

$$\tilde{g}(m, \phi_n) = \sin(2m\phi_n). \tag{1.26}$$

In this case we find two symmetries. First, the function $\tilde{g}(m, \phi_n)$ is invariant under the interchange $n \to N - n$, showing that if the PTR number n is preserved after the perturbation, the PTR number $N - n$ is also preserved. The second symmetry is due to the 2 factor in the sine function in Eq. (1.26). In the interchange $n \to (N/2) - n$ we find that the function $\tilde{g}(m, \phi_{(N/2)-n})$ becomes equal to $(-1)^m\tilde{g}(m, \phi_n)$. Therefore, for N even, if the number m is only odd or even (meaning that we place Dirac scatterers only at the edges of the odd/even cells) and if the PTR number n is preserved, so does the PTR number $(N/2) - n$.

As an illustration, we consider scattering by the setup that is shown in Fig. 1.7(a). Once more, we use as the unperturbed system the one that consists of 8 rectangular barriers. We place one Dirac scatterer at the right edge of the first cell and another Dirac scatterer at the right edge of the third cell. We set the strength of the first scatterer at some value and calculate the strength of the second one from Eq. (1.20) so that the PTR number $n = 1$ is preserved in Fig. 1.7(b) and the PTR number $n = 2$ is preserved in Fig. 1.7(c). Notice that in Fig. 1.7(b) the PTR number $n = 7$ is also preserved due to the symmetry in the interchange $n \to N - n$. What is more, the PTRs number $n = 3$ and $n = 5$ are also preserved, due to the symmetry $n \to (N/2) - n$. In Fig. 1.7(c)

because both the symmetries $n \to N-n$ and $n \to (N/2)-n$ render back the PTR number $n = 6$, only this PTR is found in the transmission spectrum, apart from the PTR number $n = 2$.

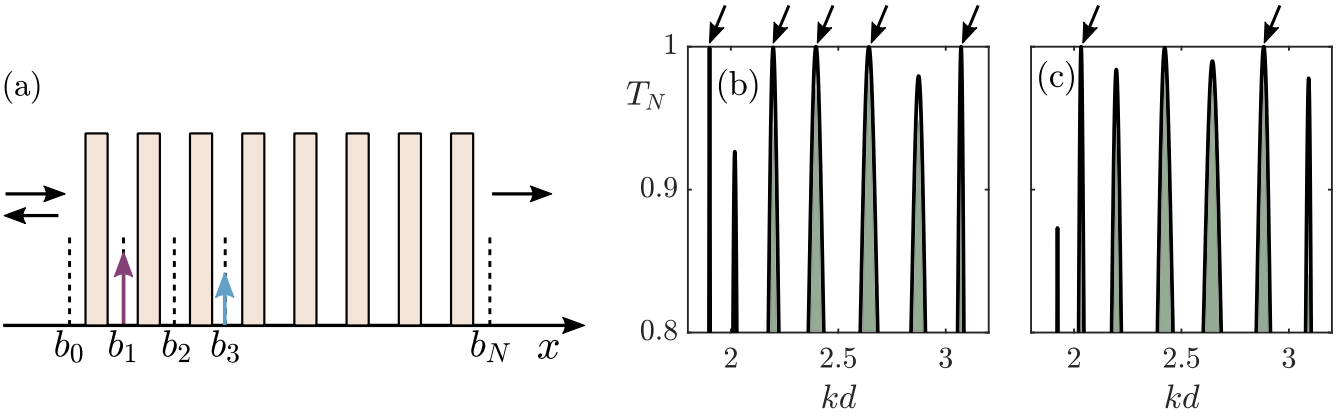

Figure 1.7: We set the parameter ϵ of the perturbation at $\epsilon = 0.1$. (a) Schematic description of scattering by a setup that consists of rectangular barriers and 2 delta scatterers that are placed at the edges of the first and third barrier respectively. The heights, the lengths of the barriers and the free space between two neighboring barriers are as in Fig. 1.2(b). (b) We set the strength c_1 of the first delta scatterer equal to $dc_1 = 1.5$ and we calculate c_3 from Eq. (1.20) so that the PTR number $n = 1$ is preserved. We find that the PTR number $n = 7$ is preserved as well, due to the symmetry in the interchange $n \to N-n$. We also find that the PTRs number $n = 2$ and $n = 6$ are also preserved. This result is due to the symmetry in the interchange $n \to (N/2) - n$. (c) We set $dc_1 = 1.5$ and we calculate c_3 again from Eq. (1.20) so that the PTR number $n = 2$ is preserved. Due to the symmetry $n \to N - n$ we find that the PTR number $n = 6$ is preserved as well. The symmetry $n \to (N/2) - n$ preserves the same PTR, i.e., $n = 6$.

1.5 Concluding remarks

In this Chapter we have studied the scattering by a perturbed periodic setup with mirror symmetric cells. We have shown how to build a perturbation that is comprised by Dirac scatterers and that maintains PTRs of the unperturbed setup, by tuning appropriately the strengths of the Dirac scatterers. We have also shown that if the Dirac scatterers are placed either at the centers or at the edges of the cells then the PTRs are preserved in pairs. As a last remark we show in Fig. 1.8 the influence of the parameter ϵ of the perturbation at the PTRs for three different cases.

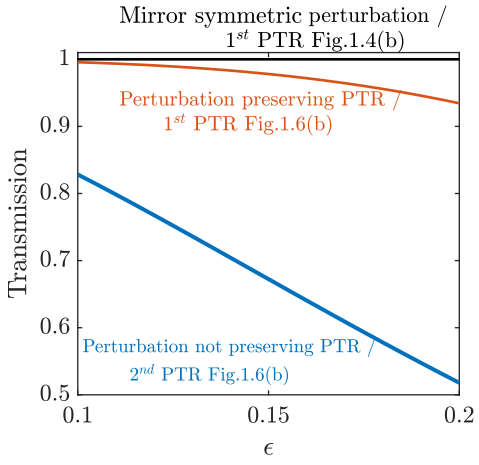

Figure 1.8: Influence of the parameter ϵ of the perturbation at PTRs.

Chapter 2

Localization properties of a disordered dimer chain

2.1 Introduction

Probably the most simple model that captures essential topological features, such as the emergence of edge states, is the celebrated Su-Schrieffer-Heeger (SSH) model [122]. The SSH model was developed in a quantum mechanical framework: it describes the hopping of particles in a one dimensional lattice with two alternating coupling strengths. During the last years, the impact of disorder in a SSH lattice has been investigated and it has been found that a static disorder causes a topological phase transition [54, 55].

The mechanical analogue of the SSH lattice is a chain with identical masses that are connected by alternating springs: a dimer mechanical chain [123]. Such a mechanical chain exhibits also topological features, since it has the same internal symmetry with the quantum SSH lattice, the so called chiral symmetry [19]. Due to the chiral symmetry, a mechanical dimer chain and a quantum SSH lattice share the same topological invariant, that is the Zak phase [124] – a special case of the general Berry phase [21]. Despite the similarities between the two systems there are some fundamental differences, for instance the mechanical chain is described by a system of second-order differential equations in time while the quantum SSH lattice is described by a system of first-order differential equations.

In this Chapter, we study the localization properties of the edge modes that are supported in a dimer mechanical chain, in the presence of disorder. We apply two forms of disorder, one that respects the chiral symmetry and a second one that does not. We compute the localization length numerically – using the transfer matrix method – and we find significant differences for the two forms of disorder. The results that are presented in this Chapter are based on ref. [125].

2.2 Topological features of a dimer chain

We begin this Chapter by reviewing the topological properties that a dimer mass-spring chain, as the one that is shown in Fig. 2.1, possesses [123]. This chain consists of same masses m that are coupled with each other with alternating springs of stiffnesses κ_1 and κ_2. All masses are attached to the ground with couplings of stiffness κ_0, which act in the horizontal direction. We denote as α the equilibrium distance between two neighboring masses. We also denote as u_n the displacement of the mass that is located at the site number n of the chain, from its equilibrium position. We consider only nearest neighbors interactions and therefore we obtain the following equations for the displacements u_n

$$m\frac{d^2u_n}{dt^2} = \kappa_{n+1}(u_{n+1} - u_n) - \kappa_n(u_n - u_{n-1}) - \kappa_n^0 u_n \tag{2.1}$$

where $\kappa_n = \kappa_1$ when n is odd, $\kappa_n = \kappa_2$ when n is even and $\kappa_n^0 = \kappa_0\ \forall n$.

Due to the dimer nature of this chain, we seek for solutions to Eq. (2.1) that have the plane wave form

$$u_n(t) = \begin{cases} A_1 e^{ikna - i\omega t} & ,\ n = 2s-1 \quad \text{with } s \in \mathbb{Z} \\ A_2 e^{ikna - i\omega t} & ,\ n = 2s \qquad \text{with } s \in \mathbb{Z} \end{cases} \tag{2.2}$$

where k is the wave number, ω is the frequency of the wave and A_1 (A_2) is the amplitude of oscillation of the masses that locate at odd (even) sites. By substituting Eq. (2.2) into Eq. (2.1) we arrive at the following eigenvalue problem

$$m\omega^2 \begin{pmatrix} A_1 \\ A_2 \end{pmatrix} = \tilde{\mathbf{D}}(k) \begin{pmatrix} A_1 \\ A_2 \end{pmatrix} = \frac{1}{m} \begin{pmatrix} \kappa_1 + \kappa_2 + \kappa_0 & -\kappa_2 - \kappa_1 e^{-2ika} \\ -\kappa_2 - \kappa_1 e^{2ika} & \kappa_1 + \kappa_2 + \kappa_0 \end{pmatrix} \begin{pmatrix} A_1 \\ A_2 \end{pmatrix}, \tag{2.3}$$

where the matrix $\tilde{\mathbf{D}}(k)$ is called the dynamical matrix. The eigenvalues of the dynamical matrix are the eigenfrequencies squared ω^2 and we find that these are given by

$$\omega^2_{(\pm)} = \frac{\kappa_1 + \kappa_2 + \kappa_0}{m} \pm \frac{1}{m}\sqrt{\kappa_1^2 + \kappa_2^2 + 2\kappa_1\kappa_2\cos(2ka)}\ . \tag{2.4}$$

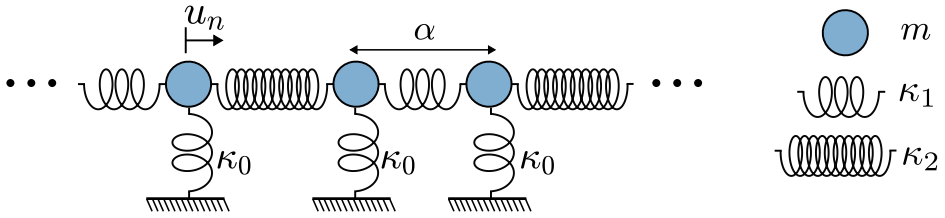

Figure 2.1: Schematic description of a dimer mass-spring chain with ground springs. The chain consists of of same masses m that are connected with alternating springs of stiffnesses κ_1 and κ_2 and are attached to the ground with springs of stiffnesses κ_0.

Equation (2.4) is the dispersion relation of the dimer chain and Fig. 2.2 illustrates this relation for $\kappa_1 > \kappa_2$ in (a), for $\kappa_1 = \kappa_2$ in (b) and for $\kappa_1 < \kappa_2$ in (c). When the two couplings are different, two bands appear in the dispersion relation that are separated by a gap.

We will now show that this infinite dimer chain has non-trivial topological features. As a first step we write the dynamical matrix in the basis that is formed by the identity $\mathbf{I}$ and the three Pauli matrices $\boldsymbol{\sigma}_i$, $i = x, y, z$

$$\tilde{\mathbf{D}}(k) = \frac{\kappa_1 + \kappa_2 + \kappa_0}{m}\mathbf{I} - \frac{\kappa_2 + \kappa_1 \cos(2ak)}{m}\boldsymbol{\sigma}_x - \frac{\kappa_1 \sin(2ak)}{m}\boldsymbol{\sigma}_y \ . \tag{2.5}$$

Notice that after the removal of the diagonal term $\omega_0^2 = \dfrac{\kappa_1 + \kappa_2 + \kappa_0}{m}$ from $\tilde{\mathbf{D}}(k)$, the remaining matrix obeys the anticommutative relation

$$\left\{\tilde{\mathbf{D}}(k) - \omega_0^2\mathbf{I}, \sigma_z\right\} = 0 \tag{2.6}$$

Due to the anticommutative relation given in Eq. (2.6), the infinite dimer chain is said to possess chiral symmetry which in turn induces non-trivial topological features. The topological features of this dimer chain are captured through the Zak phase [124], which is given by

$$\gamma_{Zak}^{(\pm)} = i\int_{-\frac{\pi}{2a}}^{\frac{\pi}{2a}} \left(\boldsymbol{A}^{(\pm)}\right)^{\dagger} \cdot \partial_k \boldsymbol{A}^{(\pm)} dk \ , \tag{2.7}$$

where $\boldsymbol{A}^{(\pm)}$ are the two eigenvectors of the dynamical matrix and the symbol +(-) denotes the upper (lower) band. Namely, the Zak phase characterizes each one of the two bands. And as we will now show, the Zak phase of each band remains unchanged as long as the band gap is open – it is therefore a topological invariant [20]. To show this, first we calculate the eigenvectors $\boldsymbol{A}^{(\pm)}$.

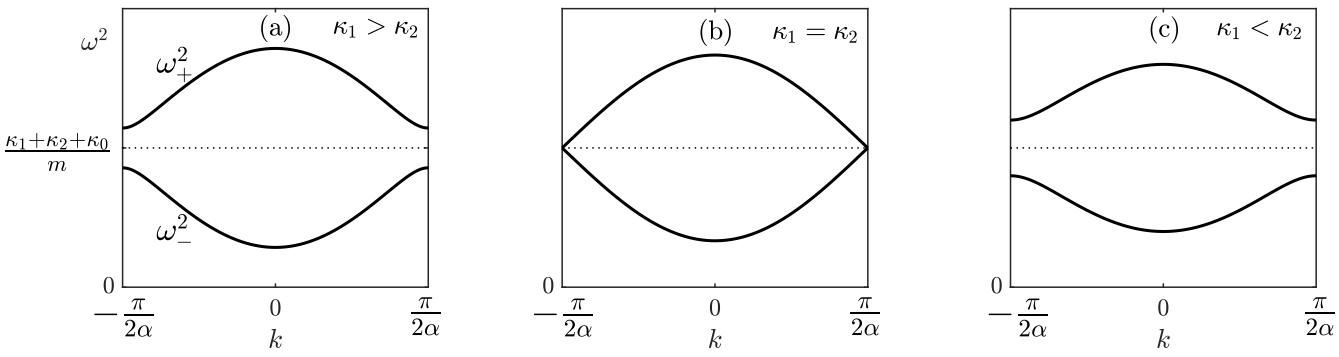

Figure 2.2: Dispersion relation of a diatomic dimer chain for (a) $\kappa_1 > \kappa_2$, (b) $\kappa_1 = \kappa_2$ and (c) $\kappa_1 < \kappa_2$.

These are easily found when we write $\tilde{\mathbf{D}}(k)$ in terms of the identity and the three Pauli matrices

$$\tilde{\mathbf{D}} = \omega_0^2 \mathbf{I} - \boldsymbol{d}\cdot\boldsymbol{\sigma} = \begin{pmatrix} \omega_0^2 - d_z & -d_x + id_y \\ -d_x - id_y & \omega_0^2 + d_z \end{pmatrix} . \tag{2.8}$$

We express the vector $\boldsymbol{d} = \begin{pmatrix} d_x & d_y & d_z \end{pmatrix}^T$ (^{T} denotes the transpose) in spherical coordinates as

$$\boldsymbol{d} = |\boldsymbol{d}|\boldsymbol{n} \quad \text{with} \quad \boldsymbol{n} = \begin{pmatrix} \cos\phi\sin\theta \\ \sin\phi\sin\theta \\ \cos\theta \end{pmatrix} \quad , \ 0 \le \phi < 2\pi \quad , \ 0 \le \theta \le \pi \ . \tag{2.9}$$

and with this notation the dynamical matrix gets the form

$$\tilde{\mathbf{D}} = \begin{pmatrix} \omega_0^2 - |\boldsymbol{d}|\cos\theta & -|\boldsymbol{d}|e^{-i\phi}\sin\theta \\ -|\boldsymbol{d}|e^{i\phi}\sin\theta & \omega_0^2 + |\boldsymbol{d}|\cos\theta \end{pmatrix} . \tag{2.10}$$

The two eigenvalues and two eigenvectors of the matrix that is given in Eq. (2.10) are

$$\lambda^{(\pm)} = \omega_0^2 \pm |\boldsymbol{d}| \tag{2.11}$$

and

$$\boldsymbol{A}^{(-)} = \begin{pmatrix} A_1^{(-)} \\ A_2^{(-)} \end{pmatrix} = \begin{pmatrix} \cos(\theta/2) \\ e^{i\phi}\sin(\theta/2) \end{pmatrix} \qquad , \qquad \boldsymbol{A}^{(+)} = \begin{pmatrix} A_1^{(+)} \\ A_2^{(+)} \end{pmatrix} = \begin{pmatrix} \sin(\theta/2) \\ -e^{i\phi}\cos(\theta/2) \end{pmatrix} . \tag{2.12}$$

We apply these results to the dynamical matrix that describes the dimer mass-spring chain (see Eq. (2.3)). We find that the angle θ is equal to $\pi/2$ and the vector $\boldsymbol{d}$ is given by

$$\boldsymbol{d} = \begin{pmatrix} \kappa_2 + \kappa_1\cos(2ka) \\ \kappa_1\sin(2ka) \\ 0 \end{pmatrix} . \tag{2.13}$$

Therefore, the vector $\boldsymbol{d}$ lies in the xy plane and can be represented by the complex number $|\boldsymbol{d}|e^{i\phi}$. Moreover, the two eigenvectors $\boldsymbol{A}^{\pm}$ of the dynamical matrix are equal to

$$\boldsymbol{A}^{(\pm)} = \frac{1}{\sqrt{2}} \begin{pmatrix} 1 \\ \mp e^{i\phi} \end{pmatrix} \tag{2.14}$$

suggesting that the Zak phase is given by

$$\gamma_{Zak}^{(\pm)} = -\frac{1}{2}\int_{-\frac{\pi}{2a}}^{\frac{\pi}{2a}} \frac{d\phi}{dq} dq = -\frac{1}{2}\left(\phi(\pi/2a) - \phi(-\pi/2a)\right) + 2\pi m \quad , \ m = 0, \pm 1, \pm 2, ... \tag{2.15}$$

To proceed further, we remind the definition of the winding number of a curve (from complex analysis). The winding number of a curve around a point z_0 gives the number of times this curve passes around that point and it is given by

$$n(z_0) = \frac{1}{2\pi i} \oint \frac{dz}{z - z_0} \ ,$$

meaning that the winding number of a curve around the origin is equal to

$$n = \frac{1}{2\pi i} \oint \frac{dz}{z} \ . \tag{2.16}$$

By writing z in polar coordinates: $z = re^{i\phi} \Rightarrow dz = e^{i\phi}dr + ire^{i\phi}d\phi \Rightarrow \frac{dz}{z} = \frac{dr}{r} + id\phi$, we obtain that $\frac{dz}{z} = d(\ln r) + id\phi$. The total change of $\ln r$ is zero around a closed path so the winding number of a curve is equal to

$$n = \frac{1}{2\pi i} \oint id\phi(k) = \frac{1}{2\pi} \left(\phi(\pi/2a) - \phi(-\pi/2a)\right) \ . \tag{2.17}$$

Thus, we immediately obtain that the Zak phase is related to the winding number of the $\boldsymbol{d}(k)$ vector and we only need to study the variation of this vector for $k \in [-\pi/2a, \pi/2a)$. In Fig. 2.3 we present this variation for $\kappa_1 > \kappa_2$ in (a), for $\kappa_1 = \kappa_2$ in (b) and for $\kappa_1 < \kappa_2$ in (c). We observe that for $\kappa_1 > \kappa_2$ the vector $\boldsymbol{d}(k)$ has a winding number equal to 1 and therefore the Zak phase is equal to π for both bands. For $\kappa_1 < \kappa_2$ the winding number is zero meaning that the Zak phase is also zero for both bands. So the Zak phase number is a topological invariant.

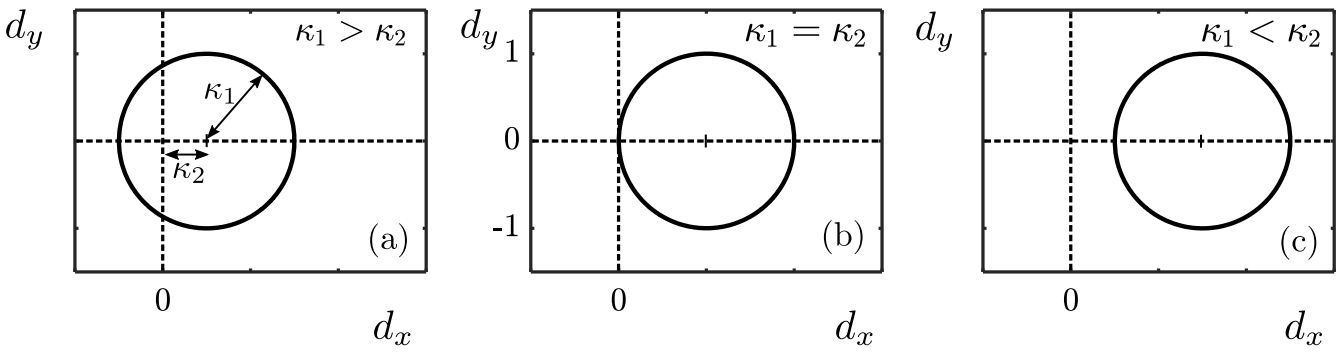

Figure 2.3: Variation of the vector $\boldsymbol{d}$ for $k \in [-\pi/2a, \pi/2a)$ when (a) $\kappa_1 > \kappa_2$, (b) $\kappa_1 = \kappa_2$ and (c) $\kappa_1 < \kappa_2$.

2.3 Finite dimer chain

A question that naturally arises at this point is what are the consequences of the non-trivial topology that the infinite dimer chain possesses. To give an answer to this question we will study in this Section the finite dimer chain that is illustrated in Fig. 2.4 (it is the finite counterpart of the infinite chain that is shown in Fig. 2.1). As we shall see in the following , this finite dimer chain supports edge modes, due to the non-trivial topological properties. Notice that the finite chain shown in Fig. 2.4 consists of an even number N of masses m, while the first and the last masses are connected to walls (fixed boundary conditions are used).

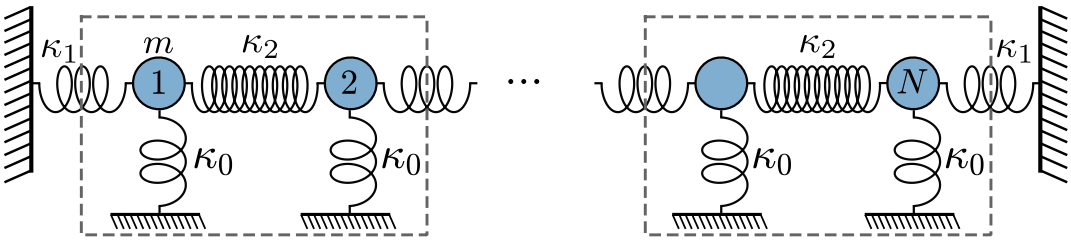

Figure 2.4: Schematic description of a finite dimer mass-spring chain with an even number N of masses. Fixed boundary conditions are used.

2.3.1 Equations of motion

We denote as $u_1,\ u_2,\ ...,\ u_N$ the displacements of the masses that locate at the sites number $1,\ 2, ..., N$ of the finite chain from their equilibrium positions. Apart from the first and the last masses (that are connected to the walls), the displacements of all the other masses, namely the u_n with $n = 2, ...N-1$, are given by Eq. (2.1). The equations for the displacements of the first the last masses are

$$m\ddot{u}_1 = -\kappa_1 u_1 - \kappa_2(u_1 - u_2) - \kappa_0 u_1, \tag{2.18}$$

$$m\ddot{u}_N = \kappa_2(u_{N-1} - u_N) - \kappa_1 u_N - \kappa_0 u_N. \tag{2.19}$$

We can rearrange the equations of all the displacements u_n with $n = 1, ...N$ in the matrix form

$$\ddot{\boldsymbol{u}}(t) + \mathbf{D}\boldsymbol{u}(t) = 0 \tag{2.20}$$

where $\boldsymbol{u} = \begin{pmatrix} u_1 & u_2 & \cdots & u_N \end{pmatrix}^T$ is the vector of displacements and $\mathbf{D}$ is the dynamical matrix,

$$\mathbf{D} = \frac{1}{m}\begin{pmatrix} \kappa_1+\kappa_2+\kappa_0 & -\kappa_2 & 0 & & ... \\ -\kappa_2 & \kappa_1+\kappa_2+\kappa_0 & -\kappa_1 & 0 & ... \\ 0 & -\kappa_1 & \kappa_1+\kappa_2+\kappa_0 & -\kappa_2 & ... \\ & & ... & & \\ & & ... & -\kappa_1 & \kappa_1+\kappa_2+\kappa_0 \quad -\kappa_2 \\ & & ... & 0 & -\kappa_2 \quad \kappa_1+\kappa_2+\kappa_0 \end{pmatrix}. \tag{2.21}$$

The dynamical matrix $\mathbf{D}$ possesses chiral symmetry as well, since it obeys a similar anticommutative relation as the dynamical matrix of the infinite chain does (see Eq. (2.6). Specifically, it holds

$$\left\{\mathbf{D} - \frac{\kappa_1 + \kappa_2 + \kappa_0}{m}\mathbf{I}_N, \mathbf{\Sigma}_z\right\} = 0, \tag{2.22}$$

where

$$\mathbf{\Sigma}_z = \begin{pmatrix} 1 & 0 & 0 & 0 & \cdots & & \cdots & 0 \\ 0 & -1 & 0 & 0 & \cdots & & \cdots & 0 \\ \vdots & & & & \ddots & & & \vdots \\ 0 & \cdots & & \cdots & 0 & 0 & 1 & 0 \\ 0 & \cdots & & \cdots & 0 & 0 & 0 & -1 \end{pmatrix} . \tag{2.23}$$

The matrix $\mathbf{\Sigma}_z$ is known as the chiral operator.

2.3.2 Eigenanalysis

To obtain the frequency spectrum of the finite chain, we follow a similar procedure with the one that we followed at the infinite chain. Namely, we substitute solutions of plane wave form $\boldsymbol{u}(t) = \boldsymbol{u}e^{i\omega t}$ at the equations of motion (Eq. (2.20)) and we get that

$$\omega_n^2 \boldsymbol{u}_n = \mathbf{D}\boldsymbol{u}_n, \tag{2.24}$$

The ω_n are the eigenfrequencies and the $\boldsymbol{u}_n$ are the eigenmodes of the finite chain ($n = 1, 2..., N$).

In Fig. 2.5(a)-(c) we present the eigenfrequencies ω_n (calculated numerically) of a chain with $N = 50$ masses in three different scenarios. In (a) we set $\kappa_1 < \kappa_2$, in (b) $\kappa_1 = \kappa_2$ and in (c) $\kappa_1 > \kappa_2$. In all cases we set $m = 0.01$, $\kappa_0 = 5$ and $\kappa_1 = 1$[1]. In Fig. 2.5(a) we set $\kappa_2 = 1.5$ - notice the band structure that is formed. In Fig. 2.5(b) we set $\kappa_2 = 1$ - there is no gap in this case. Finally, in Fig. 2.5(c) we set $\kappa_2 = 0.5$ - we find two modes whose frequencies lie in the band gap. These two modes are called edge modes (we note here that one edge mode is always supported in the chain when N is odd – see next Section). In Fig. 2.5(d) and (e) we present their profiles. Notice that these modes are localized at the two edges of the chain. This localized profile of the edge modes holds as soon as $\kappa_1 > \kappa_2$ and is more localized the more the stiffness values κ_1 and κ_2 differ.

The frequencies of the two edge modes that are illustrated in Fig. 2.5(c) are not exactly the same. There is a frequency splitting, meaning that the two eigenfrequencies are not exactly located at $\omega_0 = \sqrt{(\kappa_1 + \kappa_2 + \kappa_0)/m}$ but at ω_0^+, ω_0^-. This frequency splitting is decreasing as the size of the chain is increasing. Therefore, for a large chain there is a sufficiently small splitting and thus we have a "degeneracy" of the eigenmodes. In that case, the two edge modes could be localized at opposite edges of the chain, but each mode at one edge only. In Fig. 2.6 we present an example. We use a chain that consists of $N = 500$ masses (we set $\kappa_1 = 1$, $\kappa_2 = 0.5$ and $\kappa_0 = 5$). In Fig. 2.6(a) we see the eigenfrequencies ω_n of this chain and in Fig. 2.6(b) and (c) we see the profiles of the two edge modes. Notice that these modes are localized only at the one side of the chain in this

[1]In all the following numerical results, we set the value of m at 0.01 in arbitrary units $\bar{m}$. We also measure the stiffnesses of the couplings in arbitrary units $\bar{\kappa}$.

case. A closer look at these profiles (see the insets of Fig. 2.6(b) and (c)) reveals that only the masses that locate at sites with n even or n odd are excited. This is an known consequence of the chiral symmetry [20].

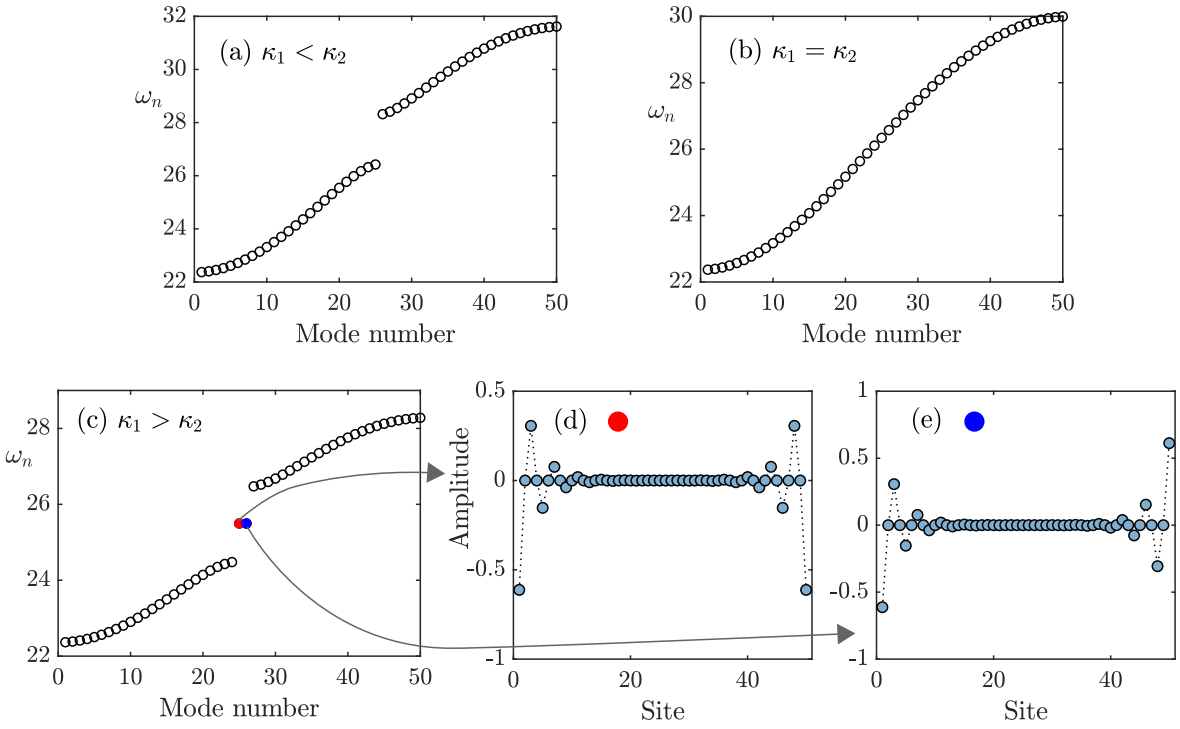

Figure 2.5: In all cases we use a finite chain that consists of $N = 50$. We set $m = 0.01$, $\kappa_1 = 1$ and $\kappa_0 = 5$. Fixed boundary conditions are used. Shown are the eigenfrequencies ω_n for (a) $\kappa_2 = 1.5$ (b) $\kappa_2 = 1$ and (c) $\kappa_2 = 0.5$. (d) and (e) Profile of the two edge modes.

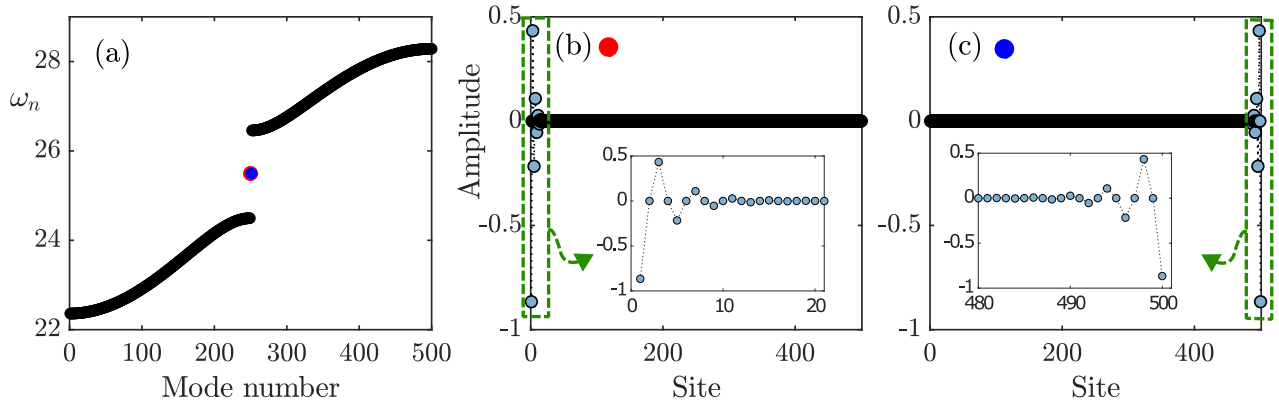

Figure 2.6: (a)-(c) Same as Fig. 2.5(c)-(e) but for a chain with $N = 500$ masses. The edge modes are localized only at the one side of the chain due to "degeneracy". Also, due to the chiral symmetry, only the masses that locate at sites with n even or n odd are excited in each case - see the insets.

2.4 Disorder analysis

A known characteristic of the edge modes is their robustness against disorder that respects the chiral symmetry [20]. In this Section, we aim to illustrate this robustness. For this, we consider that the couplings of the chain that is illustrated in Fig. 2.4 are randomly varied. Namely, we apply disorder. We apply two forms of disorder: the first retains the chiral symmetry of the chain, while the second form not.

2.4.1 Chiral disorder

We begin with the form of disorder that retains the chiral symmetry of the chain. Meaning that the dynamical matrix of the finite disordered chain satisfies the anticimmutative relation that is given in Eq. (2.22). In order for this matrix to satisfy this anticimmutative relation, it must have the same diagonal elements. However, after a careful look at the dynamical matrix that is given in Eq. (2.21) – the dynamical matrix in the clean limit (no disorder) – we conclude that we cannot alter only the two couplings κ_1 and κ_2 if we want the diagonal terms of the dynamical matrix to be the same. We have to alter the ground springs κ_0 as well (if we restrict ourselves to same masses, namely disorder only on the stiffnesses).

First of all, we consider that the stiffnesses of the couplings κ_1 and κ_2 are randomly varied and are given by

$$\kappa_n \to \begin{cases} \kappa_1 + \delta_n = \kappa_1 + W_1\epsilon_n & \text{if } n \text{ is odd} \\ \kappa_2 + \delta_n = \kappa_2 + W_2\epsilon_n & \text{if } n \text{ is even} \end{cases} \tag{2.25}$$

where ϵ_n are random numbers, uniformly distributed in the interval $[-1, 1]$ and $W_{1,2}$ are the disorder strengths. In order to keep the chiral symmetry, the ground springs must change in the following way

$$\kappa_n^0 \to \kappa_0 - \delta_n - \delta_{n+1}. \tag{2.26}$$

A schematic illustration of this form of disorder is given in Fig. 2.7(a).

The dynamical matrix of this disordered chain is given by

$$\mathbf{D} = \frac{1}{m}\begin{pmatrix} \kappa_1+\kappa_2+\kappa_0 & -\kappa_2-\delta_2 & 0 & & \dots & & \\ -\kappa_2-\delta_2 & \kappa_1+\kappa_2+\kappa_0 & -\kappa_1-\delta_3 & 0 & \dots & & \\ 0 & -\kappa_1-\delta_3 & \kappa_1+\kappa_2+\kappa_0 & -\kappa_2-\delta_4 & \dots & & \\ & & \dots & & & & \\ & & \dots & -\kappa_1-\delta_{N-1} & \kappa_1+\kappa_2+\kappa_0 & -\kappa_2-\delta_N & \\ & & \dots & 0 & -\kappa_2-\delta_N & \kappa_1+\kappa_2+\kappa_0 & \end{pmatrix}. \tag{2.27}$$

Notice that this dynamical matrix obeys the anticimmutative relation that is given in Eq. (2.22), since its diagonal elements are the same, and is therefore chiral symmetric.

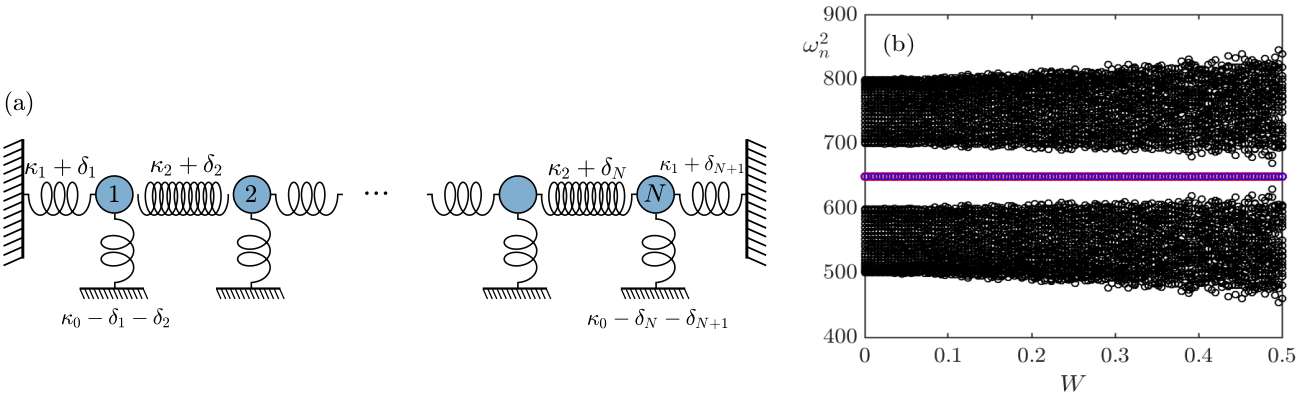

Figure 2.7: (a) Schematic description of chiral disorder. (b) Eigenfrequencies squared of a chain with $N = 50$ masses as a function of the disorder strength $W = W_2 = 2W_1$. We set $m = 0.01$, $\kappa_1 = 1$, $\kappa_2 = 0.5$, $\kappa_0 = 5$,

In Fig. 2.7(b) we present the eigenfrequencies squared ω_n^2 of a chain with $N = 50$ masses, $\kappa_1 = 1$, $\kappa_2 = 0.5$, $\kappa_0 = 5$. We also set the disorder strengths W_1 and W_2 at $W = W_2 = 2W_1$ (this choice is based on the fact that $\kappa_1/\kappa_2 = 2$ in this example). From Fig. 2.7(b) we get that: 1) the frequencies of the edge modes do not change with increasing the disorder strength 2) all the eigenfrequencies squared are symmetric with respect to the center of the gap. These two results are due to the preservation of the chiral symmetry. We note here that we present the eigenfrequencies squared, since these are the eigenvalues of the dynamical matrix.

2.4.2 Non-correlated disorder

Let us now study the case of non-correlated disorder. In this form of disorder we keep the ground springs unperturbed (their stiffness is equal to κ_0), while we consider that the springs κ_1 and κ_2 are perturbed again independently and their stiffnesses are given by Eq. (2.25). A schematic description of this form of disorder is given in Fig. 2.8(a).

In this case, the dynamical matrix takes the form

$$\mathbf{D} = \frac{1}{m}\begin{pmatrix} \kappa_1+\kappa_2+\kappa_0+\Delta_1 & -\kappa_2-\delta_2 & 0 & & \dots \\ -\kappa_2-\delta_2 & \kappa_1+\kappa_2+\kappa_0+\Delta_2 & -\kappa_1-\delta_3 & 0 & \dots \\ 0 & -\kappa_1-\delta_3 & \kappa_1+\kappa_2+\kappa_0 & -\kappa_2-\delta_4 & \dots \\ & & \dots & & \\ & & \dots & -\kappa_1-\delta_{N-1} & \kappa_1+\kappa_2+\kappa_0 & -\kappa_2-\delta_N \\ & & \dots & 0 & -\kappa_2-\delta_N & \kappa_1+\kappa_2+\kappa_0+\Delta_N \end{pmatrix}, \tag{2.28}$$

where $\Delta_n = \delta_n + \delta_{n+1}$. Notice that diagonal elements of this matrix are not the same and therefore it does not obey the anticimmutative relation that is given in Eq. (2.22).

In Fig. 2.8(b) we show the eigenfrequencies squared ω_n^2 of a chain with non-correlated disorder. The chain consists of $N = 50$ masses and we set $\kappa_1 = 1$, $\kappa_2 = 0.5$, $\kappa_0 = 5$ and the disorder strengths at $W = W_2 = 2W_1$. Notice that all the eigenfrequencies are affected from this type of disorder.

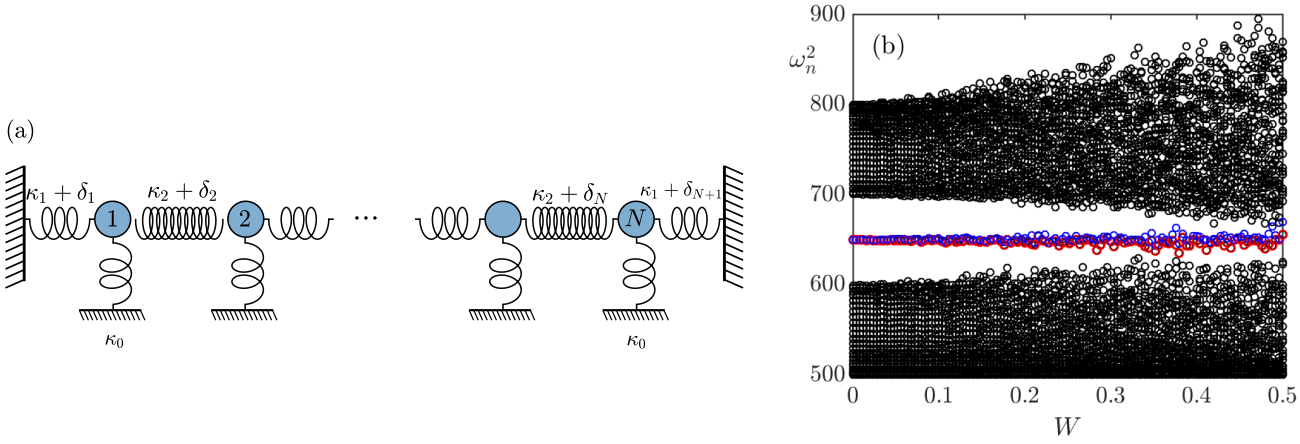

Figure 2.8: (a) Schematic description of non-correlated disorder. (b) Eigenfrequencies squared of a chain with $N = 50$ masses as a function of the disorder strength $W = W_2 = 2W_1$. We set $m = 0.01$, $\kappa_1 = 1$, $\kappa_2 = 0.5$, $\kappa_0 = 5$,

2.5 Localization properties

In this part, we study the localization length Λ at the mid-gap frequency ω_0 for a disordered chain. We compute the localization length numerically by employing the transfer matrix method. For that, we rewrite Eq. (2.1) as

$$\begin{pmatrix} u_{n+1} \\ u_n \end{pmatrix} = \mathbf{T}_n \begin{pmatrix} u_n \\ u_{n-1} \end{pmatrix}, \tag{2.29}$$

where $\mathbf{T}_n$ is the transfer matrix and is given by

$$\mathbf{T}_n = \begin{pmatrix} \dfrac{\kappa_{n+1} + \kappa_n + \kappa_n^0 - m\omega_0^2}{\kappa_{n+1}} & -\dfrac{\kappa_n}{\kappa_{n+1}} \\ 1 & 0 \end{pmatrix}. \tag{2.30}$$

In order to compute the localization length, we calculate the Lyapunov exponents γ_1 and γ_2 using the typical numerical schemes that are described in [126]. We found that $\gamma_1 \approx -\gamma_2 = \gamma$. The localization length is then given by

$$\Lambda = \frac{1}{\gamma}. \tag{2.31}$$

A more detailed discussion regarding the numerical computation of the localization length Λ is given in Appendix B.

As an illustration, we compute the localization length at the mid gap frequency ω_0 of a non-disordered chain. We set $\kappa_1 = 1$ and we compute the localization length Λ as we vary the stiffness κ_2 from 0.5 to 1.5. The transfer matrix was iterated 10^6 times. The results are illustrated in Fig. 2.9. Notice that when $\kappa_2 = \kappa_1 = 1$ the localization length diverges. This is expected since for $\kappa_1 = \kappa_2$

there is no gap at the frequency spectrum. More specifically, for $\kappa_1 = \kappa_2$ and at the frequency ω_0 an extended state exists and thus the assumption of an exponentially localized solution results in this divergence. We note here that in this clean limit (no disorder) the localization length can be calculated analytically and is equal to $\Lambda = \dfrac{2}{|\ln(\kappa_1/\kappa_2)|}$, which matches with the numerical results that are illustrated in Fig. 2.9.

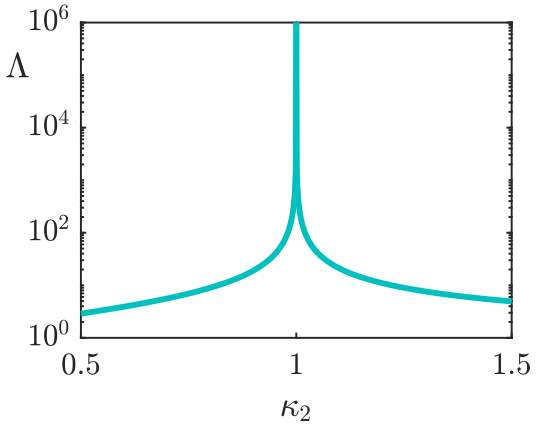

Figure 2.9: Numerical computation (with the transfer matrix method) of the localization length at the mid gap frequency ω_0.

2.5.1 Chiral disorder

We begin this part by illustrating the numerical results for the case of the chiral disorder. We note first that in the following we set the disorder strengths W_1 and W_2 at $W = W_2 = 2W_1$. We also set the stiffness of the coupling κ_1 at 1.

We calculate the localization length Λ at the mid-gap frequency, using the transfer matrix method, for each pair of κ_2 and W. The result is shown in Fig. 2.10. We stress here that the transfer matrix was iterated 10^6 times at each point of the grid and a numerical method for correcting the rounding errors was applied (see Appendix B). Clearly, there is a critical line in the plane (W, κ_2) in which the localization length diverges [127]. In the following, in order to get an insight into this result, we will see the frequency spectrum and the profile of the modes with frequency ω_0 for multiples pairs of (W, κ_2). But before that, we will compute the localization length analytically, since for the chiral disorder this is possible.

We note first that for the case of the chiral disorder we obtain the following solution at ω_0

$$\begin{aligned} u_{2m-1} &= (-1)^{m-1} \prod_{n=1}^{m-1} \frac{\kappa_{2n}}{\kappa_{2n+1}} u_1 \\ u_{2m} &= (-1)^{m-1} \prod_{n=1}^{m-1} \frac{\kappa_{2n+1}}{\kappa_{2n+2}} u_2, \end{aligned} \tag{2.32}$$

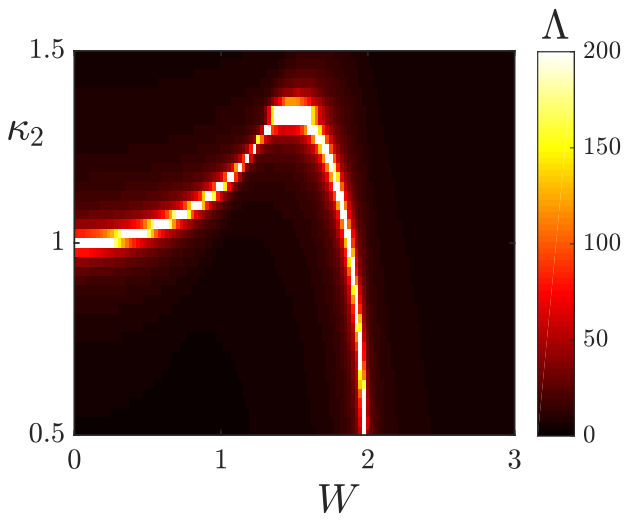

Figure 2.10: Shown here is the localization length for the chiral disorder case, calculated numerically from the transfer matrix method.

where the κ_n's are given by Eq. (2.25). Then, assuming an exponential form for these solutions we obtain that the localization length of these solutions is given by

$$\Lambda^{-1} = \left| \lim_{m\to\infty} \frac{1}{m} \sum_{n=1}^{m} \left(\ln|\kappa_1 + W_1\epsilon_n| - \ln|\kappa_2 + W_2\epsilon'_n| \right) \right| \tag{2.33}$$

where ϵ_n and ϵ'_n are random numbers, uniformly distributed in the interval $[-1, 1]$. According to the ergodic theorem (see ref. [55]) one obtains the following expression for Λ

$$\Lambda^{-1} = \left| \frac{1}{2} \frac{\int_{-1}^{1} d\epsilon \int_{-1}^{1} d\epsilon' \left(\ln|\kappa_1 + W_1\epsilon| - \ln|\kappa_2 + W_2\epsilon'| \right)}{4} \right|, \tag{2.34}$$

where an ensemble average has been used. After performing the integration we get that

$$\Lambda^{-1} = \frac{1}{4} \left| \ln \left[\frac{|\kappa_1 + W_1|^{(\kappa_1/W_1+1)}}{|\kappa_1 - W_1|^{(\kappa_1/W_1-1)}} \frac{|\kappa_2 - W_2|^{(\kappa_2/W_2-1)}}{|\kappa_2 + W_2|^{(\kappa_2/W_2+1)}} \right] \right|. \tag{2.35}$$

In Fig. 2.11 we compare the numerical results with the analytic ones. The blue line shows the points in the (W, κ_2) plane in which the $\Lambda(\omega_0)$ diverges (the blue line corresponds to the analytic expression of Eq. (2.35)). Clearly, the analytic results match perfectly with the numerical ones.

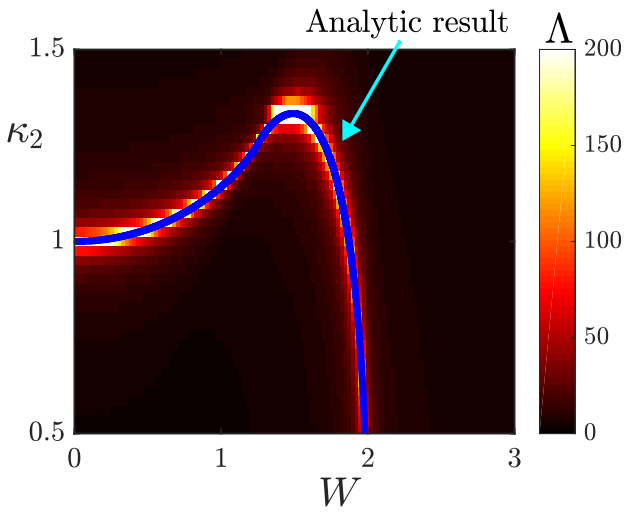

Figure 2.11: Comparison between the transfer matrix method and the analytic result.

In order to get an insight into the results, we analyze the eigenfrequencies and the center modes of a chain with $N = 500$ masses for three sets of W and κ_2. The positions of these three sets in the (W, κ_2) plane are shown in Fig. 2.12 with the three crosses: two before and one after the critical line in which the localization diverges. For each of these three sets we consider one chiral disorder realization and in Fig. 2.12 we present the eigenfrequencies of the chain and the profiles of the two center modes.

The panels (a)-(c) of Fig. 2.12 correspond to $\kappa_2 = 0.6$ and $W = 0.25$ (indicated with the yellow cross). Specifically, in the panel (a) we see the eigefrequencies and in the panels (b) and (c) we see the profiles of the two center modes. Notice that for this set of (W, κ_2), we find again a gap at the frequency spectrum and the two center modes are localized at the edges of the chain. Next, we increase the disorder strength. The panels (d)-(e) correspond to one disorder realization with $W = 1.25$ and $\kappa_2 = 0.6$ (this set is indicated with the green cross). Notice that the two center modes are still localized at the edges of the chain. We continue increasing the disorder strength and the panels (g)-(i) correspond to one disorder realization with $W = 2.5$ and $\kappa_2 = 0.6$ (this set is indicated with the magenta cross). In this case, the two center modes are localized anywhere at the chain.

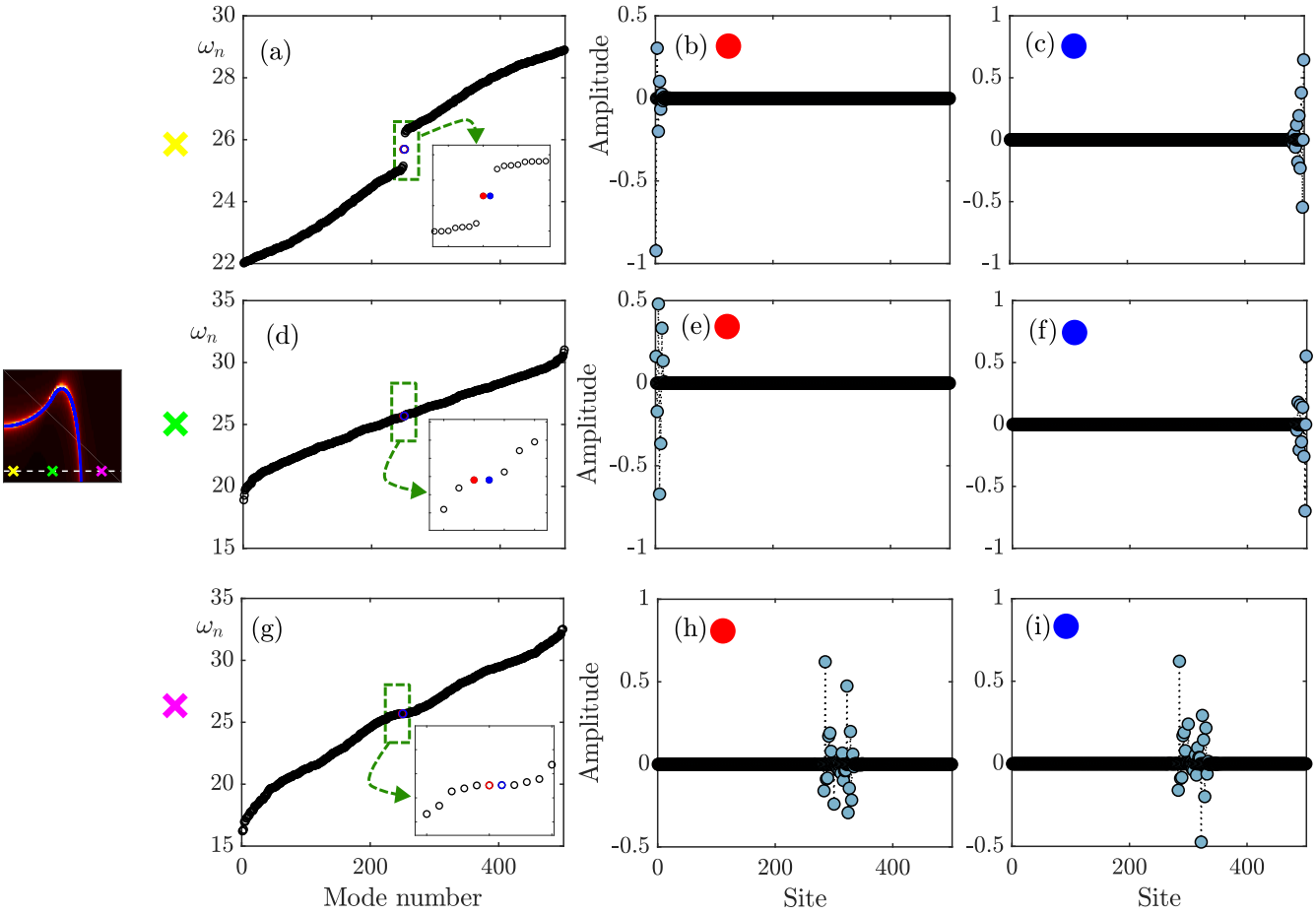

Figure 2.12: (a)-(c) Eigenfrequencies and profile of the two center modes for one disorder realization under chiral disorder. We set $\kappa_1 = 1$, $\kappa_2 = 0.5$ and the disorder strengths at $W = W_2 = 2W_1 = 0.25$. Notice that the two center modes are localized at the edges of the chain and there is a band gap in the frequency spectrum. (d)-(f) Same as (a)-(c) but we set the disorder strengths at $W = W_2 = 2W_1 = 1.25$. The two center modes are still localized at the edges of the chain but the gap in the frequency spectrum is closed. (g)-(i) Same as (a)-(c) but we set the disorder strengths at $W = W_2 = 2W_1 = 2.5$. The two center modes are localized at the center of the chain and the gap in the frequency spectrum is closed.

More insight is provided in Fig. 2.13. Here we show only the profile of the two center modes for three sets of (W, κ_2) that are indicated with the three crosses. In all cases we set $\kappa_2 = 1.05$ (white dashed line). In Fig. 2.13(a) and (b) we set $W = 0.25$, in Fig. 2.13(c) and (d) we set $W = 1.25$ and finally in Fig. 2.13(e) and (f) we set $W = 2.5$. Notice that the center modes in the panels (a), (b), (e) and (f) are localized in the interior of the chain. Yet, in Fig. 2.13(b) and (c) the two center modes are localized at the edges of the chain.

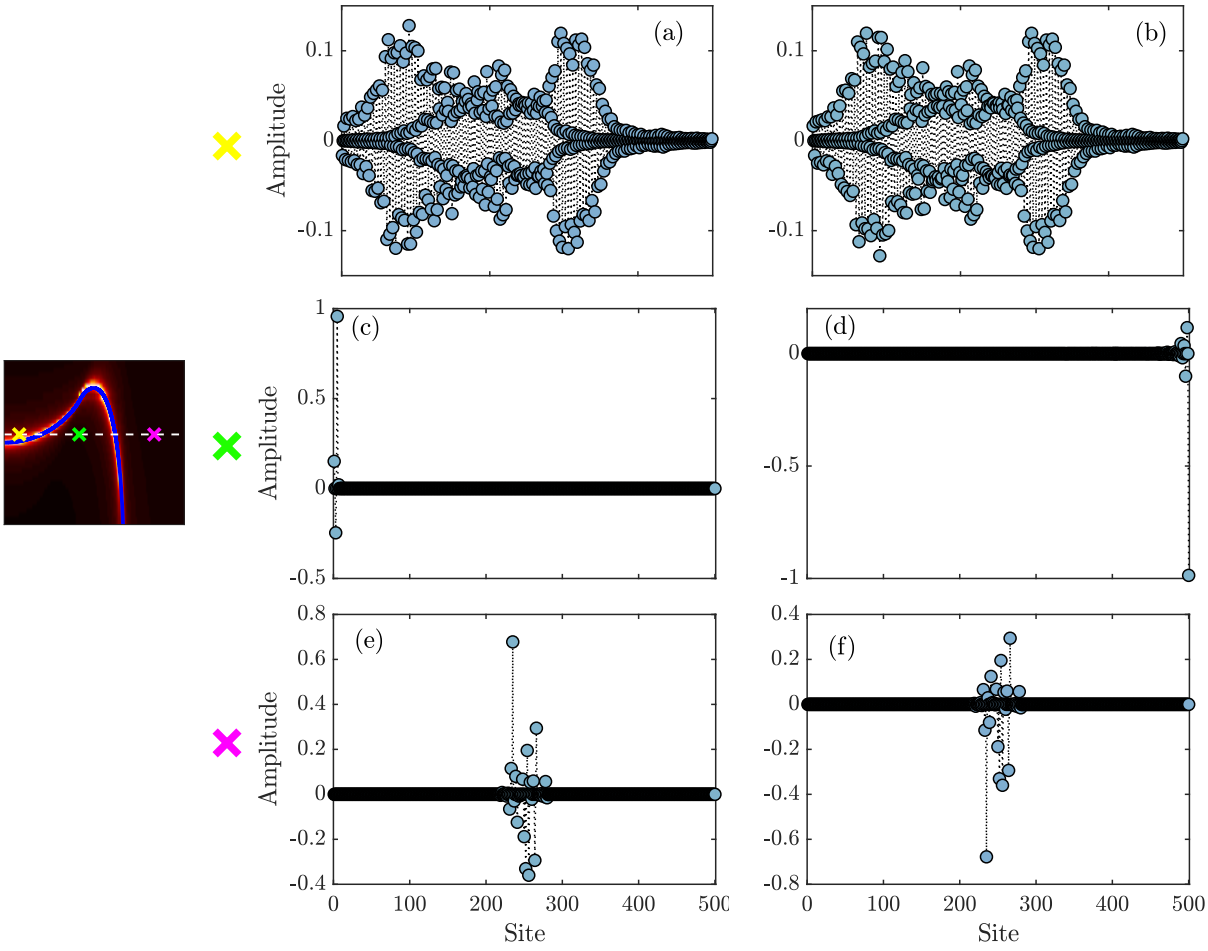

Figure 2.13: (a)-(b) Profile of the two center modes for one disorder realization under chiral disorder. We set $\kappa_1 = 1$, $\kappa_2 = 1.05$ and the disorder strengths at $W = W_2 = 2W_1 = 0.25$. Notice that the two center modes are localized at the center of the chain. (c)-(d) Same as (a)-(b) but we set the disorder strengths at $W = W_2 = 2W_1 = 1.25$. Notice that the two center modes are localized at the edges of the chain. (e)-(f) Same as (a)-(b) but we set the disorder strengths at $W = W_2 = 2W_1 = 2.5$. Notice that the two center modes are localized at the center of the chain again.

To sum up, in this part we found that there is a critical line in plane (W, κ_2) in which the localization length (calculated at the mid-gap frequency) diverges. This critical line divides the (W, κ_2) in two regions. We found that for pairs of W and κ_2 that lie in the "lower side" region the center modes are localized at the edges of the chain. But for pairs of W and κ_2 that lie in the "upper side" region we found that the center modes are localized anywhere in the chain: strong chiral disorder destroys the topological protection of the center modes. The calculation of a special topological index, called topological local marker [127], shows that the "lower side" region is topologically non-trivial and the "upper side" region is topologically trivial. Therefore, the chiral disorder introduces a topological transition from trivial to non-trivial.

2.5.2 Non-correlated disorder

We discuss now the effect of non-correlated disorder. Namely, we remove the disorder on the ground springs and in this way we break the chiral symmetry of the system. We begin again by calculating numerically the localization length (using the transfer matrix method), at the mid-gap frequency ω_0, for each pair of κ_2 and W (the transfer matrix was iterated 10^6 times at each point of the grid). Once more, we fix the disorder strengths at $W = W_2 = 2W_1$ and the stiffness of κ_1 at 1. The results are illustrated in Fig. 2.14. Notice that there is no signature of divergence of the $\Lambda(\omega_0)$ in this case. We note here that for the non-correlated disorder case, we cannot find a closed form expression for the displacements u_n with $n = 1, 2, ..., N$ as we did for the chiral disorder (see Eq. (2.35)). Therefore, we cannot compute the localization length analytically this time.

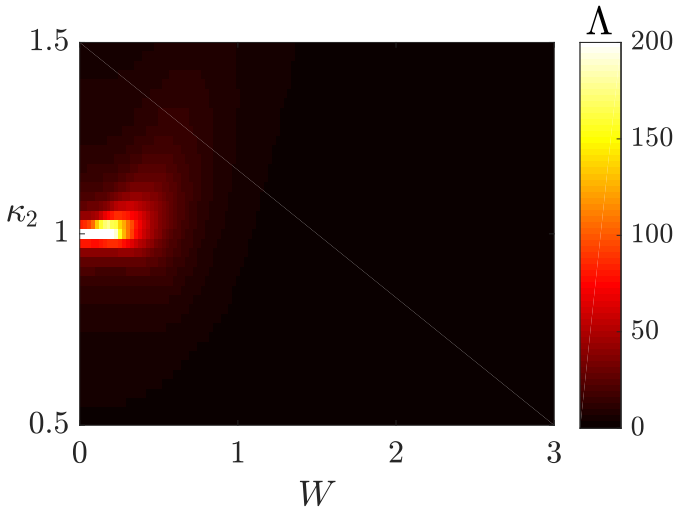

Figure 2.14: Shown here is the localization length for the non-correlated disorder case, computed numerically from the transfer matrix method.

In Fig. 2.15 we analyze again the eigenfrequencies and the two center eigenmodes of a chain with $N = 500$ masses as a function of the disorder strength. We use the same sets of W and κ_2 with the ones that we also used in Fig. 2.10. Specifically, in Fig. 2.15(a)-(c) we set $\kappa_2 = 0.6$ and $W = 0.25$. Notice that there is a gap in the frequency spectrum and the two center modes are localized at the edges of the chain. In Fig. 2.15(d)-(f) we set $\kappa_2 = 0.6$ and $W = 1.25$. Notice that the two center modes are localized in the interior of the chain. This is in contrast with the case of the chiral disorder. Recall that in that form of disorder, for this set of (W, κ_2), the two center modes were localized at the edges of the chain. Next, we increase the strength of the disorder. We consider $W = 2.5$ (and $\kappa_2 = 0.6$). Notice that the center modes are localized again anywhere in the chain.

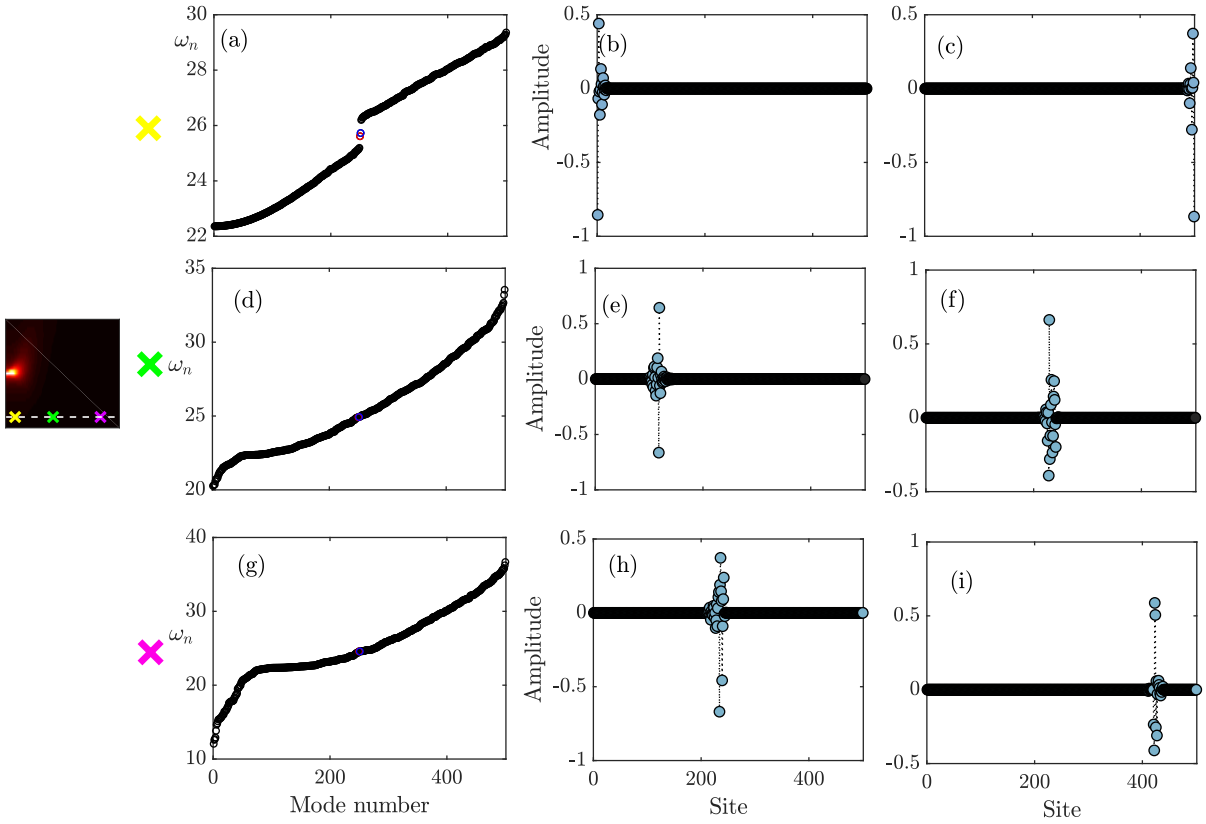

Figure 2.15: (a)-(c) Eigenfrequencies and profile of the two center modes for one disorder realization under non-correlated disorder. We set $\kappa_1 = 1$, $\kappa_2 = 0.5$ and the disorder strengths at $W = W_2 = 2W_1 = 0.25$. Notice that the two center modes are localized at the edges of the chain and there is a band gap in the frequency spectrum. (d)-(f) Same as (a)-(c) but we set the disorder strengths at $W = W_2 = 2W_1 = 1.25$. The two center modes localized at the center of the chain and the gap in the frequency spectrum is closed. (g)-(i) Same as (a)-(c) but we set the disorder strengths at $W = W_2 = 2W_1 = 2.5$. The two center modes are localized again at the center of the chain and the gap in the frequency spectrum is closed.

2.6 Concluding remarks

In this Chapter we have shown that a finite dimer mass-spring chain is chiral symmetric and due to this symmetry it supports edge modes – modes that are localized at the edges of the chain and whose frequency lies at the middle of the frequency spectrum. We have considered that such a dimer chain was disordered and we have explored the impact of chiral disorder (disorder that retains the chiral symmetry of the chain) and of uncorrelated disorder (disorder that breaks the chiral symmetry of the chain). Using the transfer matrix method, we calculated the localization length at the middle of the frequency spectrum and we concluded that a strong chiral disorder can make a topologically non-trivial chain topologically trivial and vice versa. These conclusions are supported by the calculation of proper topological indices like the topological local marker [125, 127].

Chapter 3

State transfer in periodic time-varying mechanical lattices

3.1 Introduction

In Chapter 2, we saw that a finite mass spring chain that consists of an even number of masses, supports either two edge modes or none, depending on the stiffnesses of the spring couplings. On the other hand, in a dimer chain with an odd number of masses, one edge mode is always supported, which is localized either at the left or at the right side of the chain, again depending on these stiffnesses.

Our goal in this Chapter is to transfer such an edge mode that is always supported in a dimer chain with an odd number of masses, from the chain's one end to its other. To accomplish such a state transfer, we let the spring couplings to vary with time and to exchange values between the initial and the final times of the transfer process. Furthermore, we use the CRAB optimal control theory [128, 129] in order to achieve this transfer fast. The results that are presented in this Chapter are based on ref. [130].

3.2 Finite dimer chain with odd masses

Our model in this chapter is similar to the one of chapter 2. It is again a 1D finite dimer mass-spring chain. All the masses m are the same and are coupled with each other with alternating springs of stiffnesses κ_1 and κ_2. We impose again fixed boundary conditions at both ends of the chain. However, the chain that we consider here consists of an odd number N of masses (the chain of chapter 2 consists of an even number of masses) and these masses are not attached to the ground. For a schematic illustration of such a setup see Fig. 3.1. As we shall see below, this odd sized chain always supports one edge mode as long as $\kappa_1 \neq \kappa_2$.

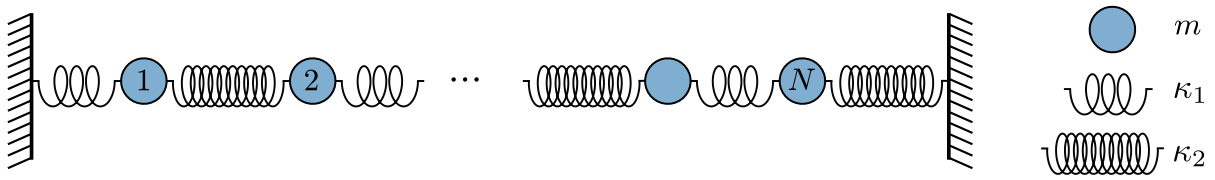

Figure 3.1: Schematic description of a finite dimer chain that consists of an odd number N of same masses m and alternating springs of stiffnesses κ_1 and κ_2. Fixed boundary conditions are used.

3.2.1 Small vibrations

Our goal until the end of this section is to derive the eigenmodes that are supported in this odd-sized dimer chain. The analysis that we follow is very similar with the corresponding one in Chapter 2. Namely, we consider small vibrations of this dimer chain and we denote as u_n with $n = 1, 2, ..., N$ the displacement of the mass that locates at the site number n of the chain from its equilibrium position. Instead of writing the equations for these displacements – we wrote these equations in Chapter 2 – we write here the Lagrangian that describes these small vibrations. This Lagrangian is given by

$$L = \frac{1}{2}\dot{\boldsymbol{u}}^T \mathbf{M} \dot{\boldsymbol{u}} - \frac{1}{2}\boldsymbol{u}^T \mathbf{K} \boldsymbol{q}, \tag{3.1}$$

where we denote again with $\boldsymbol{u}$ the vector of displacements, i.e., $\boldsymbol{u} = \begin{pmatrix} u_1 & u_2 & \cdots & u_N \end{pmatrix}$. Also $\mathbf{M} = m\mathbf{I}_N$ is the mass matrix ($\mathbf{I}_N$ denotes the identity matrix of size N) and $\mathbf{K}$ is the stiffness matrix [1]

$$\mathbf{K} = \begin{pmatrix} \kappa_1+\kappa_2 & -\kappa_2 & 0 & & \dots \\ -\kappa_2 & \kappa_1+\kappa_2 & -\kappa_1 & 0 & \dots \\ 0 & -\kappa_1 & \kappa_1+\kappa_2 & -\kappa_2 & \dots \\ & & \dots & & \\ & & \dots & -\kappa_2 & \kappa_1+\kappa_2 & -\kappa_1 \\ & & \dots & 0 & -\kappa_1 & \kappa_1+\kappa_2 \end{pmatrix}. \tag{3.2}$$

Notice that the diagonal elements of the stiffness matrix are the same. Therefore, this stiffness matrix obeys the anticommutative relation

$$\{\mathbf{K} - (\kappa_1+\kappa_2)\mathbf{I}_N, \mathbf{\Sigma}_z\} = 0, \tag{3.3}$$

[1] We note at this point that in Chapter 2, instead of the stiffness matrix $\mathbf{K}$, we used the dynamical matrix $\mathbf{D} = \mathbf{K}/m$. However, there is no difference in the analysis to use either the stiffness matrix $\mathbf{K}$ or the dynamical matrix $\mathbf{D}$ since the masses m of the chain are the same. We find it more convenient to work with the stiffness matrix $\mathbf{K}$ in this Chapter and therefore we continue our analysis with the use of this matrix.

where $\mathbf{\Sigma}_z$ is the matrix

$$\mathbf{\Sigma}_z = \begin{pmatrix} 1 & 0 & 0 & 0 & \cdots & & \cdots & 0 \\ 0 & -1 & 0 & 0 & \cdots & & \cdots & 0 \\ \vdots & & & & \ddots & & & \vdots \\ & \cdots & & \cdots & 0 & 1 & 0 & 0 \\ 0 & \cdots & & \cdots & 0 & 0 & -1 & 0 \\ 0 & \cdots & & \cdots & 0 & 0 & 0 & 1 \end{pmatrix} . \tag{3.4}$$

Due to the anticimmutative relation in Eq. (3.3) the system is said to possesses chiral symmetry, which guarantees the existence of edge modes.

3.2.2 Eigenanalysis

To obtain the eigenfrequencies and the eigenmodes of the chain, we follow the same procedure with the one that we followed in Chapter 2. Namely, we substitute solutions of the form $\boldsymbol{u}(t) = \boldsymbol{u}e^{i\omega t}$ in the Euler-Lagrange equations of the Lagrangian that is given in Eq. (3.1) and we find that $\omega_n^2 \boldsymbol{u}_n = \mathbf{K}\boldsymbol{u}_n$, where ω_n are the eigenfrequencies and $\boldsymbol{u}_n$ are the eigenmodes of the chain, with $n = 1, 2, ..., N$.

In Fig. 3.2 we present an example. We use a chain that consists of $N = 21$ masses. We set the mass $m = 1$ in arbitrary units $\bar{m}$. We also keep the quantity $\kappa_1 + \kappa_2$ constant and equal to 4 in arbitrary units $\bar{\kappa}$ and we present the eigenfrequencies ω_n as a function of $\kappa_2 - \kappa_1$. Notice that for $\kappa_1 \neq \kappa_2$ we find one mode whose frequency lies in the band gap. This mode is the edge mode. Its eigenfrequency is found explicitly in semi-infinite chains using the transfer method approach and is equal to

$$\tilde{\omega} = \sqrt{\frac{\kappa_1 + \kappa_2}{m}}, \tag{3.5}$$

(hereafter, every variable or parameter with a tilde, corresponds to the edge mode ($n = (N+1)/2$)). This mode is localized at either one of the two edges of the chain and decays exponentially with

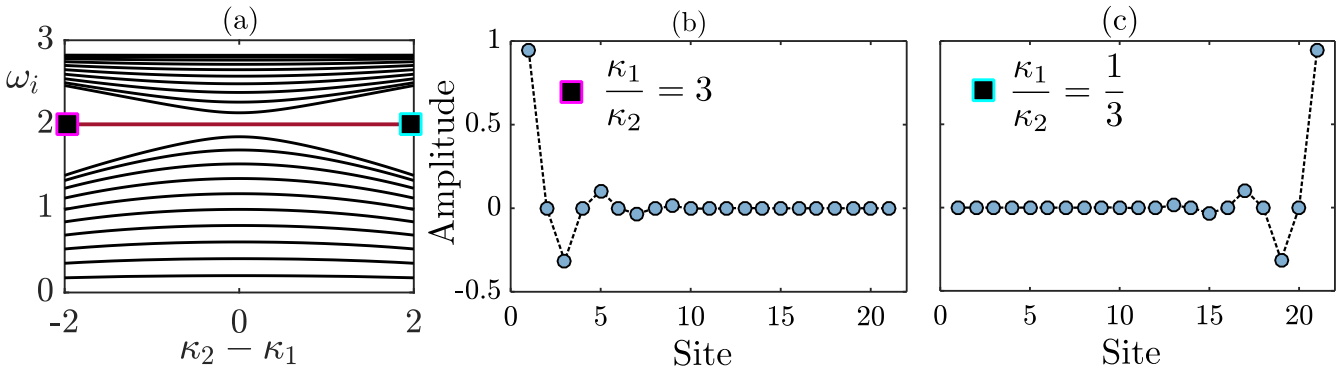

Figure 3.2: (a) Eigenfrequencies ω_i as a function of $\kappa_2 - \kappa_1$ keeping $\kappa_1 + \kappa_2 = 4$ of a chain with $N = 21$ masses. (b) When $\kappa_1 > \kappa_2$ the edge mode is localized at the left side of the chain while when (c) $\kappa_1 < \kappa_2$ it is localized at the right side.

increasing distance from the edge. Specifically, when $\kappa_1 > \kappa_2$ this mode is localized in the left side of the chain, while when $\kappa_1 < \kappa_2$ it is localized in the other side. In Fig. (b) and (c) we present the profile of the edge mode for (a) $\kappa_1 = 3\kappa_2$ and for (b) $\kappa_2 = 3\kappa_1$.

3.3 Basics for state transfer

Our goal is to transfer a localized mode from the one side of the chain to the other. Our initial mode will be a localized edge mode at the left side of the chain, as the one that we see in Fig. 3.2(b). Our target mode will be a right localized edge mode, as the one that we see in Fig. 3.2(c). To accomplish such a transfer we will let the spring stiffnesses to vary with time and to exchange values between the initial time $t = 0$ and a final time $t = T$

$$\kappa_1(0) = \kappa_2(T) \quad , \quad \kappa_2(0) = \kappa_1(T). \tag{3.6}$$

We aim to accomplish the transfer fast, namely to minimize the time T needed for the initial mode to reach the target one. In order to conclude whether the state transfer has been achieved we need a proper measure. We call this measure fidelity and we will define it via the energy flow in the chain.

3.3.1 Energy

From now on we assume that the couplings of the chain vary with time, meaning that the stiffness matrix is time-dependent $\mathbf{K} = \mathbf{K}(t)$. Therefore, the system is non conservative and the energy is not constant. The energy of the chain is given by the Hamiltonian, which in turn is given by a Legendre transformation of the Langrangian that is given in Eq. (3.1)

$$\mathcal{H}(\boldsymbol{q}, \boldsymbol{p}, t) = \frac{1}{2}\left(\boldsymbol{p}^T\boldsymbol{p} + \boldsymbol{u}^T\mathbf{K}(t)\boldsymbol{u}\right) \tag{3.7}$$

where $p_n \equiv \partial L/\partial \dot{u}_n$ is the n^{th} element of the conjugate momentum.

Notice that the stiffness matrix $\mathbf{K}(t)$ that is given in Eq. (3.7) is positive symmetric. Thus, it can be diagonalized by an orthogonal matrix which is composed by the instantaneous eigenvectors $\boldsymbol{q}_n(t)$ of $\mathbf{K}(t)$. We denote this orthogonal matrix as $\mathbf{A}(t)$. Therefore, it holds that $\mathbf{A}(t)^T\mathbf{K}(t)\mathbf{A}(t) = \boldsymbol{\Delta(t)}$ where $\boldsymbol{\Delta}(t) = \text{diag}\left(\omega_1^2(t), ..., \omega_N^2(t)\right)$ is the diagonal matrix with elements the eigenvalues of the stiffness matrix, i.e., the instantaneous eigenfrequencies squared.

With the use of the matrix $\mathbf{A}(t)$ we change variables now. We consider the transformation $(\boldsymbol{u}, \boldsymbol{p}) \to (\boldsymbol{Q}, \boldsymbol{P})$ with

$$\boldsymbol{Q} = \mathbf{A}(t)^T\boldsymbol{u}, \boldsymbol{P} = \mathbf{A}(t)^T\boldsymbol{p}. \tag{3.8}$$

The Hamiltonian that is given in Eq. (3.7) is written in these new variables as

$$\mathcal{H} = \frac{1}{2}(\boldsymbol{P}^T\boldsymbol{P} + \boldsymbol{Q}^T\boldsymbol{\Delta}(t)\boldsymbol{Q}). \tag{3.9}$$

Therefore, the total energy of the chain is written as the sum

$$E(t) = \sum_{n=1}^{N} E_n(t) = \sum_{n=1}^{N} \left(\frac{{P_n}^2}{2m} + \frac{1}{2}m\omega_n(t)^2 Q_n^2 \right). \tag{3.10}$$

where $E_i(t)$ is the instantaneous energy of each one of the N eigenmodes.

The variable change that is given in Eq. (3.8) is canonical and the generating function of this transformation is given by

$$F(\boldsymbol{p}, \boldsymbol{Q}, t) = -\boldsymbol{p}^T\mathbf{A}(t)\boldsymbol{Q}. \tag{3.11}$$

Therefore, the Hamiltonian $\mathcal{H}'(\boldsymbol{Q}, \boldsymbol{P}, t)$ that describes the system's dynamics in terms of the new variables $\boldsymbol{Q}$, $\boldsymbol{P}$ and the time t reads

$$\mathcal{H}'(\boldsymbol{Q}, \boldsymbol{P}, t) = \frac{1}{2}\left(\boldsymbol{P}^T\boldsymbol{P} + \boldsymbol{Q}^T\boldsymbol{\Delta}(t)\boldsymbol{Q}\right) - \boldsymbol{P}^T\mathbf{A}(t)^T\dot{\mathbf{A}}(t)\boldsymbol{Q}. \tag{3.12}$$

Notice that the first two terms of $\mathcal{H}'$ can be written as a sum of N independent Hamiltonians of harmonic oscillators. Excitations between different modes can take place due to the last term of $\mathcal{H}'$. This is because this term contains the matrix $\mathbf{A}(t)^T\dot{\mathbf{A}}(t)$ which is not diagonal. Yet, when the system's parameters change slowly in time - the process is adiabatic - then excitations between different modes do not take place since $\dot{\mathbf{A}}(t)$ is small.

Before closing this part, we note that the Hamiltonian $\mathcal{H}$ that is given in Eq. (3.9) describes the instantaneous total energy of the chain, while the Hamiltonian $\mathcal{H}'$ that is given in Eq. (3.12) governs the dynamics of the variables $\boldsymbol{Q}$ and $\boldsymbol{P}$.

3.3.2 Fidelity

We are ready to define a fidelity for the transferring process at this point. First, we introduce a quantity that measures how much of the total energy of the chain is distributed at the mode number n ($n = 1, 2, ..., N$) at time t. This measure is given by

$$C_n(t) = \frac{E_n(t)}{E(t)}. \tag{3.13}$$

namely it is the ratio of the instantaneous energy of the mode number n and of the total energy of the chain.

For the definition of the fidelity we will use the quantity $C_n(t)$ of the edge mode – corresponding

to index $n = \frac{N+1}{2}$ – at final time T, namely we will use the quantity

$$F = \tilde{C}(T) = \frac{\tilde{E}(T)}{E(T)}. \tag{3.14}$$

Notice that the quantity F measures how much of the final energy of the chain is stored in the target edge mode. If this quantity is one that means that all of the energy of the chain at time T is stored in the target edge mode and therefore the transfer is perfect. Yet, the quantity F does not take into account the initial mode.

The initial edge mode is an oscillating mode, with period of oscillation $\tilde{T} = 2\pi/\tilde{\omega}$. We may choose any initial phase ϕ_0 of this oscillation in order to determine the initial conditions, i.e., initial displacements and velocities. The quantity F depends on the initial phase ϕ_0 and therefore it is not a good measure for deciding if the initial edge mode has reached the target mode, since it could have a large value for some initial phase and a low value for some other ϕ_0. For this reason we consider the initial phase as a free parameter ranging from $[0, 2\pi)$ and we define as fidelity the following quantity

$$\text{Fidelity} = \mathcal{F} = \min_{\phi_0} F. \tag{3.15}$$

Using as fidelity the minimum of F over ϕ_0 we can be sure that the transfer has been achieved with a certain target fidelity regardless of the initial conditions.

3.3.3 Adiabatic invariant

If we let the couplings to vary slowly with time so that the transfer process is done adiabatically, then the initial edge mode reaches the target edge mode without exciting other modes (the bulk modes) at any time $t \in [0, T]$. However, if the transfer process is done beyond the adiabatic limit, then there will be excitations to instantaneous bulk modes, namely $E_n(t) \neq 0$ for $t > 0$ and $n \neq \frac{N+1}{2}$. In order to track the degree of adiabaticity of the process we use the adiabatic invariant of a system of N-coupled time-varying harmonic oscillators that is given by [131]

$$I(t) = \sum_n \frac{E_n(t)}{\omega_n(t)}. \tag{3.16}$$

In the general case, $I(t)$ oscillates and is not exactly invariant. In order for $I(t)$ to be considered an adiabatic invariant (and thus the process adiabatic), it must vary more slowly than the parameters vary (in our case κ_1 and κ_2).

3.4 Transfer protocols

Our goal in this part, is to find control schemes for the two couplings $\kappa_1(t)$ and $\kappa_2(t)$ that result in a fast transfer (minimize the total time T) of the edge mode across the chain. First of all, when the total time T is finite, then nonadiabatic excitations will appear in our system and it is not possible to have perfect transfer, namely fidelity $\mathcal{F} = 1$. Therefore, we have to set an acceptable lower bound for $\mathcal{F}$ that ensures almost perfect state transfer [132]. We choose $\mathcal{F}_{\text{target}} = 99\%$ and we consider that the transfer is successful when $\mathcal{F} > \mathcal{F}_{\text{target}}$. In Appendix C we show, using the WKB method [118], that if the two couplings $\kappa_{1,2}(t)$ change slowly with time so that the transfer is done adiabatically, then the initial mode is transferred to the target mode with fidelity 1.

For all the cases that we consider in the following, we use a chain that consists of $N = 21$ masses and we set the initial/final stiffness values at $\kappa_1(0) = \kappa_2(T) = 3$ and $\kappa_2(0) = \kappa_1(T) = 1$ in arbitrary units of κ_0, which without loss of generality we set at $\kappa_0 = 1$. We also set the values of the masses at $m = 1$ in arbitrary units $\bar{m}$.

3.4.1 Constrained protocols

We begin our analysis by studying control schemes which can all be written in the form

$$\kappa_1(t) = \kappa^+ + \kappa^- f(t) \quad , \quad \kappa_2(t) = \kappa^+ - \kappa^- f(t), \tag{3.17}$$

where $\kappa^+ = \frac{\kappa_1(0)+\kappa_2(0)}{2}$ and $\kappa^- = \frac{\kappa_1(0)-\kappa_2(0)}{2}$. Notice that these protocols keep the eigenfrequency of the edge mode constant during the whole time of the process since for every t, $\overline{\kappa}(t) = \kappa_1(t) + \kappa_2(t)$ is constant and equal to $\kappa_1(0) + \kappa_2(0)$ $\Big($recall that $\tilde{\omega}(t) = \sqrt{\kappa_1(t) + \kappa_2(t)}\Big)$.

Trigonometric protocol

As a first step, we consider that the function $f(t)$ is the trigonometric function,

$$f(t) = \cos\left(\frac{\pi t}{T}\right). \tag{3.18}$$

This control scheme is shown in Fig. 3.3(a). In Fig. 3.3(b) we present the corresponding fidelity $\mathcal{F}$ of this scheme as a function of the final time of the process T. Clearly, $\mathcal{F}$ increases smoothly with T and approaches unity as $T \to \infty$, while it reaches the target fidelity at $T_{\text{trig}} = 297$. Furthermore, in Fig. 3.3(c) we present the instantaneous eigenfrequencies ω_n as a function of the time. Notice that the frequency of the edge mode (indicated with the red line) is constant at all times.

The time $T_{\text{trig}} = 297$ that is required so that the transfer is successful is almost two orders of magnitude longer than the period of oscillation of the initial (and target) edge mode $\Big(T_{\text{trig}} \gg \tilde{T} = \frac{2\pi}{\tilde{\omega}} = \pi\Big)$. This implies that the protocol is nearly adiabatic. To justify this further

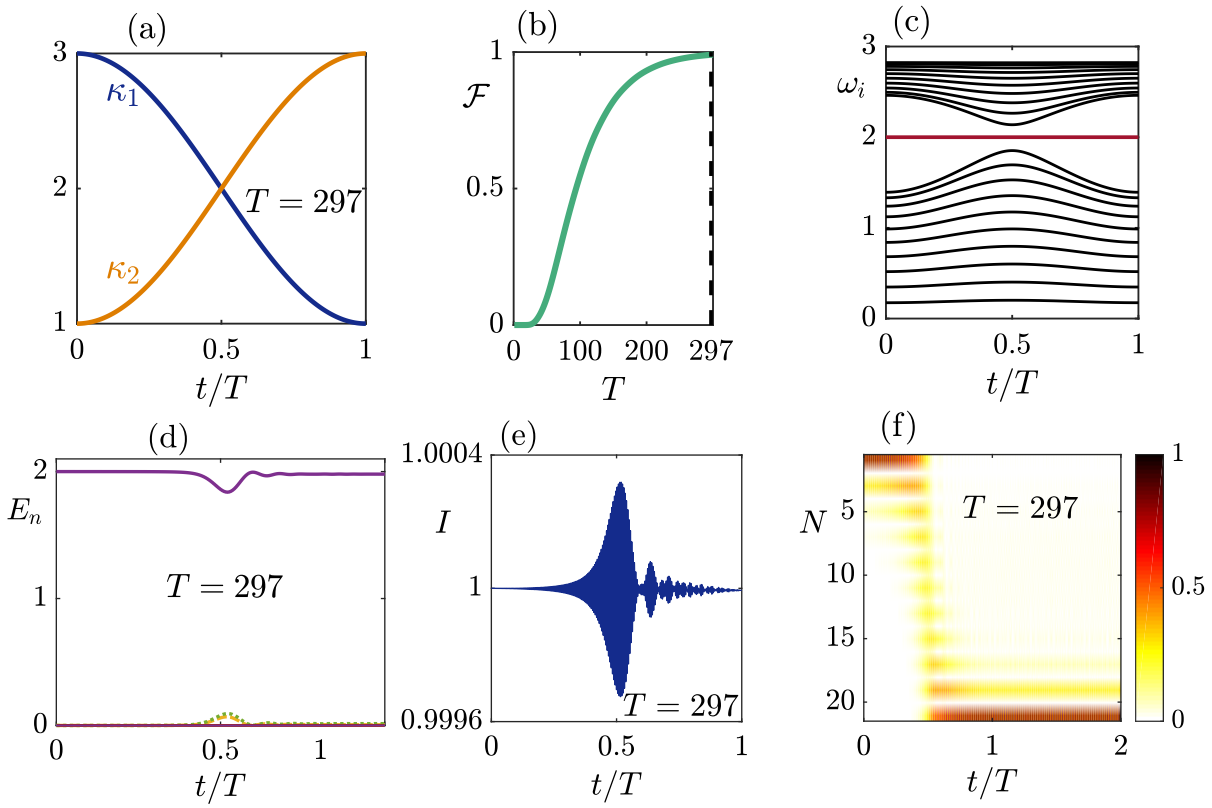

Figure 3.3: (a) $\kappa_1(t)$ and $\kappa_2(t)$ for the trigonometric protocol. (b) $\mathcal{F}(T)$ for this scheme. (c) Eigenfrequencies ω_i. (d) Instantaneous energy of each mode $E_i(t)$ (e) Adiabatic invariant $I(t)$. (f) Time evolution of the absolute value of the particle displacements. In panels (d)-(f) we set the initial phase ϕ_0 at zero.

we present in Fig. 3.3(d) the instantaneous energies $E_n(t)$ of all of the N modes and in Fig. 3.3(e) the adiabatic invariant $I(t)$. In both cases we set the initial phase at zero, $\phi_0 = 0$, meaning that initially all the masses have zero velocities and maximum displacements from their equilibrium positions. From Fig. 3.3(d) we observe very limited excitations to bulk modes (the purple shows the instantaneous energy of the edge mode). From Fig. 3.3(e) we get that the adiabatic invariant shows small oscillations and vanishing deviation from the initial value $I(0) = 1$. Finally, in Fig. 3.3(f) we show the spatio-temporal evolution of the absolute value of the mass displacements. Again we set the initial phase at zero. With the evolution at a final time $2T$, with $\kappa_{1,2}(T \leq t \leq 2T) = \kappa_{1,2}(T)$, we verify that the edge mode remains localized at the other side of the chain, after reaching the target mode at time T_{trig}.

Linear protocol

We now modify the way that the couplings change in time. We consider that the function $f(t)$ varies linearly with time,

$$f(t) = 1 - 2\frac{t}{T}. \tag{3.19}$$

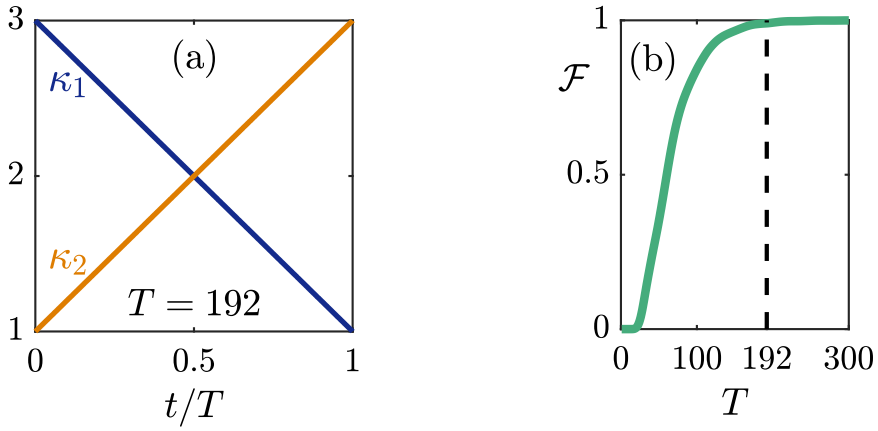

Figure 3.4: (a) $\kappa_1(t)$ and $\kappa_2(t)$ for the linear protocol. (b) $\mathcal{F}(T)$ for this scheme.

We present this control scheme in Fig. 3.4(a). In Fig. 3.4(b) we illustrate the corresponding fidelity. This protocol has smoothly increasing fidelity with T and reaches $\mathcal{F} > 99\%$ for total time $T_{\text{linear}} = 192$.

Notice that the linear function approaches to and departs from the closed gap point, namely at the point where $\kappa_1 = \kappa_2$, at the same rate. On the contrary, the trigonometric function is slower in the beginning (and in the end) when the gap is very open and fast when it approaches the closed gap point. The higher speed of the linear protocol, compared to the trigonometric one, could mean that protocols that reach the closed gap point faster may reach the desired fidelity at a shorter time. We continue our study along this line and in the following we study a control scheme that approaches the closed gap point faster than the linear protocol.

Tangential protocol

We consider that the control function $f(t)$ is given by

$$f(t) = \frac{\tan(\pi t/T_f + \alpha)}{\tan \alpha} \tag{3.20}$$

where $T_f = \frac{\pi T}{2\pi - 2\alpha}$ and $\alpha \in (\pi/2, \pi)$ is a free parameter. We search for the value of α that results in a fidelity $\mathcal{F}$ that reaches its target value (99%) at the shortest possible final time T. We find that the desired value of α is $\pi/2 + 0.4$.[2] We present this control scheme for this value of α in Fig. 3.5(a). Furthermore, we get that for $\alpha = \pi/2 + 0.4$, the fidelity reaches its target value at time $T_{\text{tan}} = 89$. The corresponding fidelity of this scheme as a function of the final time T is illustrated in Fig. 3.5(b).

In Fig. 3.5(c) we present the instantaneous energies $E_n(t)$ of the modes, for $\phi_0 = 0$. From this

[2]For the derivation of this value of α we use the CRAB optimal control method that we mention at the beginning of this chapter.

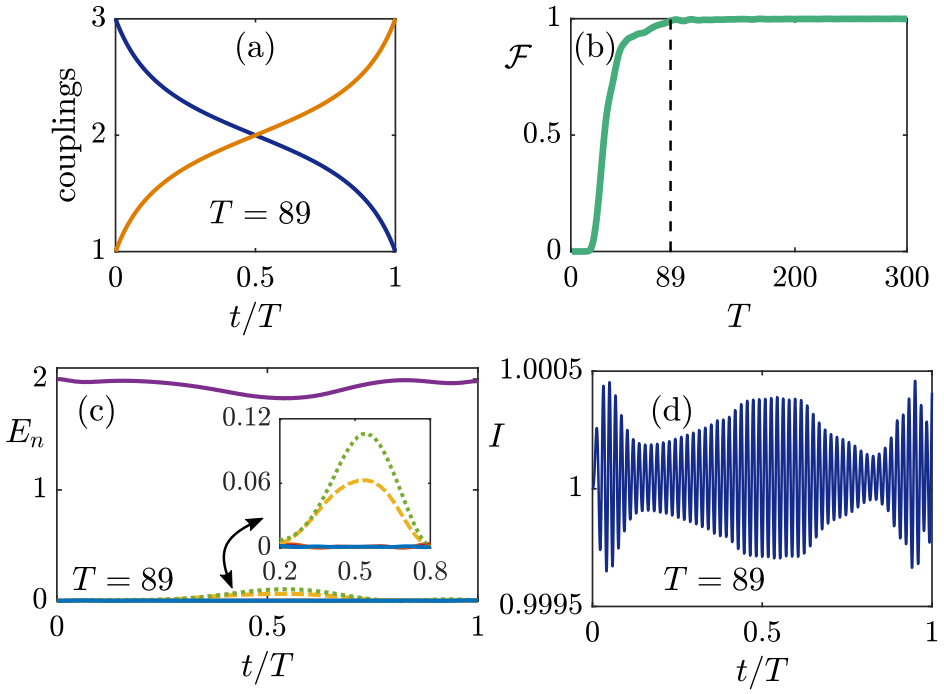

Figure 3.5: (a) $\kappa_1(t)$ and $\kappa_2(t)$ for the optimal tangential protocol. (b) $\mathcal{F}(T)$ for this scheme. (c) Instantaneous energy of each mode, $E_i(t)$ (d) Adiabatic invariant $I(t)$.

figure we get that this optimal tangential protocol has a bit higher bulk mode excitations than the trigonometric one. Moreover, the adiabatic invariant of this scheme (see Fig. 3.5(d)) - it is calculated again for $\phi_0 = 0$ - shows also a bit higher oscillations that the trigonometric protocol. Therefore, we conclude that this optimal tangential protocol is a less adiabatic protocol than the trigonometric one.

Up to now, we have studied three protocols and our conclusion is that the protocol that approaches the closed gap point faster (the optimal tangential), is the one that speeds up the energy transfer. This observation drives us to study an extreme case. We study the control scheme that is illustrated in Fig. 3.6(a), where the function $f(t)$ is almost a step function. This function $f(t)$ is given from Eq. (3.20) by setting $\alpha = \pi/2 + 0.001$. In Fig. 3.6(b) we present the corresponding fidelity of this control scheme. Clearly, this fidelity does not reach high values and oscillates strongly. Furthermore, in Fig. 3.6(c) we present the spatio-temporal evolution at the final time T = 89, i.e., at the final time that the previous control scheme reaches the target fidelity. Clearly, the initial edge mode does not reach the target one.

The step protocol does not improve the transfer due to the following reason: Even though this protocol approaches directly the closed gap point, it stays longer at its vicinity where the probability of nonadiabatic excitations becomes higher. However, the probability of nonadiabatic excitations becomes higher at the vicinity of the closed gap point. These observations indicate the following: there is no trivial simple process that can reach high fidelity at vanishing time. On

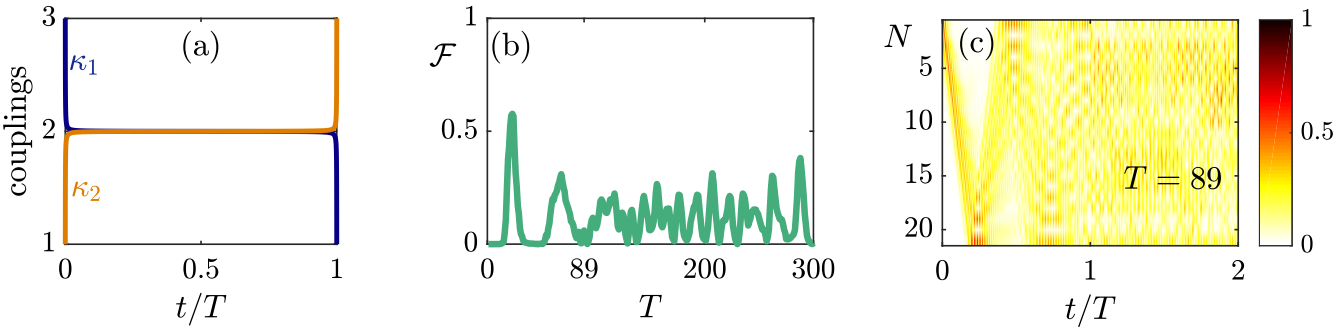

Figure 3.6: (a) $\kappa_1(t)$ and $\kappa_2(t)$ for the step protocol. (b) $\mathcal{F}(T)$ for this scheme. (c) Time evolution of the absolute value of the particle displacements.

the opposite, as we deviate from adiabaticity the handling of the energy flow is very subtle. This requires to search for optimal solutions.

3.4.2 Non-constrained protocols

All the protocols that we have studied so far, keep the frequency of the edge mode constant during the whole time of the process. In this part, we raise this constraint in order to get more transfer speed (if it is possible). We also use the CRAB optimal control method [128, 129].

3-step protocol

The first control scheme that we study and that does not keep the frequency of the edge mode constant during the transfer process, is illustrated in Fig. 3.7(a). We call this protocol as *3-step protocol* since it consists of 3 time intervals. In the first time interval (we denote its length as Δt_1) the stiffness of the coupling κ_1 is constant and equal to its initial value, while the stiffness of the coupling κ_2 increases linearly up to the value of $\kappa_1(0)$. In the second time interval Δt_2, both coupling stiffnesses are constant at their maximum value $\kappa_1(0)$. Finally, in the third time interval Δt_3 the stiffness of the coupling κ_1 drops to the value of $\kappa_2(0)$, while the stiffness of the coupling κ_2 remains constant and equal to $\kappa_1(0)$.

If we impose the mirror condition $\kappa_2(t) = \kappa_1(T - t)$, then there is only one free parameter. This free parameter is the length of the first/third time interval. We search for the optimal value of this time interval, i.e., the value of $\Delta t_1 (= \Delta t_3)$ for which the fidelity reaches the target value 99% at the minimum final time T. We find that the fidelity reaches the value $\mathcal{F} > 99\%$ at time $T_{\text{3-step}} = 39$ when the first/third time intervals have length $\Delta t_1 = \Delta t_3 = 0.4 T_{\text{3-step}}$. We present the fidelity as a function of the final time T in Fig. 3.7(b). Opposite to the previous protocols, the fidelity is fluctuating in this case (in all the protocols that we have studied so far – apart from the step protocol – the fidelity is close to 1 for final times T larger than 300).

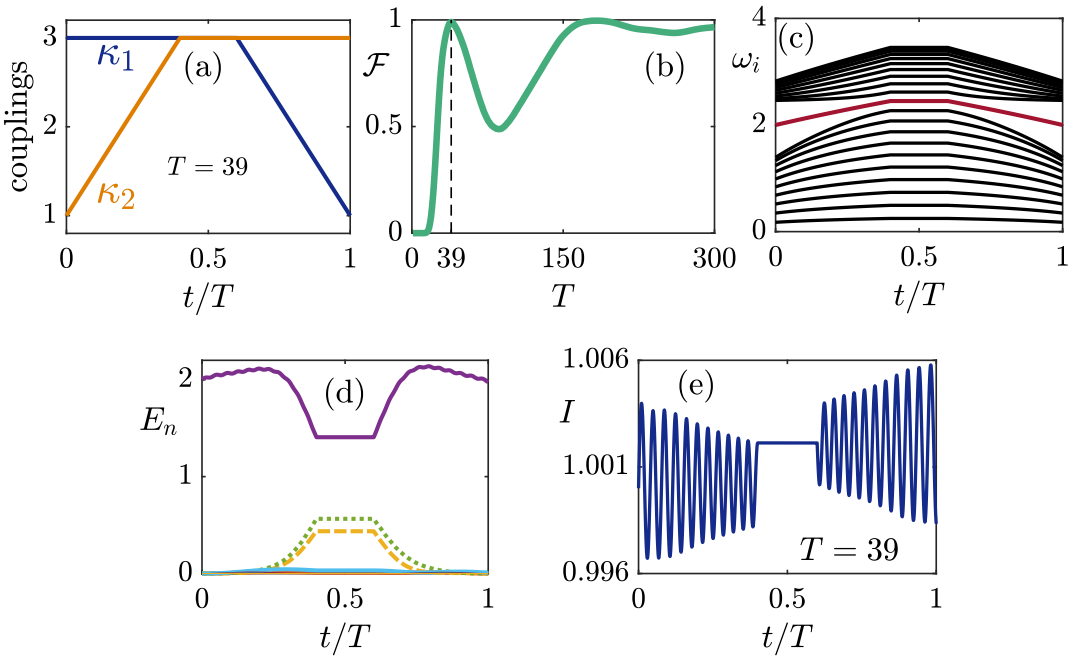

Figure 3.7: (a)-(e): Same as Fig. 3.3 but for the 3-step protocol.

In Fig. 3.7(c) we present the instantaneous eigenfrequencies ω_n as a function of the time t. Notice that the instantaneous frequency of the edge mode $\tilde{\omega}(t)$ is shifted up and down and its mean value $\tilde{\omega}_{\text{mean}}$ is higher than its initial/final value. Therefore, the time scales which may be considered inverse proportional to $\tilde{\omega}_{\text{mean}}$ effectively decrease and this is why the transfer gets faster in this case.

In Fig. 3.7(d) we show the instantaneous energies E_n of the modes. Clearly, these increase and decrease substantially during the time intervals Δt_1 and Δt_2. Finally, in Fig. 3.7(e) we present adiabatic invariant $I(t)$. Notice that it shows rather larger oscillations, compared to previous protocols, during the time intervals Δt_1 and Δt_2.

We close our analysis for the 3-*step protocol* with the following comment: We lifted the mirror symmetry condition $\kappa_2(t) = \kappa_1(T - t)$ and we searched again for the optimal values of the free parameters (the free parameters are two in this case). The optimization procedure returned values for these parameters that render back the mirror symmetry. Namely, the parameters and the results were the same with the ones that we got when we imposed the mirror symmetry.

3-step up protocol

The 3-step up protocol revealed that if we take the value of $\tilde{\omega}_{\text{mean}}$ to be larger than $\tilde{\omega}(0) = \tilde{\omega}(T)$, then the state transfer is becoming faster. A natural step towards this direction is to increase further the value of $\tilde{\omega}_{\text{mean}}$. This is accomplished with the protocol that we study here and which is illustrated in Fig. 3.8(a). We call this protocol as 3-*step up* for evident reasons: It is similar with

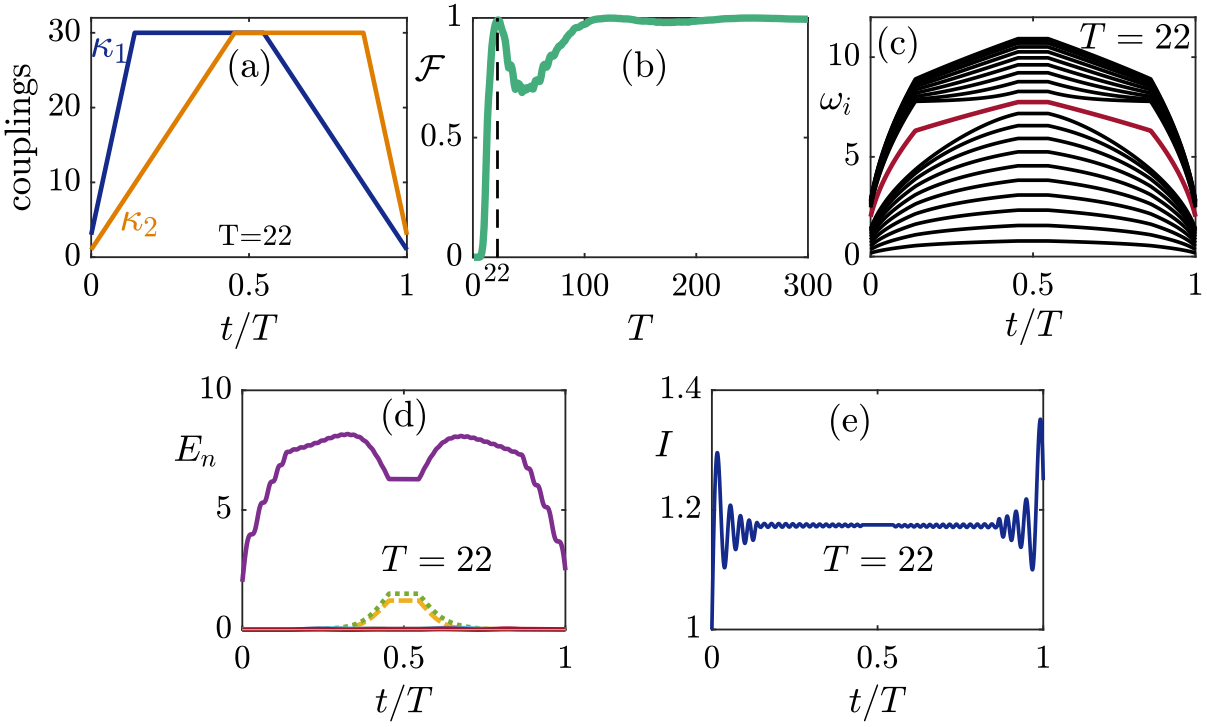

Figure 3.8: (a)-(e): Same as Fig. 3.3 but for the 3-step up protocol.

the 3-*step* protocol with the difference that in the time interval Δt_2 the values of the stiffnesses are equal to $\kappa_{\max} = 30$.[3]

In this case, we do not impose the mirror symmetry $\kappa_2(t) = \kappa_1(T-t)$ from the beginning. Therefore, we have 4 free parameters. Two time intervals for the coupling κ_1 (for example the Δt_1 and the Δt_3) and two time intervals for the coupling κ_2. The optimization procedure returned the following optimal values: The coupling κ_1 is constant (and equal to $\kappa_{\max} = 30$) at the time interval $[0.138T, 0.546T]$ and the coupling κ_2 is constant and equal to $\kappa_{\max} = 30$ at the time interval $[0.454T, 0.862]$. From these values we get that the optimization procedure rendered back again the mirror symmetry $\kappa_2(t) = \kappa_1(T-t)$ (this is also evident from Fig. 3.8(a)). For these optimal values, the fidelity reaches the target value 99% at time $T_{\text{3-step up}} = 22$ which is another significant reduction compared to the 3-step protocol. We present the fidelity as a function of the final time in Fig. 3.8(b).

This gain in the transfer speed is explained from the evolution of the eigenfrequencies ω_n. These are illustrated in Fig. 3.8(c). The eigenfrequencies change substantially here and clearly the mean value of $\tilde{\omega}(t)$ is much larger, compared to the 3-step protocol. Finally, in Fig. 3.8(d) and (e) we present the instantaneous energies E_n and the adiabatic invariant $I(t)$ as a function of the time t. These two panels suggest that this protocol is the most non-adiabatic compared to all others we have examined so far.

[3]Notice that in the 3-*step* protocol the corresponding maximum value of the stiffnesses was $\kappa_{\max} = 3$.

3-step & 3-step up cubic protocols

We can gain more transfer speed by considering control schemes that include more parameters. For instance, the couplings κ_1 and κ_2 in the 3-step and in the 3-step up protocols are linear functions and have different linear forms in three time intervals. We build the cubic analogues of these protocols, which we call 3-*step cubic* and 3-*step up cubic* protocols. In this protocols, the couplings κ_1 and κ_2 are cubic polynomials and have different forms in three time intervals. Moreover, the difference between the 3-*step cubic* and the 3-*step up cubic* is that in the former case the values of $\kappa_1(t)$ and $\kappa_2(t)$ cannot exceed the value $\kappa_1(0) = \kappa_2(T)$.

The coefficients of these polynomials and the time intervals are found again with an optimization procedure. The results are illustrated in Fig. 3.9. Notice that the 3-step cubic protocol reaches the fidelity $\mathcal{F} > 99\%$ at total time $T_{\text{3-step cubic}} = 35$ (recall that $T_{\text{3-step}} = 39$). The 3-step cubic up protocol reaches the target fidelity at total time $T_{\text{3-step cubic up}} = 12$ (recall that $T_{\text{3-step up}} = 22$).

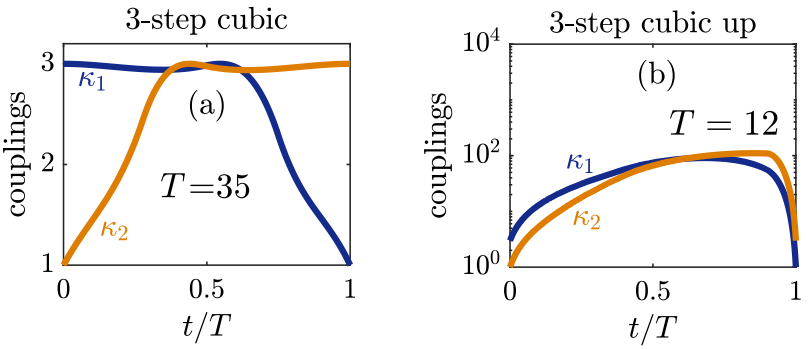

Figure 3.9: (a) $\kappa_{1,2}(t)$ for the 3-step cubic protocol. (b) Corresponding $\kappa_{1,2}(t)$ for the 3-step up cubic protocol.

3.4.3 Disorder analysis

In this part, we apply disorder at some of the protocols that we studied before. The protocols that we will examine in the presence of disorder are: the trigonometric, the tangential, the 3-step, and the 3-step up protocols. We consider a form of disorder that affects only the initial stiffness values

$$\kappa_n(0) \to \kappa_n(0)\,(1 + \eta w_n) \quad , \quad n = 1, ..., N+1 \tag{3.21}$$

with $\eta = 0.2$ and $w_n \in [-1, 1]$ a random number that is uniformly distributed.

We set the initial phase at $\phi_0 = 0$ and we calculate the quantity $F(\phi_0 = 0)$ for each disorder realization. Also, for each protocol we evolve the system at the corresponding final times that the fidelity reaches its target value, namely at $T = 297$ for the trigonometric protocol, at $T = 89$ for the tangential protocol, at $T = 39$ for the 3-step protocol and at $T = 22$ for the 3-step up protocol. In Fig. 3.10 we present the statistical distribution of $F(\phi_0) = 0$ out of 10^5 disorder realizations.

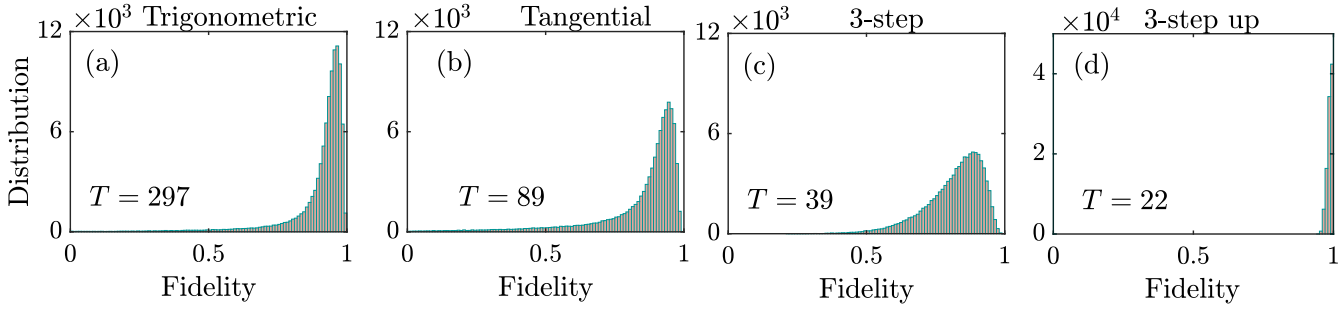

Figure 3.10: Shown is the statistical distribution of $F(\phi_0 = 0)$ out of 10^5 realizations of disorder for the (a) Trigonometric (b) Tangential (c) 3-step and (d) 3-step up protocol.

Clearly, the trigonometric protocol is more robust than the tangential and the 3-step protocol. But the 3-step up is even more robust than the trigonometric. This is attributed to the fact that the edge mode remains well separated from the bulk modes throughout the process.

To shed more light, we present in Fig. 3.11(a) and (b) the instantaneous eigenfrequencies of the tangential protocol for two different disorder realizations. In Fig. 3.11(a) the fidelity remains high after the application of disorder while in Fig. 3.11(b) the fidelity drops with the application of disorder. Similarly, in Fig. 3.11(c) and (d) we present the instantaneous eigenfrequencies of the 3-step protocol when the fidelity remains high with the application of disorder (panel (c))

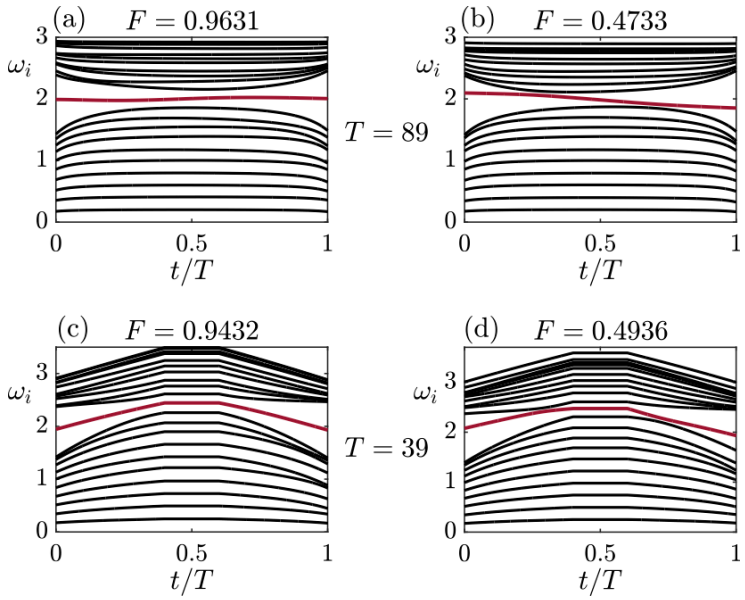

Figure 3.11: Instantaneous eigenfrequencies ω_i as a function of time t after the application of disorder for (a) the tangential protocol and when the fidelity remains high (b) the tangential protocol and when the fidelity drops (c) the 3-step protocol and when the fidelity remains high (d) 3-step protocol and when the fidelity drops.

and when the fidelity drops with the application of disorder (panel (d)). Notice that the fidelity remains high after the application of disorder, when the band gap is sufficiently open and the eigenfrequency of the edge mode is separated from the bands. On the contrary, the fidelity drops with the application of disorder, when the frequency of the edge mode approaches the two bands, since the bulk modes are strongly excited in this case.

3.5 Energy amplification

As we noted before, when the couplings of the chain change with time, the system is non-conservative. Meaning that the energy that is stored in the chain after time T could be higher/lower than the energy that is initially stored. Similarly, the final energy of the final edge mode (right localized) can exceed the energy of the initial edge mode (left localized).[4] Therefore, we define a quantity that measures this energy amplification of the edge mode. It is given by

$$A = \frac{\tilde{E}(T)}{\tilde{E}(0)} = \frac{\tilde{E}(T)}{E(0)} \ . \tag{3.22}$$

In Fig. 3.12 we show the quantity A as a function of the initial phase ϕ_0 for the 3-step up protocol (the final time is $T = 22$ - the fidelity is above 99%). Notice that $A > 1$ for various values of ϕ_0 and therefore the initial edge mode is transferred across the chain and is simultaneously amplified. Moreover, A could be less than 1 for certain other values of ϕ_0, meaning that the transferred mode is disamplified. As a final remark, we note here that when the transfer is done adiabatically (which is not the case for the 3-step up protocol), then the initial mode is transferred to the target one without being amplified. We prove this in Appendic C, using the WKB method.

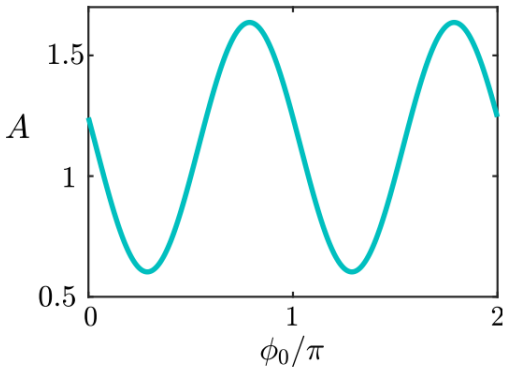

Figure 3.12: (a) Amplification A as a function of the initial phase ϕ_0 for the 3-step up protocol.

[4]Notice that the energy that is given at the start of the process to the initial edge mode is also the total energy that is given to the system initially, since no other modes are excited at $t = 0$. Therefore, $\tilde{E}(0) = E(0)$.

3.6 Concluding remarks

We have shown in this Chapter how to achieve a fast and robust transfer in a mechanical chain. Due to the absence of unitarity in the classical system that we studied, the transferred mode can be either amplified or disamplified, according to the initial's edge mode phase of oscillation ϕ_0. As a closing remark, we note that the phase ϕ_0 is not the only parameter that results in amplification/disamplification. For instance, in Fig. 3.13 is shown the quantity A as a function of κ_{max} for the 3-step up protocol (we set $\phi_0 = 0$). Notice that we can get $A > 1$ (amplification) or $A < 1$ (disamplification) with an appropriate choice of the bound $\kappa_{\max}$.

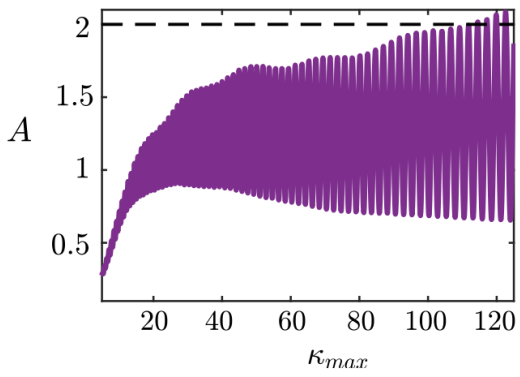

Figure 3.13: Amplification A as a function of κ_{max} for the 3-step up protocol.

Chapter 4

Transient amplification for the Mathieu equation without parametric instability

4.1 Introduction

In Chapter 3, we encountered the phenomenon of amplification in a time-varying platform. We are interested to investigate this phenomenon further. To achieve this, we will employ the well known Mathieu equation [1, 115] since it occurs naturally when we consider wave propagation in an infinite medium that is periodically modulated in time [116, 117].

The Mathieu equation is among the well studied equations in physics [1, 109, 115, 118, 133–135] and it is known to lead to parametric instability in some regions of its parameter space. However, it has been reported that even the stable solutions of the Mathieu equation can be transiently amplified [136].

In this Chapter, we explore the transient effects and the global maximum amplification of the stable solutions of the Mathieu equation. To do so we use several quantities of the ϵ-psudospectrum [110] of the monodromy matrix – the matrix that propagates the initial conditions over one period – and we demonstrate that is the degree of non-normality of this matrix [112] that determines the global amplifying features.

4.2 Wave propagation in Floquet media

To start this part, we follow ref. [116, 117] and we consider the wave propagation in a one dimensional infinite medium that is governed by the following wave equation

$$\frac{\partial^2\psi(x,t)}{\partial t^2} = \left[\tilde{\delta} - 2\tilde{q}\cos(\Omega t)\right]\frac{\partial^2\psi(x,t)}{\partial x^2} \tag{4.1}$$

where $\tilde{\delta}$, $\tilde{q}$ and Ω are constants. In order to solve Eq. (4.1) we apply the method of separation of variables. That is, we assume that the solution $\psi(x,t)$ is written in the form $\psi(x,t) = f(t)h(x)$ and by substituting this form into Eq. (4.1) we arrive at the following set of ODE's for $f(t)$ and $h(x)$

$$\frac{d^2h(x)}{dx^2} + k^2h(x) = 0 \tag{4.2}$$

$$\frac{d^2f(t)}{dt^2} + k^2\left[\tilde{\delta} - 2\tilde{q}\cos(\Omega t)\right]f(t) = 0 \tag{4.3}$$

where k is the real wave number of the wave. From Eq. (4.2) we get that $h(x)$ has the form $h(x) \sim e^{\pm ikx}$. To get an insight into the function $f(t)$, first we rescale the time as $\tau = \Omega t/2$ and then we set $\delta = 4k^2\tilde{\delta}/\Omega^2$, $q = 4k^2\tilde{q}/\Omega^2$ (we should keep in mind that the parameters δ and q are related with the wave number k). After this, Eq. (4.3) drops to the usual form of the Mathieu equation, that is

$$\ddot{f} + [\delta - 2q\cos(2\tau)]\,f = 0 \tag{4.4}$$

where dot represents differentiation with respect to the time τ.

4.2.1 Unstable and stable solutions of the Mathieu equation

The Mathieu equation contains both stable and unstable solutions according to the values of the parameters δ and q. For an illustration, we present in Fig. 4.1 the evolution of the function $f(\tau)$ for two different sets of parameters (δ, q). We indicate the set of (δ, q) that is used in Fig. 4.1(a) with an orange rectangle and the corresponding set of (δ, q) that is used in Fig. 4.1(b) with a green rectangle. Also, in both cases, we used as initial conditions: $f(0) = 0$ and $\dot{f}(0) = 1$.

Clearly, the set of (δ, q) that is used in Fig. 4.1(a) leads to an unstable solution $f(\tau)$ and in particular $f(\tau)$ grows exponentially with time. On the contrary, in Fig. 4.1(b) we used a set of parameters (δ, q) that leads to a stable $f(\tau)$: the solution $f(\tau)$ is oscillating in time and is transiently amplified.

In the next part, we are interested in understanding and quantifying the transient amplification that stable solutions can exhibit. For that, we will show first the regions in the (δ, q) plane that correspond to the stable solutions of Eq. (4.4), essentially, the stable regions of the stability chart of the Mathieu equation.

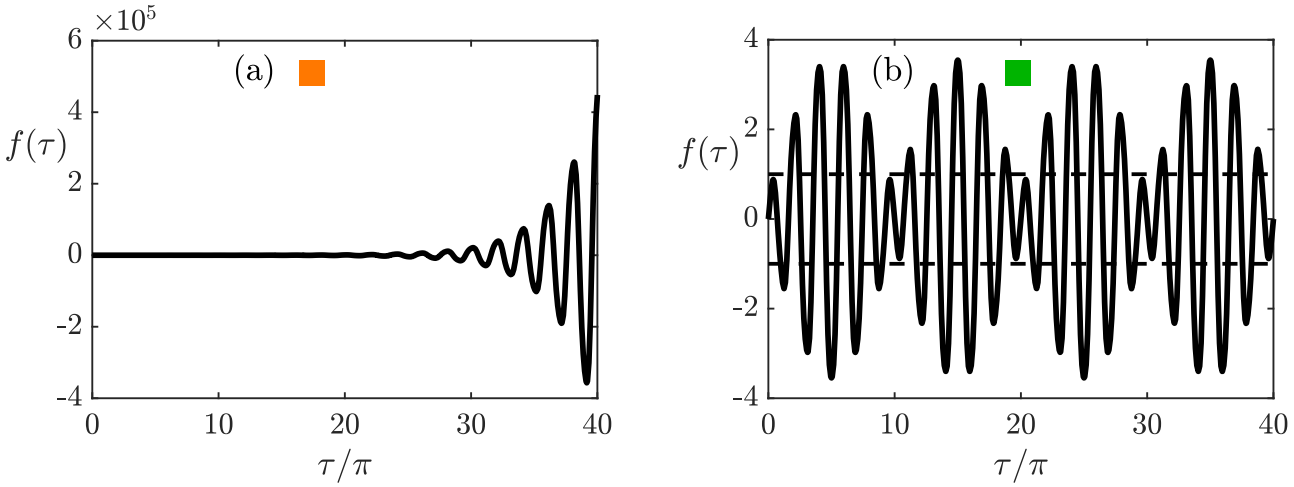

Figure 4.1: Evolution of the function $f(\tau)$ that is a solution of the Mathieu equation for the initial conditions $f(0) = 0$ and $\dot{f}(0) = 1$ and for the set of parameters (a) $q = 0.4578$, $\delta = 3q$ and (b) $q = 0.5072$, $\delta = 3q$.

4.2.2 Review of Mathieu equation

We write first the Mathieu equation as a system of two linear differential equations

$$\dot{\boldsymbol{\eta}}(\tau) = \mathbf{A}(\tau)\boldsymbol{\eta}(\tau), \tag{4.5}$$

with $\boldsymbol{\eta}(\tau) = \begin{pmatrix} f(\tau) \\ \dot{f}(\tau) \end{pmatrix}$ and $\mathbf{A}(\tau) = \begin{pmatrix} 0 & 1 \\ -(\delta - 2q\cos(2\tau)) & 0 \end{pmatrix}$. The general solution of Eq. (4.5) is written in the form

$$\boldsymbol{\eta}(t) = \boldsymbol{\Psi}(\tau, \tau_0)\boldsymbol{\eta}(\tau_0), \tag{4.6}$$

where the vector $\boldsymbol{\eta}(\tau_0)$ contains the initial conditions $f(\tau_0)$ and $\dot{f}(\tau_0)$ and the matrix $\boldsymbol{\Psi}(\tau, \tau_0)$ is called principal matrix solution and it solves the matrix valued problem $\frac{d\boldsymbol{\Psi}(\tau,\tau_0)}{d\tau} = \mathbf{A}(\tau)\boldsymbol{\Psi}(\tau, \tau_0)$ with $\boldsymbol{\Psi}(\tau_0, \tau_0) = \mathbf{I}$ (see for example ref. [109]). In order to calculate the elements of the principal matrix solution for any set of times τ and τ_0, we have to evolve the initial conditions $\boldsymbol{\eta}_1(\tau_0) = \begin{pmatrix} f_1(\tau_0) \\ \dot{f}_1(\tau_0) \end{pmatrix} = \begin{pmatrix} 1 \\ 0 \end{pmatrix}$ and $\boldsymbol{\eta}_2(\tau_0) = \begin{pmatrix} f_2(\tau_0) \\ \dot{f}_2(\tau_0) \end{pmatrix} = \begin{pmatrix} 0 \\ 1 \end{pmatrix}$ forward in time. The principal matrix solution is then given by $\boldsymbol{\Psi}(\tau, \tau_0) = \begin{pmatrix} f_1(\tau) & f_2(\tau) \\ \dot{f}_1(\tau) & \dot{f}_2(\tau) \end{pmatrix}$. For the case of the Mathieu equation, we calculate $f_1(\tau)$, $\dot{f}_1(\tau)$ and $f_2(\tau)$, $\dot{f}_2(\tau)$ by solving Eq. (4.4) numerically, since there is no analytical solution. The analysis for the derivation of the principal matrix solution that we discuss here applies to any system of nonautonomous linear ordinary differential equations that is written in the form $\dot{\boldsymbol{\eta}}(\tau) = \mathbf{A}(\tau)\boldsymbol{\eta}(\tau)$. However, when the matrix $\mathbf{A}(\tau)$ is a periodic one, then we can apply the Floquet theory and derive the stability of the solutions as we show next.

Notice that for the Mathieu equation the matrix $\mathbf{A}(\tau)$ is π-periodic, i.e., $\mathbf{A}(\tau+\pi)=\mathbf{A}(\tau)$. The Floquet theory states that the stability of the solutions is derived by the eigenvalues of the principal matrix that is evaluated over one period, namely by the eigenvalues of the matrix $\mathbf{\Psi}(\tau_0+\pi,\tau_0)$. The matrix $\mathbf{\Psi}(\tau_0+\pi,\tau_0)$ is called the monodromy matrix. The eigenvalues of the monodromy matrix are commonly known as Floquet multipliers. We denote the Floquet multipliers as $\lambda_\pm$. From Liouville's formula $\det\left[\mathbf{\Psi}(\tau_0+\pi,\tau_0)\right]=\exp\left[\int_{\tau_0}^{\tau_0+\pi}\mathrm{Tr}\left(\mathbf{A}(s)\right)ds\right]$ [109] we get that the determinant of the monodromy matrix is 1 and therefore the Floquet multipliers satisfy the relation $\lambda_+\lambda_-=1$. When $|\lambda_\pm|=1$, then the Floquet multipliers are restricted to lie in the unit circle in the complex plane and are complex conjugates. In that case the solutions of the Mathieu equation are stable. When $|\lambda_\pm|\neq 1$ then the Floquet multipliers lie in the real axis in the complex plane and in that case the solutions of the Mathieu equation are unstable and grow exponentially with time. We note here that the Floquet multipliers do not depend on the initial time τ_0. This is because the matrices $\mathbf{\Psi}(\pi+\tau_1,\tau_1)$ and $\mathbf{\Psi}(\pi+\tau_2,\tau_2)$ are similar and therefore they share the same eigenvalues [109].

In Fig. 4.2 we present the norm of the Floquet multipliers for each pair of the parameters δ and q. In the red region of this chart $|\lambda_\pm|=1$ and therefore the solutions of the Mathieu equation are stable for these pairs of (δ,q). In the blue region $|\lambda_\pm|\neq 1$ and therefore this area corresponds to exponentially growing solutions. In the boundary between these two areas, both the eigenvalues and the eigenvectors of the monodromy matrix coalescence. Therefore, the boundary between the stable and the unstable region corresponds to exceptional points and in the most general case the solutions grow linearly with time [115]. This plot is known as the stability chart of the Mathieu equation [1,115]. For reasons that will get clear in the following, we also show in the stability chart the line $\delta=3|q|$ with black solid line. In this line, the orange and green rectangular indicate the sets of (δ,q) that were used in Fig. 4.1(a) and (b) respectively.

More generally, the Floquet theory states that the principal matrix solution is written in the form [109]

$$\mathbf{\Psi}(\tau,\tau_0)=\tilde{\mathbf{P}}(\tau,\tau_0)e^{\tilde{\mathbf{B}}(\tau_0)(\tau-\tau_0)}, \tag{4.7}$$

where the matrix $\tilde{\mathbf{B}}(\tau_0)$ depends only on the initial time τ_0 and the matrix $\tilde{\mathbf{P}}(\tau,\tau_0)$ is periodic on both times τ and τ_0, having the same period with the matrix $\mathbf{A}(\tau)$ (this period is π for the Mathieu equation). The eigenvalues of the matrix $\tilde{\mathbf{B}}(\tau_0)$ are related with the eigenvalues of the monodromy matrix – the Floquet multipliers $\lambda_\pm$ – through the relation [109]

$$\gamma_\pm=\frac{1}{\pi}\ln(\lambda_\pm). \tag{4.8}$$

The eigenvalues $\gamma_\pm$ are referred as Floquet exponents. Moreover, since $\lambda_+\lambda_-=1$, it follows that $\gamma_++\gamma_-=0 \mod 2\pi i$. In the stable region the Floquet exponents are purely imaginary and therefore we set $\gamma_\pm=\pm i\gamma$ with γ a real parameter. In Fig. 4.2(b) we present the exponent γ along

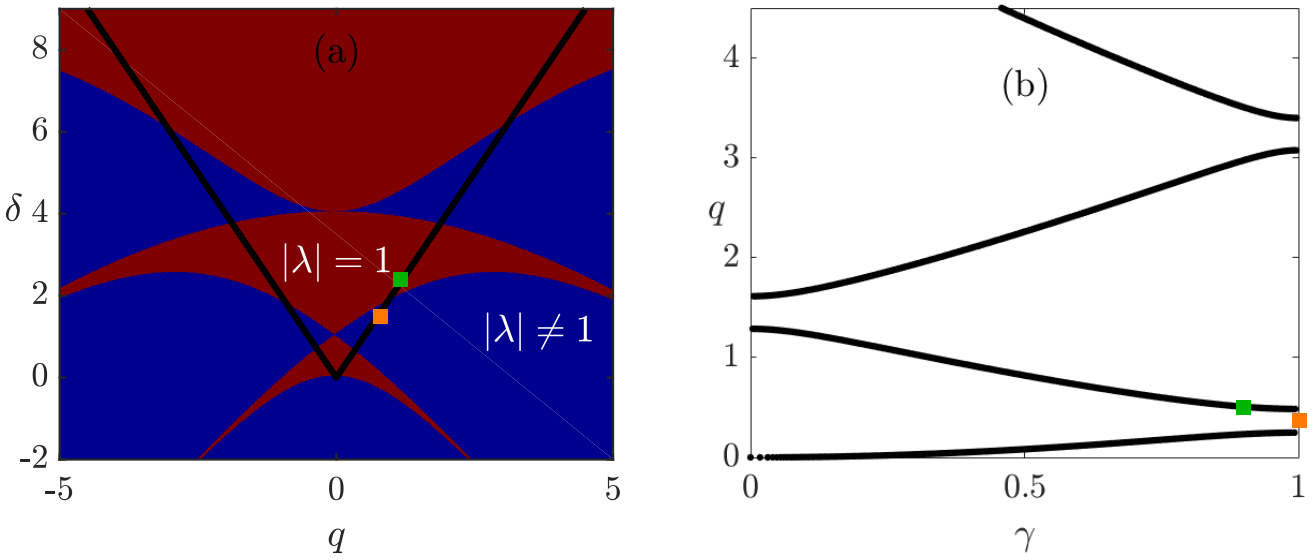

Figure 4.2: (a) Shown here is the norm of the eigenvalues $\lambda_{\pm}$ of the monodromy matrix as a function of the parameters δ and q. Also shown is the cut $\delta = 3|q|$. (b) Floquet exponent for the stable solutions as the line $\delta = 3|q|$ is scanned.

the cut $\delta = 3q$. This is a Floquet spectrum [137]. The bands correspond to the stable regions and the gaps to the unstable ones. We note here that the set of parameters that is used in Fig. 4.1(b) and is indicated with the green rectangular, results in a Floquet exponent γ equal to 0.9.

4.3 Measuring the transient amplification

In this part we will elaborate on the transient amplification that a stable solution (as the one that is shown in Fig. 4.1(b) - indicated with the green rectangular) can exhibit. One of our goals is to introduce a measure that quantifies this transient amplification. This is done in the first two subsections of this part.

The transient amplification cannot be captured by the Floquet multipliers (Floquet exponents) since they have norm one (they are purely imaginary) in the stable region of the stability chart. These eigenvalues determine the large time limit and fail to predict any transient effects. One of the tools that was developed in order to capture such transient effects is the ϵ-pseudospectrum [110]. To that end, we will study the ϵ-pseudospectrum of the monodromy matrix.

It is known that transient effects and non-normal dynamics are due to the non-normality of the matrix that propagates the initial conditions forward in time [110, 138]. A non-normal matrix has non orthogonal eigenvectors and this non-orthogonality can result to transient effects [112]. There are quantities - related with the ϵ-pseudospectrum - like the Kreiss constant and the Petermann

factors [139] that indicate the non-normality of a matrix. For this reason, we will study these quantities as well.

4.3.1 Choice of variables

For reasons that will get clear in the following, we change variables at this point. We consider the transformation $(f, \dot{f}) \rightarrow (F, G)$ with

$$F(\tau) = f(\tau)\sqrt{\omega(\tau)} \quad , \quad G(\tau) = \dot{f}(\tau)/\sqrt{\omega(\tau)}. \tag{4.9}$$

and $\omega^2(\tau) = \delta - 2q\cos(2\tau)$ (see Eq. (4.4)). This transformation is illuminated when we consider the WKB limit of Eq. (4.3), that is when $\omega(\tau)$ varies slowly with time, $\Omega << \omega$. The solution of Eq. (4.3) in the WKB limit is given by $f(\tau) = e^{\pm i\int_0^\tau \omega(r)dr}$ [118] and is predicting amplification. Yet, by choosing the variables in Eq. (4.9) we cancel this adiabatic effect: in the WKB limit the norm of the vector $\boldsymbol{\xi}(\tau) = \begin{pmatrix} F(\tau) \\ G(\tau) \end{pmatrix}$, i.e., $||\boldsymbol{\xi}(\tau)|| = \sqrt{|F(\tau)|^2 + |G(\tau)|^2}$, is constant and equal to $\sqrt{|F(0)|^2 + |G(0)|^2}$. Away from the WKB limit the norm of the vector $\boldsymbol{\xi}(\tau)$ is not constant and this is when non-trivial amplification is captured in the sense that is not predicted by WKB.

In Fig. 4.3 we present an example. In all of the three panels we show the evolution of the variables $F(0) = 1/\sqrt{2}$, $G(0) = 1/\sqrt{2}$ and the norm of the vector $\boldsymbol{\xi}(\tau)$ for three different sets of δ and q. In (a) we set $q = 0.82$ in (b) $q = 4.4$ (c) $q = 20.03$ and in all of these three cases we also set $\delta = 3q$. We used these particular sets of δ and q because all these choices result in Floquet exponents equal to $\gamma = 0.5$. By inspecting this figure it is clear that as q and δ increase, the norm of the vector $\boldsymbol{\xi}(\tau)$ tends to a constant value which is its initial value. The limit of large q and δ is essentially the WKB limit of Eq.(4.4). Therefore, we get that the norm of the vector $\boldsymbol{\xi}(\tau)$ is an elegant measure for the description of the transient amplification since it is constant (and equal to $||\boldsymbol{\xi}(0)||$) in the WKB limit and it is non-constant (and oscillates) away from the WKB limit.

From the transformation that is given in Eq. (4.9), we get that outside the cone $\delta = 2|q|$ the variable $G(\tau)$ acquires singularities since the parameter $\omega^2(\tau)$ becomes zero at some instants of time. As a result, we restrict our analysis only in the area that locates inside the cone $\delta = 2|q|$. Outside of this cone, we have to consider another suitable transformation, based on which we can describe the transient amplification properly. However, the amplification is not qualitatively different in the regions outside and inside of the cone $\delta = 2|q|$, because the initial variables $f(\tau)$ and $\dot{f}(\tau)$, which express the physical properties of the system, change smoothly across the whole stability chart.

At this point, we will show the equations that govern the dynamics of the variables $F(\tau)$ and $G(\tau)$ and we will express the general solution of these equations in terms of a propagating matrix. Essentially, we will follow a similar procedure to the one that we followed for the variables $f(\tau)$ and $\dot{f}(\tau)$. Notice first that the equations that the new variables $F(\tau)$ and $G(\tau)$ satisfy, are also

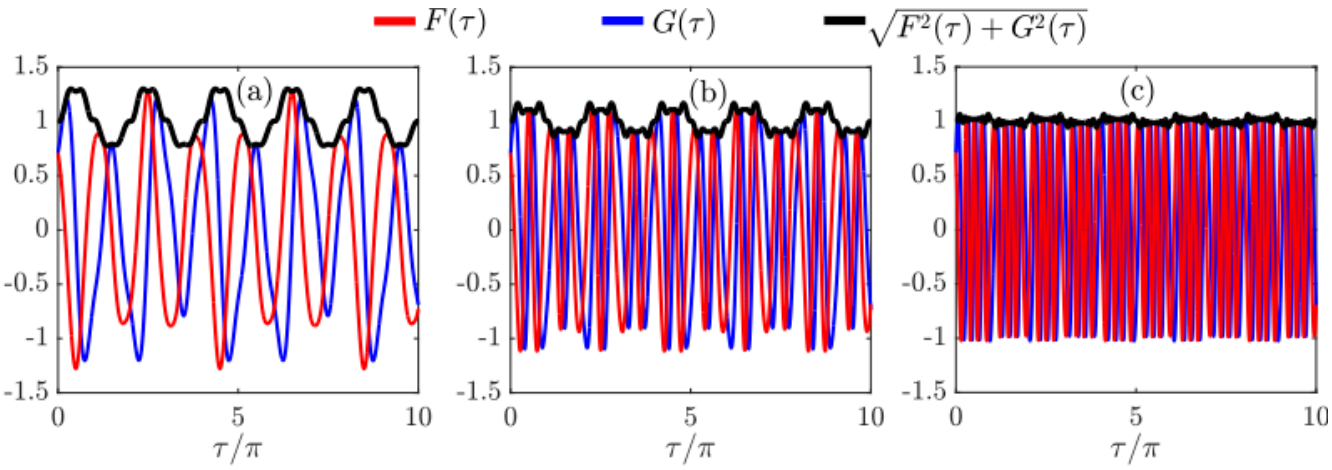

Figure 4.3: Shown here is the evolution of the variables $F(0)$ and $G(0)$ as well the quantity $\sqrt{X^2(\tau)+Y^2(\tau)}$. In all cases we set $\delta = 3q$ and in (a) $q = 0.82$, (b) $q = 4.4$, (c) $q = 20.03$.

written in the form of a system of two linear differential equations

$$\dot{\boldsymbol{\xi}}(\tau) = \mathbf{C}(\tau)\boldsymbol{\xi}(\tau) \tag{4.10}$$

with $\mathbf{C}(\tau) = \begin{pmatrix} \dot{\omega}/2\omega & \omega \\ -\omega & -\dot{\omega}/2\omega \end{pmatrix}$. The general solution of Eq. (4.10) is written in the form

$$\boldsymbol{\xi}(\tau) = \boldsymbol{\Phi}(\tau,\tau_0)\boldsymbol{\xi}(\tau_0), \tag{4.11}$$

where $\boldsymbol{\xi}(\tau_0) = \begin{pmatrix} F(\tau_0) \\ G(\tau_0) \end{pmatrix}$ is the vector that contains the initials conditions and the matrix $\boldsymbol{\Phi}(\tau,\tau_0)$ evolves these initial conditions forward in time. Hereafter, in order to discriminate the matrix $\boldsymbol{\Phi}(\tau,\tau_0)$ from the matrix $\boldsymbol{\Psi}(\tau,\tau_0)$ (that evolves the variables $f(\tau_0)$ and $\dot{f}(\tau_0)$ in time), we will call the matrix $\boldsymbol{\Phi}(\tau,\tau_0)$ as the propagator. Using the transformation that is given in Eq. (4.9), it is straightforward to show that the propagator $\boldsymbol{\Phi}(\tau,\tau_0)$ is given in terms of the principal matrix $\boldsymbol{\Psi}(\tau,\tau_0)$ through the relation

$$\boldsymbol{\Phi}(\tau,\tau_0) = \begin{pmatrix} \dfrac{\sqrt{\omega(\tau)}}{\sqrt{\omega(\tau_0)}}\Psi_{11}(\tau,\tau_0) & \sqrt{\omega(\tau)\omega(\tau_0)}\Psi_{12}(\tau,\tau_0) \\ \dfrac{1}{\sqrt{\omega(\tau)\omega(\tau_0)}}\Psi_{21}(\tau,\tau_0) & \dfrac{\sqrt{\omega(\tau_0)}}{\sqrt{\omega(\tau)}}\Psi_{22}(\tau,\tau_0) \end{pmatrix}. \tag{4.12}$$

Recall that $\omega^2(\tau) = \delta - 2q\cos(2\tau)$ and therefore $\omega(\tau_0) = \omega(\tau_0+\pi)$. Using the latter property, we can easily show that the eigenvalues of the monodromy matrix $\boldsymbol{\Phi}(\tau_0+\pi,\tau_0)$ are the same with the eigenvalues of the monodromy matrix $\boldsymbol{\Psi}(\tau_0+\pi,\tau_0)$. Namely, the eigenvalues of $\boldsymbol{\Phi}(\tau_0+\pi,\tau_0)$

are the Floquet multipliers $\lambda_{\pm}$. This should not come as a surprise, since there is no reason for the stability properties of the new variables $F(\tau)$ and $G(\tau)$ to be different from from the stability properties of the initial variables $f(\tau)$ and $\dot{f}(\tau)$.

We close this part, by exploiting the Floquet theory again which states that the propagator $\mathbf{\Phi}(\tau_0 + \pi, \tau_0)$ is written as a product

$$\mathbf{\Phi}(\tau, \tau_0) = \mathbf{P}(\tau, \tau_0) e^{\mathbf{B}(\tau_0)(\tau - \tau_0)}, \tag{4.13}$$

where $\mathbf{P}(\tau, \tau_0)$ is π-periodic on both τ and τ_0 and the matrix $\mathbf{B}(\tau_0)$ depends only on τ_0. Notice that that we are able to apply the Floquet theory because the matrix $\mathbf{C}(\tau)$ (see Eq. (4.10)) is periodic as well.

4.3.2 Choice of measure

As we noted before, the norm of the vector $\boldsymbol{\xi}(\tau)$ quantifies properly the transient amplification. However, it depends on the choice of the initial vector $\boldsymbol{\xi}(\tau_0)$. Therefore, if we are interested to know the maximum possible amplification of the vector $\boldsymbol{\xi}(\tau)$ over all initial conditions, is reasonable to compute the quantity

$$\max_{||\boldsymbol{\xi}(\tau_0)||=1} \frac{||\boldsymbol{\xi}(\tau)||}{||\boldsymbol{\xi}(\tau_0)||} = \max_{||\boldsymbol{\xi}(\tau_0)||=1} \frac{||\mathbf{\Phi}(\tau, \tau_0)\boldsymbol{\xi}(\tau_0)||}{||\boldsymbol{\xi}(\tau_0)||}. \tag{4.14}$$

Namely, we consider a maximization over all initial unit vectors. The quantity that is given in Eq. (4.14) is the 2-norm of the propagator matrix $\mathbf{\Phi}(\tau, \tau_0)$ since by definition

$$||\mathbf{\Phi}(\tau, \tau_0)|| = \max_{||\boldsymbol{\xi}(\tau_0)||=1} ||\mathbf{\Phi}(\tau, \tau_0)\boldsymbol{\xi}(\tau_0)||. \tag{4.15}$$

Therefore, the 2-norm of the propagator matrix $\mathbf{\Phi}(\tau, \tau_0)$ reveals the maximum amplification of the vector $\boldsymbol{\xi}(\tau)$ at time τ when the propagation starts at τ_0, out of all the initial unit vectors $\boldsymbol{\xi}(\tau_0)$.

The 2-norm of a matrix is provided by its largest singular value, as this is given by the singular value decomposition (SVD) [114]. For the case of a real matrix, such as the propagator $\mathbf{\Phi}(\tau, \tau_0)$, the SVD is the decomposition

$$\mathbf{\Phi}(\tau, \tau_0) = \mathbf{U}(\tau, \tau_0)\mathbf{\Sigma}(\tau, \tau_0)\mathbf{V}^T(\tau, \tau_0) \tag{4.16}$$

where the matrices $\mathbf{V}(\tau, \tau_0)$ and $\mathbf{U}(\tau, \tau_0)$ are real and orthogonal and the superscript ^{T} denotes the transpose. The matrix $\mathbf{\Sigma}(\tau, \tau_0)$ is diagonal and its elements are real, nonnegative and are arranged in descending order. These diagonal elements are called the singular values $\sigma_i(\tau, \tau_0)$ with $i = 1, 2, ..., N$ and N is the dimension of the matrix (in our problem $N = 2$). The largest singular value - that is $\sigma_1(\tau, \tau_0)$ - is the 2-norm of the matrix $\mathbf{\Phi}(\tau, \tau_0)$. The SVD provides also the initial conditions that are amplified the most for a given set of initial and final times, τ and τ_0. These

initial conditions are the elements of the first column of the orthogonal matrix $\mathbf{V}(\tau, \tau_0)$ [113].

Figure 4.4 illustrates an example. We used the same set of parameters (δ, q) that we used in Fig. 4.1(b) and we set the initial time at $\tau_0 = 0$. In Fig. 4.4(a) we present the norm of the propagator $\mathbf{\Phi}(\tau, 0)$ as a function of the time τ. Clearly, the norm exceeds 1 at almost all times and reveals that the solution of the Mathieu equation can be transiently amplified for this set of parameters (δ, q) at almost all times. Also, it appears that the norm of the propagator is periodic with a period of 10π. We stress here that when the exponent γ is a proper fraction m_1/m_2, then the propagator is of period at most $m_2\pi$. Recall that this set of parameters returns a Floquet exponent that is equal to 0.9 and that it why the norm of the propagator oscillates with a period of 10π. Therefore, the value that is indicated with a blue dashed line and is captured at $\tau = 5.32\pi$ is the overall maximum value of $||\mathbf{\Phi}(\tau, 0)||$, it is namely the $\max_{\tau} ||\mathbf{\Phi}(\tau, 0)||$. This maximum is the largest possible transient amplification that a stable solution of the Mathieu equation can exhibit (for this set of parameters (δ, q)), when the propagation starts at $\tau_0 = 0$ under the proper initial condition given by SVD.

To shed some light, we consider two different sets of initial conditions $(F(0), G(0))$ and in Fig. 4.4(b) and (c) we present their time evolution. These two sets of initial conditions are found as follows: we compute the singular value decomposition of the propagator matrix $\mathbf{\Phi}(\tau, 0)$ at 2 different times τ, at $\tau_1 = 0.8\pi$ and at $\tau_2 = 5.32\pi$. From the SVD we find the matrices $\mathbf{V}(\tau_1, 0)$ and $\mathbf{V}(\tau_2, 0)$ and we use the first columns of these two matrices as the two different sets of initial conditions in Fig. 4.4(b) and Fig. 4.4(c) respectively. These two different sets of initial conditions yield the maximum value of the norm of the vector $\boldsymbol{\xi}(\tau)$ at the final times $\tau_1 = 0.8\pi$ and $\tau_2 = 5.32\pi$ accordingly. To visualize this, we also present in Fig. 4.4(b) and (c) the norm $||\boldsymbol{\xi}(\tau)||$ (with a solid

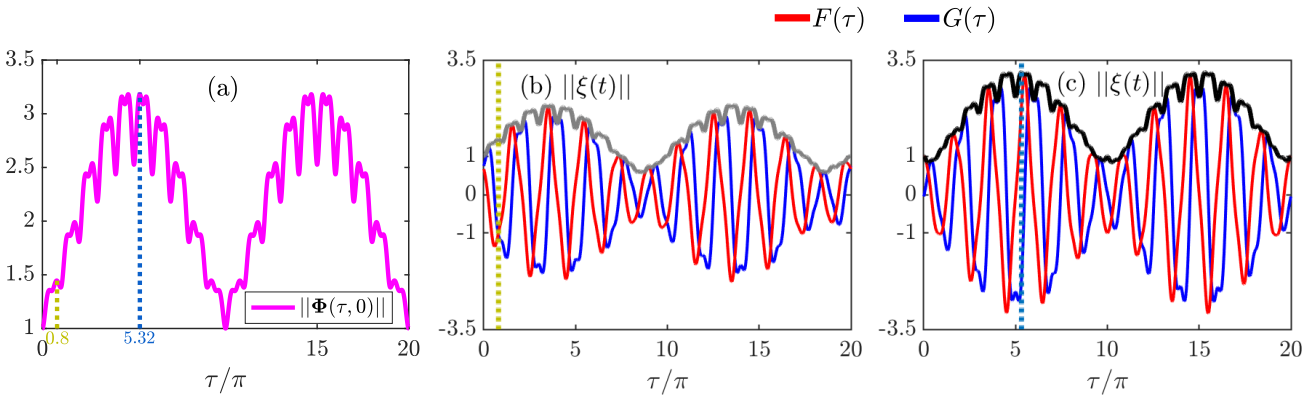

Figure 4.4: We set the initial time τ_0 at zero and we used the same set of (δ, q) that we also used in Fig. 4.1(b) - green rectangular. (a) Norm of the matrix $\mathbf{\Phi}(\tau, 0)$. (b) Evolution of the initial conditions $F(0) = 0.7469$ and $G(0) = 0.6651$. These initial conditions maximize the norm of the vector $\boldsymbol{\xi}(\tau)$ at time $\tau = 0.8\pi$. (c) Same as (b) with initial conditions $X = F(0) = -0.0481$ and $G(0) = 0.9988$. These initial conditions maximize the norm of the vector $\boldsymbol{\xi}(\tau)$ at time $\tau = 5.32\pi$.

gray curve in (b) and a solid black curve in (c)). Clearly, the black curve reaches a higher value than the gray curve at time $\tau_2 = 5.32\pi$. However, even though it is not visible, the gray curve takes a higher value than the black curve at time $\tau_1 = 0.8\pi$.

4.3.3 Pseudospectrum analysis

As we mentioned in the beginning of this section, the spectrum of the monodromy matrix – the Floquet multipliers $\lambda_\pm$ – do not give any information regarding the transient amplification of a bounded solution. These determine the asymptotic behavior of the solution, namely whether it is bounded or not. On the contrary, the ϵ-pseudospectrum [110] of the monodromy matrix can detect transients. First of all, the ϵ-pseudospectrum of a matrix (for instance of the monodromy matrix $\mathbf{\Phi}(\tau_0 + \pi, \tau_0)$) is the set of all the complex numbers z, such that

$$||(z - \mathbf{\Phi}(\tau_0 + \pi, \tau_0))^{-1}|| > \epsilon^{-1}, \tag{4.17}$$

with $\epsilon > 0$. We denote this set as $\sigma_\epsilon[\mathbf{\Phi}(\tau_0 + \pi, \tau_0)]$. It follows that in the limit of $\epsilon \to 0$, then $\sigma_\epsilon[\mathbf{\Phi}(\tau_0+\pi, \tau_0)] \to \sigma[\mathbf{\Phi}(\tau_0+\pi, \tau_0)]$ where $\sigma\left[\mathbf{\Phi}(\tau_0 + \pi, \tau_0)\right]$ is the spectrum of the monodromy matrix. Notice that, unlike the spectrum, the pseudospectrum is not uniquely defined and depends on the choice of ϵ.

In Fig. 4.5 we present an example. We set the initial time τ_0 again at zero and we use the same set of parameters (δ, q) that we also used in Fig. 4.1(b). In Fig. 4.5(a) the two crosses correspond to the two Floquet multipliers. Notice that these are complex conjugates and lie in the unit circle in the complex plane (gray circle) since this set of parameters (δ, q) belongs in the stable region of the stability chart. In this panel, we also show with the four solid closed curves the boundaries of the ϵ-pseudospectrum, for four values of $\epsilon : 0.08, 0.14, 0.2$ and 0.26. The value of $\epsilon = 0.08$ corresponds to the closed cyan curves that surround the Floquet multipliers. As the value of ϵ gradually increases these two curves extend to the complex plane and for some value of ϵ they touch and unite in a single curve. For instance, the boundary of the ϵ-pseudospectrum for $\epsilon = 0.14$ is the single blue curve. As ϵ keeps increasing this single curve keeps extending in the complex plane (see for instance the purple line that is the boundary of the ϵ-pseudospectrum for $\epsilon = 0.26$). We note here again that these solid closed curves that we present in Fig. 4.5(a) are not the ϵ-pseudospectra of the monodromy matrix but the boundaries of the ϵ-pseudospectra. The ϵ-pseudospectra are the sets with all the complex numbers inside these curves. To shed more light, we show in Fig. 4.5(b) the norm $||(z - \mathbf{\Phi}(\pi, 0))^{-1}||$ as a function of $z \in \mathbb{C}$. Clearly, the two spikes correspond to the Floquet multipliers. The four solid closed curves are the boundaries of the ϵ-pseudospectra that are shown in (a).

The pseudospectrum provides several useful bounds for the transient amplification and it can be estimated very accurately. For example, there is a very useful lower bound for the quantity

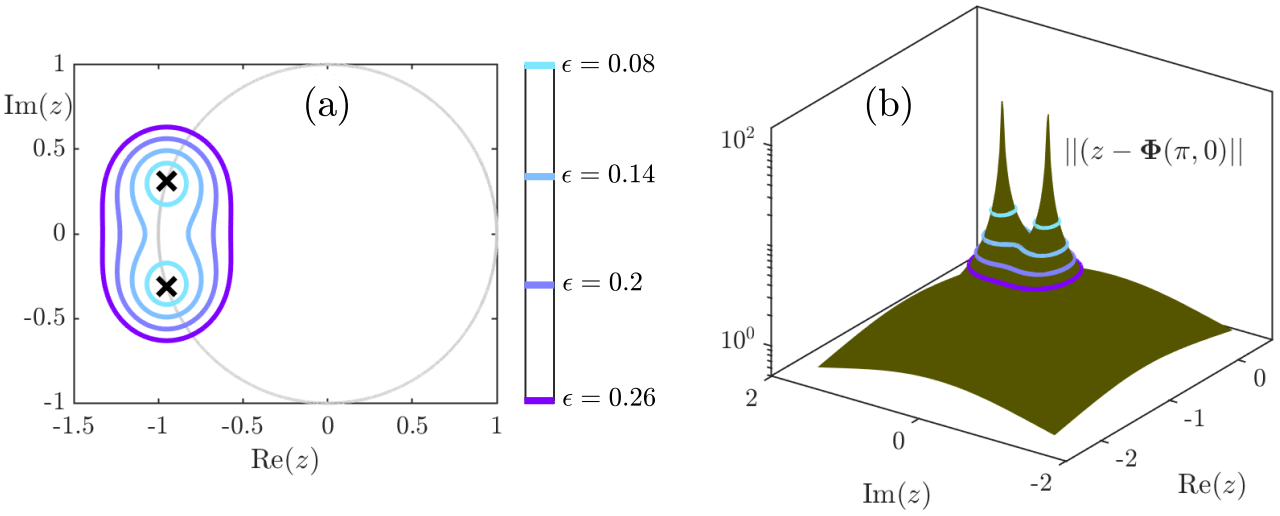

Figure 4.5: We used the set of parameters (δ, q) that we also used in Fig. 4.1(b) - green rectangular. (a) Shown here with the two crosses is the spectrum of the monodromy matrix $\mathbf{\Phi}(\pi, 0)$ and with the four solid lines the boundaries of the ϵ-pseudospectra for ϵ: 0.08, 0.14, 0.2 and 0.28. (b) Shown here is the norm $||(z - \mathbf{\Phi}(\pi; 0))^{-1}||$ as a function of $z \in \mathbb{C}$.

$\max_n ||\mathbf{\Phi}^n(\tau_0 + \pi, \tau_0)||$ with n an integer.[1] As an illustration, we present first in Fig. 4.6(a) the quantity $||\mathbf{\Phi}^n(\pi, 0)||$ for the same set of parameters (δ, q) that we used in Fig. 4.5. We also show with a faded magenta line this time the corresponding norm of the propagator $\mathbf{\Phi}(\tau, 0)$ (like in Fig. 4.4). Clearly, the maximum value of the black dots, that is the quantity $\max_n ||\mathbf{\Phi}^n(\tau_0 + \pi, \tau_0)||$, is a lower bound for the $\max_\tau ||\mathbf{\Phi}(\tau, 0)||$ and this is why it is of interest to find a lower bound for the $\max_n ||\mathbf{\Phi}^n(\tau_0 + \pi, \tau_0)||$.

This lower bound for the maximum norm of the $||\mathbf{\Phi}^n(\tau_0 + \pi, \tau_0)||$ is given by

$$\max_n ||\mathbf{\Phi}^n(\tau_0 + \pi, \tau_0)|| \geq \max_\epsilon \frac{\rho_\epsilon(\mathbf{\Phi}(\tau_0 + \pi, \tau_0)) - 1}{\epsilon} \tag{4.18}$$

where $\rho_\epsilon(\mathbf{\Phi}(\tau_0 + \pi, \tau_0))$ is the ϵ-pseudospectrum radius. The pseudospectrum radius $\rho_\epsilon(\mathbf{\Phi}(\tau_0 + \pi, \tau_0))$ is the set of all the complex numbers z such that

$$\rho_\epsilon(\mathbf{\Phi}(\tau_0 + \pi, \tau_0)) = \max\left\{|z| : z \in \mathbb{C}, ||(z - \mathbf{\Phi}(\tau_0 + \pi, \tau_0))^{-1}|| > \epsilon^{-1}\right\}. \tag{4.19}$$

The quantity at the right hand side of Eq. (4.18) which is the maximum (over ϵ) of the quantity $\frac{\rho_\epsilon - 1}{\epsilon}$, is called the Kreiss constant. In Fig. 4.6(b) we present the quantity $\frac{\rho_\epsilon - 1}{\epsilon}$ as a function of ϵ. This quantity reaches a plateau for small values of ϵ. Some insight into this plateau is

[1] Notice that the quantity $||\mathbf{\Phi}^n(\tau_0 + \pi, \tau_0)|| = ||\mathbf{\Phi}(\tau_0 + n\pi, \tau_0)||$ is the norm of the propagator at multiples of the period.

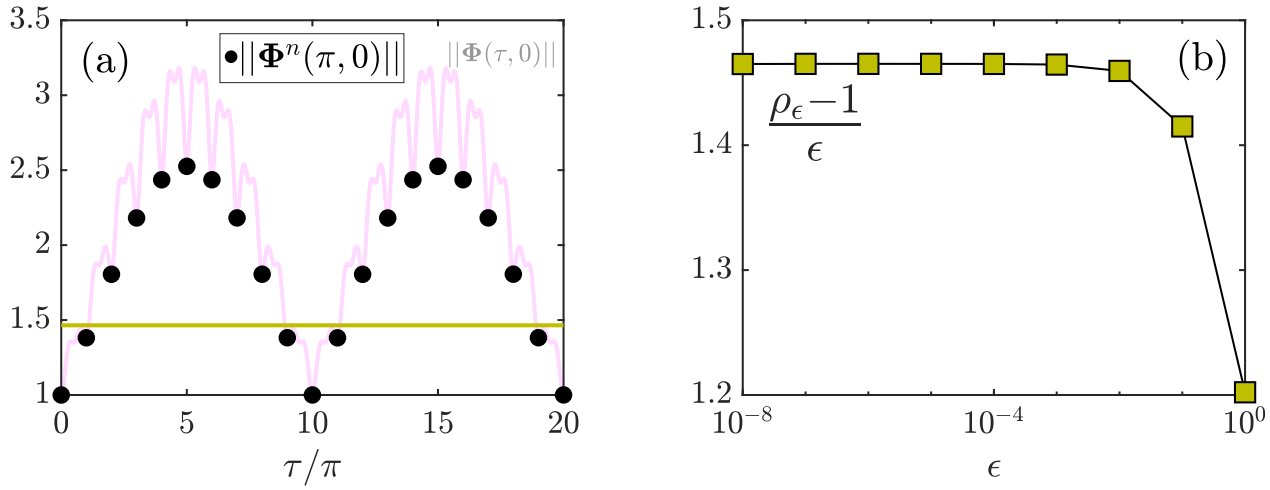

Figure 4.6: We used again the same set of parameters (δ, q) that we used in Fig. 4.1(b) - green rectangular. (a) Shown here is the norm of the monodromy matrix $||\mathbf{\Phi}^n(\pi,0)||$ with $n = 1, 2, ...20$. Also shown with a faded magenta line is the norm of the propagator, $||\mathbf{\Phi}(\tau,0)||$. The latter quantity is also shown in Fig. 4.4(a) with the magenta line. The yellow line shows the value of the discrete Kreiss constant which is a lower bound for the $\max_n ||\mathbf{\Phi}(\pi,0)^n||$. (b) Shown here is the ratio $\frac{\rho_\epsilon - 1}{\epsilon}$ as a function of ϵ. The maximum value of this ratio is the discrete Kreiss constant.

provided in Appendix D where we approximate the propagator matrix with the monodromy matrix continuously and we find closed form expressions for the Kreiss constant. Finally, in order to visualize that the Kreiss constant is indeed a lower bound for the maximum value of the norm of the monodromy matrix, we present its value in Fig. 4.6(a) with a yellow solid line. Clearly, the yellow line is below the maximum black dot.

The fact that the value of the discrete Kreiss constant exceeds one suggests that the monodromy $\mathbf{\Phi}(\pi,0)$ is non-normal, i.e. $[\mathbf{\Phi}(\pi,0), \mathbf{\Phi}(\pi,0)^\dagger] \neq 0$. For a normal matrix the value of the Kreiss constant is one. As we explained at the beginning of this section, we find transient amplification because the propagator (and the monodromy) matrix is non-normal. The non-normality of a matrix is reflected at its eigenvectors which are not orthogonal. For that reason, in the following part we briefly remind the Petermann factors because we can easily understand this non-orthogonality through these quantities.

4.3.4 Petermann factors

The Petermann factors [139] measure the nonorthogonality of the left and right eigenvectors of a matrix and thus they indicate the non-normality of this matrix. We are interested to measure the non-normality of the monodromy matrix $\mathbf{\Phi}(\tau_0 + \pi, \tau_0)$ and therefore our goal is to compute the Petermann factors of $\mathbf{\Phi}(\tau_0 + \pi, \tau_0)$. However, we will give first the definition of the Petermann

factors of a general matrix that is of dimension N and after that we will restrict to the monodromy matrix $\mathbf{\Phi}(\tau_0+\pi,\tau_0)$. We denote this general matrix of dimension N as $\mathbf{Q}$ and its N eigenvalues as λ_i, with $i=1,2,...N$. We denote the N right eigenvectors of $\mathbf{Q}$ as $\boldsymbol{u}_i$, namely it holds $\mathbf{Q}\boldsymbol{u}_i=\lambda_i\boldsymbol{u}_i$, and we also denote its left eigenvectors as $\boldsymbol{v}_i$, namely $\boldsymbol{v}_i^\dagger\mathbf{Q}=\lambda_i\boldsymbol{v}_i^\dagger$, where † denotes complex conjugate transpose. Then, the N Petermann factors of this general matrix $\mathbf{Q}$ are defined as

$$K_i=\frac{||u_i||\ ||v_i||}{|v_i^\dagger u_i|},\quad i=1,2,...,N. \tag{4.20}$$

If the matrix $\mathbf{Q}$ is normal, we can take its right and left eigenvectors to be the same and therefore all of the N Petermann factors K_i are equal to 1.

Going back to the monodromy matrix $\mathbf{\Phi}(\tau_0+\pi,\tau_0)$ of our problem, we note first that this matrix depends on the initial time τ_0. Therefore, its two right and two left eigenvectors depend also on τ_0. We denote these right eigenvectors as $\boldsymbol{u}_\pm(\tau_0)$ and the corresponding left ones as $\boldsymbol{v}_\pm(\tau_0)$. Since the determinant of $\mathbf{\Phi}(\tau_0+\pi,\tau_0)$ is one, we immediately get that the two right and two left eigenvectors of $\mathbf{\Phi}(\tau_0+\pi,\tau_0)$ are complex conjugates, namely $\boldsymbol{u}_+=\overline{\boldsymbol{u}}_-$ and $\boldsymbol{v}_+=\overline{\boldsymbol{v}}_-$. Therefore, the two Petermann factors $K_\pm$ of the monodromy matrix are equal, $K_+=K_-=K$. As an example, we used the set of parameter (δ,q) that we have mainly used so far (see Fig. 4.4, Fig. 4.5 and Fig. 4.6) and we set again the initial time at $\tau_0=0$. We computed the Petermann factors of $\mathbf{\Phi}(\pi,0)$ and we found that they are approximately equal to 2.147. As we expected, we found Petermann factors that are not equal to one, since this matrix is non-normal.

4.4 Impact of the initial time τ_0

Up to now, the only thing that we have mentioned regarding the initial time τ_0, is that the spectrum of the monodromy matrix – the two Floquet multipliers $\lambda_\pm$ – do not depend on it. And this is due to the similarity of the monodromy matrices that propagate initial conditions from different initial times [109]. Regarding the phenomenon of the transient amplification though, there is no reason for it to be independent on the choice of the initial time τ_0. Therefore, in this part we explore the impact of τ_0 at these transient effects.[2]

We begin with the illustration of an example that is shown in Fig. 4.7. Once more, we used the same set of (δ,q) that we used in Fig. 4.1(b). In the top three panels of this figure, we present with the magenta lines the norm of the propagator $\mathbf{\Phi}(\tau,\tau_0)$ as a function of the final time τ, for three choices of the initial time $\tau_0=0.2\pi,0.32\pi,0.5\pi$. In these panels, we also present with the black dots the quantity $||\mathbf{\Phi}^n(\tau_0+\pi,\tau_0)||$ with n an integer (we stress here again that this is the norm of the propagator at multiples of the period). What we immediately get from these four panels is that the norm of the propagator and its sampling at each period change as the initial time τ_0 changes.

[2]Notice that in all the examples that we have presented so far, we have set the initial time to be zero.

To get a first insight into the latter result, at the three lower panels of Fig. 4.7 we present the boundaries of the pseudospectrum of the monodromy matrix $\mathbf{\Phi}(\tau_0+\pi,\tau_0)$ for the same initial times that we used at the corresponding upper panels and for the four values of $\epsilon = 0.08, 0.14, 0.2, 0.26$ that we also used in Fig. 4.5. Clearly, the pseudospectrum of the monodromy matrix depends on τ_0 since its boundaries extend/shrink into the complex plane as the initial time changes. At these lower panels we also show the spectrum of the monodromy matrix (with the crosses) that does not change as the initial time τ_0 changes.

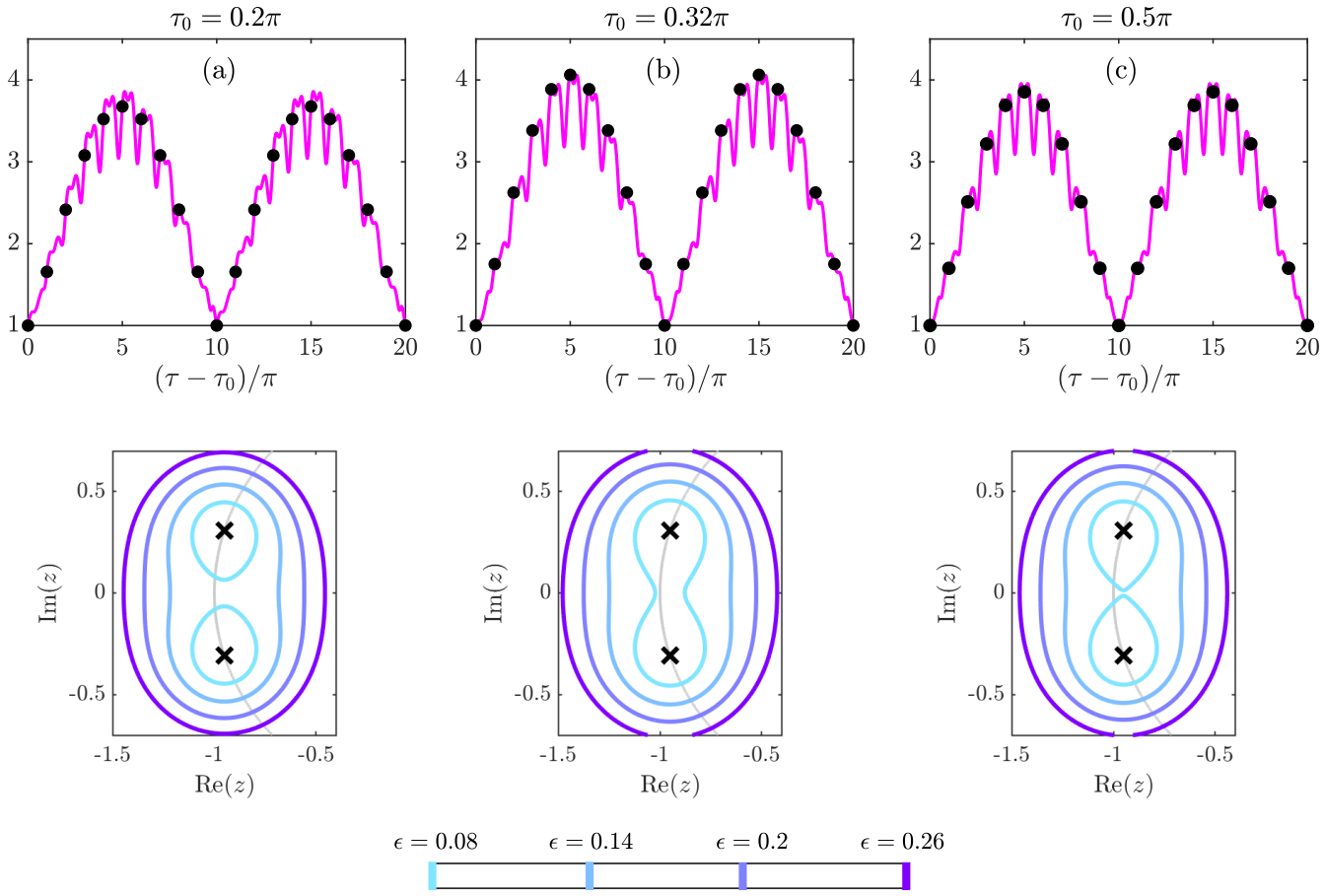

Figure 4.7: We used the set of parameters (δ, q) that we also used in Fig. 4.1(b) - green rectangular. Upper panels: Shown here are the quantities $||\mathbf{\Phi}(\tau,\tau_0)||$ and $||\mathbf{\Phi}(\tau_0+\pi,\tau_0)||$ for (a) $\tau_0 = 0.2$, (b) $\tau_0 = 0.32$ and (c) $\tau_0 = 0.5$. Bottom figures: Corresponding boundaries of the pseudospectra for ϵ =0.08, 0.14, 0.2 and 0.26.

A close look at Fig. 4.7(b) reveals that the black dot with the maximum value coincides with the magenta line at its maxima. This drives us to compute the quantities $\max_{\tau} ||\mathbf{\Phi}(\tau,\tau_0)||$ and $\max_{n} ||\mathbf{\Phi}^n(\tau_0+\pi,\tau_0)||$ as a function of the initial time τ_0. The results are shown in Fig. 4.8(a). Clearly, these two curves touch at their maxima, meaning that the quantity $\max_{\tau_0}[\max_{\tau} ||\mathbf{\Phi}(\tau,\tau_0)||]$ is equal to the $\max_{\tau_0}[\max_{n} ||\mathbf{\Phi}^n(\tau_0+\pi,\tau_0)||]$. We emphasize that the $\max_{\tau_0}[\max_{\tau} ||\mathbf{\Phi}(\tau,\tau_0)||]$, contains

a maximization in the initial conditions, in the final time τ, and in the initial time τ_0 and is therefore the overall biggest amplification that we can get for this set of parameters (δ, q). And according to the results that are shown in Fig. 4.8(a) this overall maximum is provided merely by the monodromy matrix. We note here that this finding is not a peculiarity of the specific choice (δ, q) that we used here since we have verified it using several parameters δ and q (that all belong in the stable regime of the stability chart).

As a next step we compute the Kreiss constant as a function of the initial time τ_0. The results are shown in Fig. 4.8(b). Notice that this curve has the same pattern with the ones that are shown in Fig. 4.8(a) and suggests that the monodromy matrix $\mathbf{\Phi}(\tau_0 + \pi, \tau_0)$ becomes the most non-normal for $\tau = 0.32\pi$ and the least non-normal for $\tau_0 = 0$. Furthermore, we compute the Petermann factors $K = K_+ = K_-$ of the monodromy matrix $\mathbf{\Phi}(\tau_0 + \pi, \tau_0)$ as a function of τ_0. The results are illustrated in Fig. 4.8(c). Notice that this curve has the same pattern with all the other curves that are shown in the same figure. Again, we conclude that the monodromy matrix becomes the most non-normal at $\tau = 0.32\pi$.

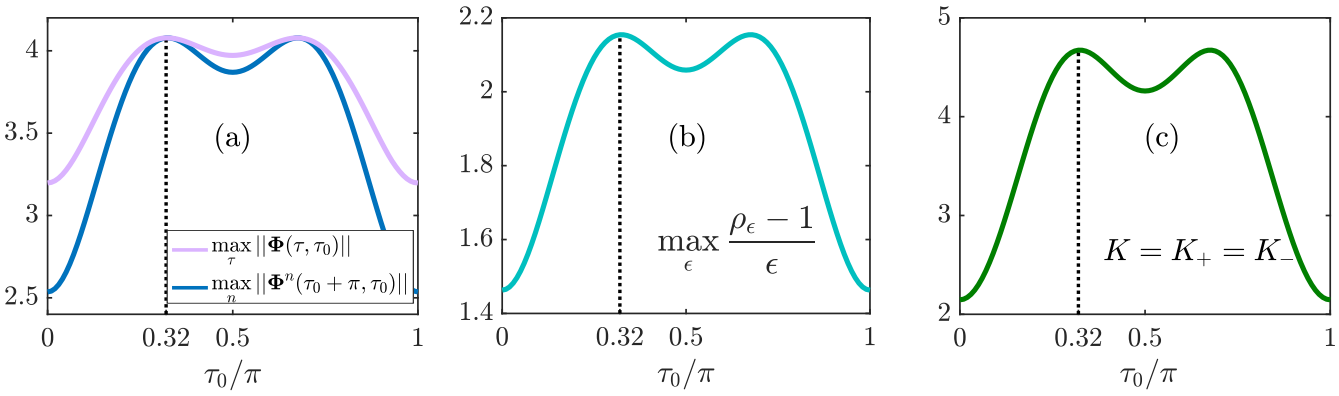

Figure 4.8: We used the set of parameters (δ, q) that we also used in Fig. 4.1(b) - green rectangular. (a) Shown here is the $\max_\tau ||\mathbf{\Phi}(\tau, \tau_0)||$ and the quantity $\max_n ||\mathbf{\Phi}(\tau_0 + \pi, \tau_0)||$ with n an integer. (b) Discrete Kreiss constant as a function of the initial time τ_0. (c) Petermann factors $K = K_+ = K_-$ of the monodromy matrix as as a function of the initial time τ_0.

4.4.1 Maximum transient amplification

Up to now, we have used a particular set of the parameters δ and q in the most examples that we have presented. For this reason, we will calculate in this part the overall maximum transient amplification that all the stable solutions of the Mathieu equation can exhibit. Namely, we will calculate the quantity

$$\max_{\tau_0} \left[\max_\tau ||\mathbf{\Phi}(\tau, \tau_0)|| \right], \tag{4.21}$$

at the stable region of the stability chart, that is inside the cone $\delta = 2|q|$. The results are shown in Fig. 4.9(a). We note here that we calculated the quantity that is given in Eq. (4.21), only in the stable region that locates inside the cone $\delta = 2|q|$. Clearly, for the set of (δ, q) that locate close to the unstable area, the corresponding solutions are intensively amplified. Furthermore, the maximum transient amplification of a solution grows as the boundary with the unstable region is approached.

A natural step in our analysis, is to compute the quantity

$$\max_{t_0}\left[\max_{n}||\mathbf{\Phi}(t_0+\pi,t_0)^n||\right] \tag{4.22}$$

as well, since in the previous part we concluded that the is the same with the corresponding quantity that is given in Eq. (4.21). The results are shown in Fig. 4.9(b). Notice that both the quantities that are shown in Fig. 4.9(a) and (b) match perfectly. This supports our finding that merely the monodromy matrix provides the overall maximum amplification that the stable solutions of the Mathieu equation exhibit. For that reason we state the following as a conjecture:

Conjecture *Given the Floquet representation of a propagator matrix* $\mathbf{\Phi}(t,t_0)$*, namely* $\mathbf{\Phi}(t,t_0) = \mathbf{P}(t,t_0)e^{\mathbf{B}(t_0)(t-t_0)}$ *where* $\mathbf{P}(t,t_0)$ *is a* T*-periodic matrix on both times, the following relation holds*

$$\max_{t_0}\left[\max_{t}||\mathbf{\Phi}(t,t_0)||\right] = \max_{t_0}\left[\max_{n}||\mathbf{\Phi}(t_0+nT,t_0)||\right]. \tag{4.23}$$

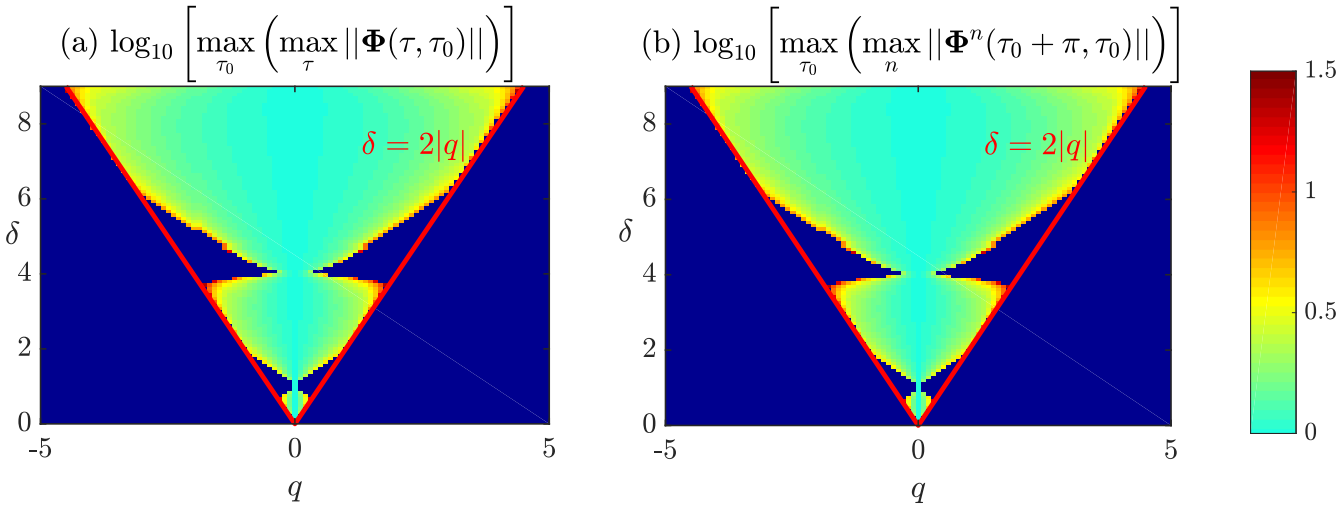

Figure 4.9: Shown here are the quantities (a) $\log_{10}\{\max_{\tau_0}\left[\max_{\tau}||\mathbf{\Phi}(\tau,\tau_0)||\right]\}$ and (b) $\log_{10}\{\max_{\tau_0}\left[\max_{n}||\mathbf{\Phi}^n(\tau_0+\pi,\tau_0)||\right]\}$, at the stable regime inside the cone that is formed by the line $\delta = 2|q|$.

4.5 Concluding remarks

In this chapter we have made a comprehensive investigation of the transient amplification exhibited by the stable solutions of the Mathieu equation. As a last remark we give here an example of a wave whose evolution is governed by Eq. (4.1) and that is transiently amplified in time. We remind that we have applied the method of separation of the variables and we have written the solution of the wave equation (4.1) as $\psi(x,t) = h(x)f(t)$ where $f(t)$ is a solution of the Mathieu equation and $h(x) = Ae^{ikx} + Be^{-ikx}$ In the example that is illustrated in Fig. 4.10 we set $A = 1$ and $B = 0$, we use the set of parameters (δ, q) that is indicated with the green rectangular and we set the initial time at $\tau_0 = 0.32\pi$, which as we have seen in Section 4.4 results in the maximization of the norm that we have chosen. We also use as initial conditions $f(0)$ and $\dot{f}(0)$ the ones that the SVD yields. In Fig. 4.10 we present the real part of the solution $\psi(x,t)$ and the result is a standing wave that is transiently amplified in time.

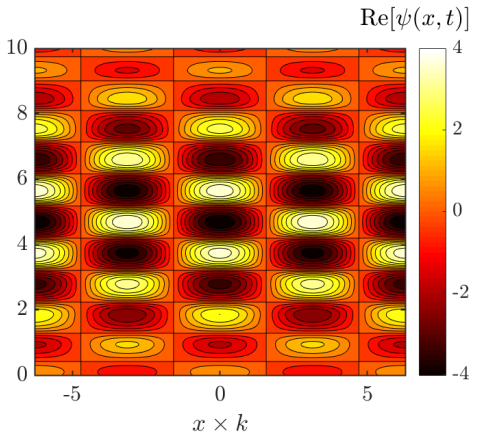

Figure 4.10: Example of a standing wave that is transiently amplified in time.

Chapter 5

Summary and perspectives

In this thesis, we explored the wave propagation in space or time varying media aiming to shed light and understand in depth some phenomenological aspects which have not been yet explored in detail. Based on the findings of the present thesis a very general future perspective is to explore the wave propagation in space-time varying media, since these kind of media have attracted great interest over the last years [98].

In the context of wave propagation in space varying media, we explored the effect of a perturbation in the transmittance of a periodic potential with mirror symmetric cells (Chapter 1). Due to periodicity, the transmittance had a band-like structure form and each band was consisting of at least $N-1$ perfect transmission resonances (PTRs), N being the number of the mirror symmetric cells. Employing Dirac scatterers we achieved to develop a systematic way to perturb the set-up so that specific PTRs survive after its modification.

Both the unperturbed and perturbing potentials that we considered in Chapter 1 were real. Yet the transmittance of a periodic potential that is complex and $\mathcal{PT}$-symmetric, has also a band-like structure form and supports PTRs in each band [140]. Therefore, it would be of interest to investigate whether the results that were presented in Chapter 1, could be generalized to the case of a complex and $\mathcal{PT}$-symmetric periodic potential.

The perturbing potential that we used in Chapter 1 comprised Dirac scatterers - for simplicity. Another perspective is to construct a perturbing potential that preserves PTRs but does not comprise Dirac scatterers. This could reveal additional phenomena and would make the problem more easily realizable in an experimental setup.

We also investigated the spectral properties of a finite periodic dimer chain possessing spatial perturbations due to disorder (Chapter 2). In the clean limit (no disorder) the frequency spectrum of the chain showed a gap and depending on the stiffness couplings, two modes whose frequency lied in the middle of the gap were supported (topological edge modes). We found that under a strong chiral disorder, the localization length of the edge modes diverged, indicating the occurrence of a topological phase transition.

It would be interesting to verify the results that were presented in Chapter 2 in an experimental platform, for instance in an electric circuit [141]. Moreover, the extension of these findings to mechanical systems that are of higher dimension could reveal new phenomena.

In the framework of time-varying media, we considered that the couplings of the dimer chain (in the clean limit - no disorder) varied with time (Chapter 3). Our goal was to transfer a topological edge mode from the chain's one end to the other in minimum time. We used an optimal control method and we found a simple protocol – we called it 3-step up protocol – consisted of three time intervals with linear increase, constant and linear decrease of the springs stiffness parameters that resulted in a fast and robust (against disorder) transfer of the edge mode. An interesting result of our analysis in Chapter 3, was the emergence of the phenomenon of amplification of the transferred mode, which is absent in the corresponding quantum systems, for example in the transfer of qubits [97].

For the experimental realization of the transfer process that we studied in Chapter 3, it is important to investigate some aspects of this problem further. For instance, a more thorough study of the impact of the disorder is important. We have investigated the impact of one form of disorder, but other sources should be studied as well. Also, the total time needed for the transfer to be successful, depends on the size of the chain and therefore a thorough study of this issue is of importance as well.

Moreover, it would be of interest to compare the method that we used in Chapter 3 with other methods of shortcuts to adiabaticity. For instance, the authors in ref. [96] suggested a method for state transfer in a quantum topological chain (Su-Schrieffer-Heeger chain). This method could be applied at the mechanical chain that we considered in Chapter 3.

The under system in Chapter 3 was non-autonomous. We have taken this into account when we optimized the fidelity over the initial edge mode's phase of oscillation. We showed that this initial phase had a strong impact at the whole transfer process, since it could lead to either amplification or disamplification of the transferred mode. It would be of interest to explore the impact of the initial phase in more depth. For instance, we could quantify the degree of adiabaticity of the transfer process more rigorously (we have used the adiabatic invariant in this chapter) and investigate whether this degree is affected by the initial phase.

The phenomenon of amplification that we encountered in Chapter 3, set the frame of our study on the transient amplification of a wave that propagates in an infinite medium whose properties vary periodically with time (Chapter 4). We considered wave dynamics governed by the Mathieu equation and we explored the transient amplification of its stable solutions. We have searched for the global maximum transient amplification by optimizing the initial conditions and the initial start of the process and we claimed that the knowledge of the monodromy matrix is sufficient to derive this global maximum.

The results that were illustrated in Chapter 4 open a lot of research directions. First of all, the addition of a loss term would make the model realizable in experimental setups and therefore an extensive study of this is needed. Some initial numerical results for the impact of loss are illustrated in Fig. 5.1.

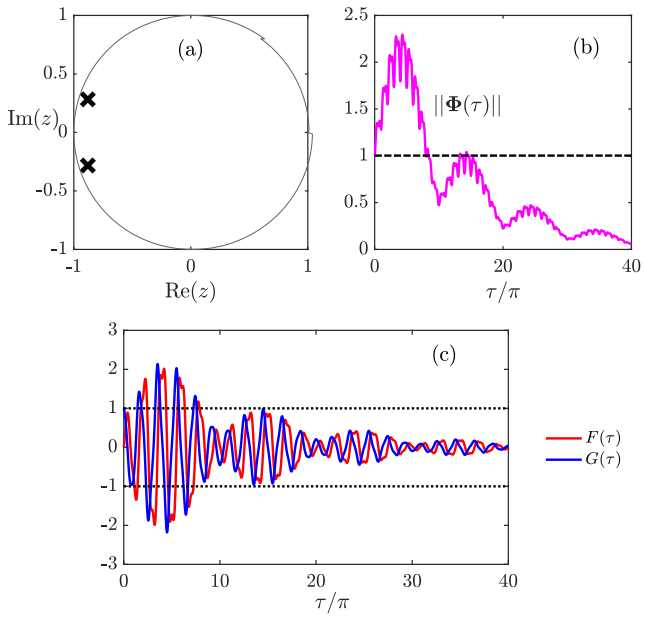

Figure 5.1: Mathieu equation with loss. (a) The eigenvalues of the monodromy matrix lie inside the unit circle. (b) The propagator is a non normal matrix. (c) Example of transient amplification of the solution.

In particular, we consider the Mathieu equation with loss: $\ddot{x}+\epsilon\dot{x}+\omega^2(t)x = 0$ and then we change variables to the ones that are given in Eq. (4.9) in Chapter 4. In Fig. 5.1(a) we present with the crosses the eigenvalues of the monodromy matrix in the complex plane. The two eigenvalues of the monodromy matrix lie inside the unit circle (shown with the gray solid curve) and therefore the solution decays asymptotically. In Fig. 5.1(b) we present the norm of the propagator (this figure is the analogous of Fig. 4.4(a) that we presented in Chapter 4). Finally, in Fig. 5.1(c) we present the evolution of the initial conditions $F(0) = 0$ and $G(0) = 1$. Notice that even though the solution decays asymptotically, it can be transiently amplified since the propagator is still a non normal matrix.

Another perspective is to study the transient amplifying effects of other time-modulated systems. In particular, we aim to study a relevant time-dependent system in fuid mechanics, first because the ϵ-pseudospectrum has its orginigs in this area of physics and second because the Mathieu equation emerges in many problems in hydrodynamics. For instance, it is a known fact that all 2-dimensional, incompressible, time-independent elliptic flows are bounded. Meaning that if we impose a perturbation at such a time-independent elliptic flow, then the energy of the perturbation remains bounded with time. For example, in Fig. 5.2(a) we present the velocity field $\boldsymbol{u}_0$ of such an elliptic flow and in the panel (b) we present the energy of a compressible perturbation that we impose at this flow (the perturbation has random initial velocity and pressure). Notice that the energy of the perturbation is bounded. Yet, if we vary the shape of the elliptic flow with time, i.e., $\boldsymbol{u}_0 = \boldsymbol{u}_0(T)$, then the energy of the perturbation can grow with time.

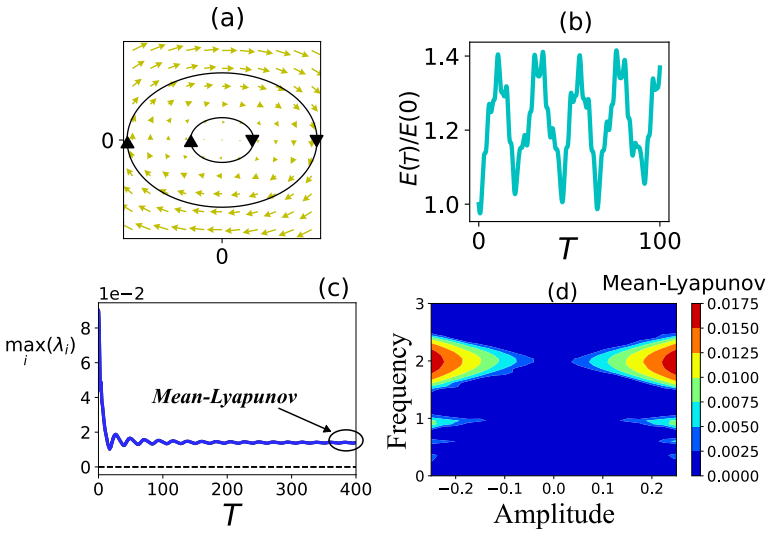

Figure 5.2: (a) Velocity field of a time-independent elliptic flow. (b) Energy of a perturbation that we impose at a time-independent elliptic flow. Notice that it remains bounded and therefore the flow is stable. (c) We let the elliptic flow to vary with time in a cosine way. Shown here is the maximum Lyapunov exponent (corresponding to a perturbation) which converges to some positive value. (d) The value at which the maximum Lyapunov converges as a function of the frequency and amplitude of the modulation.

For instance, we let the shape of the elliptic flow to change in a cosine way with a particular frequency and a particular amplitude, we computed the velocity and the pressure of a perturbation that we imposed at such a time-varying flow and in Fig. 5.2(c) we present the maximum Lyapunov exponent (corresponding to the perturbation). The maximum Lypaunov converges asymptotically to some positive value, meaning that the energy of the perturbation grows exponentially with time. This is a paremetric resonance. In Fig. 5.2(d) we present the value at which the maximum Lyapunov converges (the Mean Lyapunov - see Fig. 5.2(c)) as a function of the frequency and the amplitude of the modulation. We find some regions in the parameter space in which the time-dependent elliptic flow is unstable (these regions actually match with the Arnold tongues of the Mathieu equation). Next thing is to calculate the transient amplifying effects of the stable perturbations of this time-dependent elliptic flow.

To conclude, the study presented in the current thesis revealed the rich phenomenology of wave physics in time and/or space varying media, while the exploration of both classical and quantum systems highlighted the diversity and broad range of applications within wave physics. The world of wave physics never stops amazing us, and novel wave phenomena that continuously emerge only serve to deepen our understanding of the physical world.

Appendix A

Mirror symmetric cells

We give here the analytic derivation of the relations that are given in Eq. (1.21), (1.22), (1.25) and (1.26) in Chapter 1. We remind first that the periodic potential that we considered in that Chapter was build from a mirror symmetric cell. Due to this mirror symmetry, the transfer matrix of this cell (that is the transfer matrix $\mathbf{M}$ that is given in Eq. (1.2)) is decomposed around its center of symmetry as $\mathbf{M} = \mathbf{M}_2\mathbf{M}_1$ with $\mathbf{M}_2^{-1} = \mathbf{P}\mathbf{M}_1\mathbf{P}$ and $\mathbf{P} = \begin{pmatrix} 0 & 1 \\ 1 & 0 \end{pmatrix}$ is the parity operator. Therefore if we set $\mathbf{M}_1 = \begin{pmatrix} \alpha & \beta \\ \beta^* & \alpha^* \end{pmatrix}$ then $\mathbf{M}_2^{-1} = \begin{pmatrix} \alpha^* & \beta^* \\ \beta & \alpha \end{pmatrix}$. We will use this decomposition in both of the following proofs.

A.1 Centers of the cells

We begin by giving the derivation of the relations that are given in Eq. (1.21) and (1.22). To start we remind that we have denoted the centers of the mirror symmetric cells as a_m with $m = 1, 2, ..., N$.

We denote as $\boldsymbol{\varphi}$ the vector that contains the right and left going waves at each point. For instance, at $x = -D/2$ (left edge of the setup, see Fig. 1.1(b) of the main text), since there is no reflected wave it holds

$$\boldsymbol{\varphi}(-D/2) = \begin{pmatrix} 1 \\ 0 \end{pmatrix} \tag{A.1}$$

The wave function is the sum of the two components of the vector $\boldsymbol{\varphi}$, and therefore at $x = -D/2$ it holds

$$\psi(-D/2) = 1. \tag{A.2}$$

Next, we calculate the vector $\boldsymbol{\varphi}$ at $x = D/2$ (right edge of the setup) using the Chebychev identity.

The Chebyshev identity states that if the transfer matrix $\mathbf{M}$ is written in the form

$$\mathbf{M} = \begin{pmatrix} m_{11} & m_{12} \\ m_{21} & m_{22} \end{pmatrix} \tag{A.3}$$

then the matrix $(\mathbf{M})^N$ is given by

$$(\mathbf{M})^N = \begin{pmatrix} m_{11}U_{N-1} - U_{N-2} & m_{12}U_{N-1} \\ m_{12}U_{N-1} & m_{22}U_{N-1} - U_{N-2} \end{pmatrix} \tag{A.4}$$

where

$$U_N = \frac{\sin((N+1)\phi)}{\sin(\phi)}. \tag{A.5}$$

where ϕ is the Bloch phase and it is equal to $n\pi/N$ at the n^{th} PTR. Therefore, for the PTR number n it holds

$$\boldsymbol{\varphi}(D/2) = \begin{pmatrix} (-1)^n \\ 0 \end{pmatrix} \tag{A.6}$$

and the wave function there is equal to

$$\psi(D/2) = (-1)^n. \tag{A.7}$$

Now, we calculate the vector $\boldsymbol{\phi}$ at the centers of the first and last cells, namely at the positions a_1 and a_N. At $x = a_1$ we get

$$\boldsymbol{\varphi}(a_1) = \mathbf{M}_1\boldsymbol{\varphi}(-D/2) = \begin{pmatrix} \alpha \\ \beta^* \end{pmatrix} \tag{A.8}$$

meaning that the wave function there is equal to

$$\psi(a_1) = \alpha + \beta^*. \tag{A.9}$$

Similarly, at the the centers of the center of the last cell, $x = a_1$, it holds

$$\boldsymbol{\varphi}(a_N) = \mathbf{M}_2^{-1}\boldsymbol{\varphi}(D/2) = \begin{pmatrix} (-1)^n\alpha^* \\ (-1)^n\beta \end{pmatrix} \tag{A.10}$$

and therefore the wave function there is equal to

$$\psi(a_N) = (-1)^n(\alpha^* + \beta). \tag{A.11}$$

For the next step, it is necessary to define a new transfer matrix. We define the matrix $\tilde{\mathbf{M}} = \mathbf{M}_1\mathbf{M}_2$. Notice that this matrix differs from the matrix $\mathbf{M}$ which is equal to $\mathbf{M} = \mathbf{M}_2\mathbf{M}_1$.

We denote the two eigenvectors of the matrix $\tilde{\mathbf{M}}$ as $\boldsymbol{v}_q$ and $\boldsymbol{v}_{-q}$. The determinant of $\tilde{\mathbf{M}}$ is equal to 1 and therefore its eigenvectors are written in the form

$$\boldsymbol{v}_q = \frac{1}{\sqrt{1+|\kappa|^2}} \begin{pmatrix} 1 \\ \kappa \end{pmatrix} \qquad \boldsymbol{v}_{-q} = \frac{1}{\sqrt{1+|\kappa|^2}} \begin{pmatrix} \kappa^* \\ 1 \end{pmatrix}. \tag{A.12}$$

We use the vectors $\boldsymbol{v}_q$ and $\boldsymbol{v}_{-q}$ as a basis and we write the vector $\boldsymbol{\varphi}(a_1)$, i.e., at the center of the first cell, as

$$\boldsymbol{\varphi}(a_1) = A\boldsymbol{v}_q + B\boldsymbol{v}_{-q}, \tag{A.13}$$

where A and B are coefficients that are calculated by the boundary conditions. The wave function at $x = a_1$ is written as

$$\psi(a_1) = Az + Bz^* \tag{A.14}$$

with $z = \dfrac{1+\kappa}{\sqrt{1+|\kappa|^2}}$.

The wave function at the center a_m is calculated by acting with the transfer matrix $\tilde{\mathbf{M}}^{m-1}$ at the vector $\boldsymbol{\varphi}(a_1)$,

$$\boldsymbol{\varphi}(a_m) = Ae^{i(m-1)\phi_n}\boldsymbol{v}_q + Be^{-i(m-1)\phi_n}\boldsymbol{v}_{-q} \tag{A.15}$$

and therefore for the wave function at $x = a_m$ we get

$$\psi(a_m) = Ae^{i(m-1)\phi_n}z + Be^{-i(m-1)\phi_n}z^*. \tag{A.16}$$

The coefficients A and B are found from the boundary conditions that are given in Eq. (A.9) and (A.11). These result to,

$$A = \frac{we^{-i(N-1)\phi_n} - w^*(-1)^n}{z\left(e^{-i(N-1)\phi_n} - e^{i(N-1)\phi_n}\right)} \tag{A.17}$$

and

$$B = \frac{(-1)^n w^* - we^{i(N-1)\phi_n}}{z^*\left(e^{-i(N-1)\phi_n} - e^{i(N-1)\phi_n}\right)} \tag{A.18}$$

where $w = \alpha + \beta^*$.

If we plug the coefficients A and B at the expression that is given in Eq. (A.16), then we get that the wave function at the center a_m is given by

$$\psi(a_m) = \frac{1}{\sin[(N-1)\phi_n]}\{[w_R\sin[(N-m)\phi_n] + (-1)^n w_R\sin[(m-1)\phi_n]] + \\ +i\left[w_I\sin[(N-m)\phi_n] - (-1)^n w_I\sin[(m-1)\phi_n]\right]\} \tag{A.19}$$

where w_R and w_I are the real and imaginary components of w. Finally, the quantity $\mathrm{Re}[\psi(a_m)]\mathrm{Im}[\psi(a_m)]$

is equal to

$$\mathrm{Re}[\psi(a_m)]\mathrm{Im}[\psi(a_m)] = \frac{w_R w_I}{\sin^2[(N-1)\phi_n]} \times \left\{\sin^2[(N-m)\phi_n] - \sin^2[(m-1)\phi_n]\right\} \tag{A.20}$$

which is Eq. (1.21) of the main text.

As we mentioned in the main text, Eq. (A.20) proves that if we place Dirac scatterers at the centers of the cells, then the PTRs are always preserved in pairs. To see this clearly, notice that from Eq. (A.20) we get the following relation

$$\mathrm{Re}[\psi_{0,n}(a_m)]\mathrm{Im}[\psi_{0,n}(a_m)] = \frac{f(\phi_n)}{f(\phi_{N-n}}\mathrm{Re}[\psi_{0,N-n}(a_m)]\mathrm{Im}[\psi_{0,N-n}(a_m)] \tag{A.21}$$

If the PTR number n is preserved after the addition of Dirac scatterers, then the imaginary part of $k_{1,n}$ is zero, which means (recall Eq. (1.19) of the main text) that

$$\sum_{m=1}^{N} c_m \mathrm{Re}[\psi_{0,n}(w_m)]\mathrm{Im}[\psi_{0,n}(w_m)] = 0. \tag{A.22}$$

Using, Eq. (A.22) we immediately get that $\mathrm{Im}[k_{1,N-n}]$ is also zero and therefore the PTR number $N-n$ is preserved as well.

A.2 Edges of the cells

The derivation of the relations that are given in Eq. (1.25) and (1.26) in Chapter 1 is similar to the previous proof. First, we remind that we have denoted the edges of the cells as b_m and notice that the index m this time gets the values: $m = 0, 1, 2, ..., N$.

For this proof we will make use of the transfer matrix $\mathbf{M} = \mathbf{M_2}\mathbf{M_1} = \begin{pmatrix} m_{11} & m_{12} \\ m_{21} & m_{22} \end{pmatrix}$. We denote the two eigenvectors of this transfer matrix as

$$\boldsymbol{u}_q = \frac{1}{\sqrt{1+|\lambda|^2}} \begin{pmatrix} 1 \\ \lambda \end{pmatrix} \qquad \boldsymbol{u}_{-q} = \frac{1}{\sqrt{1+|\lambda|^2}} \begin{pmatrix} \lambda^* \\ 1 \end{pmatrix}. \tag{A.23}$$

We stress here that due to the mirror symmetry of the cells, the parameter λ is real, i.e., $\lambda = \lambda^*$. Even if we did not write it in the previous proof – in Appendix A.1 – this holds for the parameter κ as well (see Eq. (A.12), the definition of the eigenvectors of the $\tilde{\mathbf{M}}$ matrix).

We write now the vector $\boldsymbol{\varphi}(-D/2) = \boldsymbol{\varphi}(b_0)$ (see Appendix A.1) using as a basis the vectors ϕ_q and ϕ_{-q}

$$\boldsymbol{\varphi}(b_0) = C_1 \frac{1}{\sqrt{1+|\lambda|^2}} \begin{pmatrix} 1 \\ \lambda \end{pmatrix} + C_2 \frac{1}{\sqrt{1+|\lambda|^2}} \begin{pmatrix} \lambda \\ 1 \end{pmatrix} \tag{A.24}$$

The coefficients C_1 and C_2 are found from the fact that the analysis refers to PTRs, namely

$$\boldsymbol{\varphi}(-D/2) = \begin{pmatrix} 1 \\ 0 \end{pmatrix}, \tag{A.25}$$

and we get that

$$\boldsymbol{\varphi}(b_0) = \frac{1}{1-\lambda^2}\begin{pmatrix} 1 \\ \lambda \end{pmatrix} - \frac{1}{1-\lambda^2}\begin{pmatrix} \lambda \\ 1 \end{pmatrix}. \tag{A.26}$$

We can now calculate the vector $\boldsymbol{\varphi}$ at each point b_m, if we act with the transfer matrix $\mathbf{M}^m$. Therefore, we get

$$\boldsymbol{\varphi}(b_m) = e^{im\phi_n}\frac{1}{1-\lambda^2}\begin{pmatrix} 1 \\ \lambda \end{pmatrix} - e^{-im\phi_n}\frac{1}{1-\lambda^2}\begin{pmatrix} \lambda \\ 1 \end{pmatrix} \tag{A.27}$$

where again $\phi_n = n\pi/N$ is the Bloch phase of the n^{th} PTR. The sum of the two components of the vector $\boldsymbol{\varphi}(b_m)$ is the wave function $\psi(b_m)$ and therefore it is equal to

$$\psi(b_m) = \frac{1}{1-\lambda}\left[e^{im\phi_n} - \lambda e^{-im\phi_n}\right]. \tag{A.28}$$

Finally, for the quantity $\mathrm{Re}[\psi(b_m)]\mathrm{Im}[\psi(b_m)]$, which is of interest in the preservation of the PTRs, we get

$$\mathrm{Re}[\psi(b_m)]\mathrm{Im}[\psi(b_m)] = \frac{1}{2}\frac{1+\lambda}{1-\lambda}\sin(2m\phi_n), \tag{A.29}$$

which is Eq. (1.26) of the main text.

Appendix B

Numerical computation of the localization length

We provide here a more detailed discussion regarding the numerical computation of the localization length that we studied Chapter 2. Recall that for this computation, we employed the transfer matrix method and we wrote the displacements of the masses from their equilibrium positions (that is u_n), in the matrix form (see Eq. (2.29))

$$\boldsymbol{A}_{n+1} = \mathbf{T}_n \boldsymbol{A}_n \tag{B.1}$$

where $\boldsymbol{A}_n = \begin{pmatrix} u_n \\ u_{n-1} \end{pmatrix}$. The matrix $\mathbf{T}_n$ is given in Eq. (2.30). Therefore, given an initial vector $\boldsymbol{A}_1$, the behavior of the vector $\boldsymbol{A}_N$ is given from the matrix

$$\mathbf{P}_N = \prod_{i=1}^{N} \mathbf{T}_i \tag{B.2}$$

According to the Oseledec's theorem [126], the matrix

$$\mathbf{B} = \lim_{N\to\infty} \left(\mathbf{P}_N^T \mathbf{P}_N\right)^{1/2N} \tag{B.3}$$

exists and the logarithms of its eigenvalues are the Lyapunov exponents. In our problem, $\mathbf{B}$ is a 2×2 matrix and for its two eigenvalues we found that: $\lambda_1 \approx -\lambda_2$. Therefore, the two Lyapunov exponents satisfy the relation $\gamma_1 \approx -\gamma_2$ as well. The localization length is by definition equal to

$$\Lambda = \frac{1}{\gamma_{min}} \tag{B.4}$$

where γ_{min} is the minimum positive Lyapunov exponent, and therefore in the under study problem we get that $\Lambda = 1/\gamma_1$ since only one exponent is positive (the γ_1).

For chains of large size (large N) we encountered rounding errors when we computed the Lyapunov exponents from the eigenvalues of the matrix $\mathbf{B}$ that is given in Eq. (B.3). To overcome these rounding errors we followed ref. [142] and we normalized the vector $\boldsymbol{A}_n$ at the previous step of each iteration. Specifically: By definition, the maximum Lyapunov exponent (which is γ_1 is our problem as well) is given by

$$\gamma_1 = \frac{1}{N} \ln \left(||\boldsymbol{A}_N|| \right) \tag{B.5}$$

where $||.||$ denotes the Euclidean norm. By using an initial vector $\boldsymbol{A}_1$ with norm 1, from Eq. (B.5) we get that

$$\gamma_1 = \frac{1}{N} \ln \left(\frac{||\boldsymbol{A}_N||}{||\boldsymbol{A}_{N-1}||} \frac{||\boldsymbol{A}_{N-1}||}{||\boldsymbol{A}_{N-2}||} \cdots \frac{||\boldsymbol{A}_3||}{||\boldsymbol{A}_3||} \frac{||\boldsymbol{A}_2||}{||\boldsymbol{A}_1||} \right) \tag{B.6}$$

At each step of iteration, we normalize the vector $\boldsymbol{A}_n$ with its norm at the previous step of the iteration, defining thus the vector

$$\boldsymbol{A}'_n = \frac{\boldsymbol{A}_n}{||\boldsymbol{A}_{n-1}||} \tag{B.7}$$

Then from Eq. (B.6) we get that the Lyapunov exponent γ_1 is given by

$$\gamma_1 = \frac{1}{N} S_N \tag{B.8}$$

where $S_{N+1} = S_N + \ln \left(||\boldsymbol{A}'_{N+1}|| \right)$.

Appendix C

Adiabatic state transfer

We prove here that if the couplings of the time-varying chain that we considered in Chapter 3 vary slowly with time, then the initial edge mode is perfectly transferred across the chain, without being amplified. To prove this we use the WKB method [118].

Let $q_1, q_2, ..., q_N$ be the displacements of all masses from their equilibrium positions and $\dot{q}_1, \dot{q}_2, ..., \dot{q}_N$ the corresponding velocities. Dot represents derivative with respect to time. Then the equations of motion can all be written in the form

$$\dot{\boldsymbol{W}} = \mathbf{A}\boldsymbol{W} \tag{C.1}$$

where

$$\boldsymbol{W} = \begin{pmatrix} q_1 & \cdots & q_N & \dot{q}_1 & \cdots & \dot{q}_N \end{pmatrix}^T \tag{C.2}$$

and

$$\mathbf{A} = \begin{pmatrix} 0 & 0 & \cdots & 0 & 0 & 1\ 0 & \cdots & 0 \\ 0 & 0 & \cdots & 0 & 0 & 0\ 1 & \cdots & 0 \\ & & \ddots & & & & \ddots & \\ 0 & 0 & \cdots & 0 & 0 & 0\ 0 & \cdots & 1 \\ & & & & & & & \\ -\kappa_1-\kappa_2 & \kappa_2 & 0 & \cdots & 0 & 0\ 0 & \cdots & 0 \\ \kappa_2 & -\kappa_1-\kappa_2 & \kappa_1 & \cdots & 0 & 0\ 0 & \cdots & 0 \\ & & \ddots & & & & \ddots & \\ & & & & & & \ddots & \\ 0 & \cdots & \kappa_2 & -\kappa_1-\kappa_2 & \kappa_1 & & \ddots & \\ 0 & 0 & \cdots & \kappa_1 & -\kappa_1-\kappa_2 & & \ddots & \end{pmatrix} \tag{C.3}$$

where the superscript ^{T} stands for the transpose and $\kappa_{1,2}$ are the couplings of the chain that vary with time (without loss of generality we set the values of the masses of the chain at $m = 1$).

We assume that the couplings vary slowly with time, namely $\kappa_{1,2} = \kappa_{1,2}(\epsilon t)$ with $\epsilon << 1$. We introduce the slow time scale $\tau = \epsilon t$ and then Eq. (C.1) gets the form

$$\epsilon \frac{d\boldsymbol{W}}{d\tau} = \mathbf{A}(\tau)\boldsymbol{W}. \tag{C.4}$$

In order to solve Eq. (C.4), we apply the WKB method. Namely, we use as an ansatz the vector

$$\boldsymbol{W}(\tau) = e^{\frac{i}{\epsilon}S(\tau)}\left(\boldsymbol{W}_0(\tau) + \epsilon\boldsymbol{W}_1(\tau) + \epsilon^2\boldsymbol{W}_2(\tau) + ...\right). \tag{C.5}$$

Plugging this ansatz into Eq. (C.4) and collecting powers of ϵ we get

$$O(1): \quad i\frac{dS(\tau)}{d\tau}\boldsymbol{W}_0(\tau) = \mathbf{A}(\tau)\boldsymbol{W}_0(\tau) \tag{C.6}$$

$$O(\epsilon): \quad i\frac{dS(\tau)}{d\tau}\boldsymbol{W}_1(\tau) + \frac{d\boldsymbol{W}_0(\tau)}{d\tau} = \mathbf{A}(\tau)\boldsymbol{W}_1(\tau) \tag{C.7}$$

From Eq. (C.6) we get that $idS/s\tau$ is one of the eigenevalues of the matrix $\mathbf{A}(\tau)$ and that $\boldsymbol{W}_0(\tau)$ is proportional to the associated eigenvector. It remains to find the proportionality factor. This factor is found as follows: We act with some vector $\boldsymbol{Y}^\dagger$ at Eq. (C.7) († stands for the complex congugate transpose)

$$\boldsymbol{Y}^\dagger\left(\mathbf{A}(\tau) - i\frac{dS(\tau)}{d\tau}\right)\boldsymbol{W}_1 = \boldsymbol{Y}^\dagger\frac{d\boldsymbol{W}_0}{d\tau} \tag{C.8}$$

which is also written as

$$\left[\left(\mathbf{A}(\tau) - i\frac{dS(\tau)}{d\tau}\mathbf{I}\right)^\dagger\boldsymbol{Y}\right]^\dagger\boldsymbol{W}_1 = \boldsymbol{Y}^\dagger\frac{d\boldsymbol{W}_0}{d\tau}. \tag{C.9}$$

We choose $\boldsymbol{Y}$ to be on the kernel of the matrix $\mathbf{B}(\tau) = \left(\mathbf{A}(\tau) - i\frac{dS(\tau)}{d\tau}\mathbf{I}\right)^\dagger$. Then from Eq. (C.9) we get that $\boldsymbol{Y}$ and $d\boldsymbol{W_0}/d\tau$ are orthogonal. From this orthogonality condition, we find the corresponding proportional factor.

Next, we show how to apply this, at the eigenvector of the matrix $\mathbf{A}(\tau)$ that corresponds to the edge mode. First of all, notice that the matrix $\mathbf{A}(\tau)$ has an eigenvalue that is equal to

$$\tilde{\lambda}(\tau) = i\sqrt{\kappa_1(\tau) + \kappa_2(\tau)} = i\tilde{\omega}(\tau). \tag{C.10}$$

This eigenvalue corresponds to the edge mode. The associated eigenvector to this eigenvalue is

$$\tilde{\boldsymbol{u}}(\tau) = \begin{pmatrix} (-1)^{\frac{N-1}{2}} r^{\frac{N-1}{2}} \\ 0 \\ \vdots \\ -r \\ 0 \\ 1 \\ i(-1)^{\frac{N-1}{2}} \tilde{\omega} r^{\frac{N-1}{2}} \\ 0 \\ \vdots \\ -i\tilde{\omega} r \\ 0 \\ i\tilde{\omega} \end{pmatrix}, \tag{C.11}$$

where we set $r = r(\tau) = \kappa_1(\tau)/\kappa_2(\tau)$.

The vector $\boldsymbol{W}_0(\tau)$ of the WKB ansatz is written as

$$\boldsymbol{W}_0(\tau) = \tilde{c}(\tau)\tilde{\boldsymbol{u}}(\tau), \tag{C.12}$$

where $\tilde{c}(\tau)$ is the proportional factor. To find this factor we use the orthogonality of the vectors $\boldsymbol{W}_0(\tau)$ and $\boldsymbol{Y}$. The vector $\boldsymbol{Y}$ is found to be the following one

$$\boldsymbol{Y} = \begin{pmatrix} i\tilde{\omega}(-1)^{\frac{N+1}{2}} r^{\frac{N-1}{2}} \\ 0 \\ \vdots \\ i\tilde{\omega} r \\ 0 \\ -i\tilde{\omega} \\ (-1)^{\frac{N-1}{2}} r^{\frac{N-1}{2}} \\ 0 \\ \vdots \\ -r \\ 0 \\ 1 \end{pmatrix}. \tag{C.13}$$

From the orthogonality of the vectors $\boldsymbol{Y}$ and $d\boldsymbol{W_0}/d\tau$ we arrive at the following ODE that the factor $\tilde{c}(\tau)$ satisfies,

$$\frac{1}{\tilde{c}}\frac{d\tilde{c}}{d\tau} = -\frac{\boldsymbol{Y}^\dagger \cdot \dfrac{d\tilde{\boldsymbol{u}}}{d\tau}}{\boldsymbol{Y}^\dagger \cdot \tilde{\boldsymbol{u}}}. \tag{C.14}$$

After a few calculations we find that Eq. (C.14) takes the form

$$\frac{1}{\tilde{c}}\tilde{c}' = -\frac{1}{2}r' \frac{\sum_{i=1,i\ \text{odd}}^{N} (i-1)\, r^{i-2}}{\sum_{i=1,i\ \text{odd}}^{N} r^{i-1}} - \frac{\tilde{\omega}'}{2\tilde{\omega}} \tag{C.15}$$

where prime denotes derivative with respect to τ. Integrating the last equation we get that

$$\tilde{c}(\tau) \sim \frac{1}{\sqrt{\sum_{i=1,i \text{ odd}}^{N} r^{i-1}(\tau)}} \frac{1}{\sqrt{\tilde{\omega}(\tau)}} e^{\frac{i}{\epsilon}\int_0^\tau \tilde{\omega}(s)ds}. \tag{C.16}$$

Therefore, the vector $\boldsymbol{W}(\tau)$ of the WKB ansatz is given by

$$\boldsymbol{W}(\tau) = \frac{C}{\sqrt{\sum_{i=1,i \text{ odd}}^{N} r^{i-1}(\tau)}\sqrt{\tilde{\omega}(\tau)}} e^{\frac{i}{\epsilon}\int_0^\tau \tilde{\omega}(s)ds} \tilde{\boldsymbol{u}}(\tau) + c.c, \tag{C.17}$$

where the constant C is related with the initial conditions. At time $t = 0$ the vector $\boldsymbol{W}$ is given by

$$\boldsymbol{W}(0) = \frac{C}{\sqrt{\sum_{i=1,i \text{ odd}}^{N} r^{i-1}(0)}\sqrt{\tilde{\omega}(0)}} \begin{pmatrix} (-1)^{\frac{N-1}{2}} r^{\frac{N-1}{2}}(0) \\ 0 \\ \vdots \\ -r(0) \\ 0 \\ 1 \\ i\tilde{\omega}(0)(-1)^{\frac{N-1}{2}} r^{\frac{N-1}{2}}(0) \\ 0 \\ \vdots \\ -i\tilde{\omega}(0)r(0) \\ 0 \\ i\tilde{\omega}(0) \end{pmatrix} + c.c, \tag{C.18}$$

At time $t = T$, the couplings are inverted $\kappa_1(T) = \kappa_2(0)$ and $\kappa_2(T) = \kappa_1(0)$. So, $\tilde{\omega}(T) = \tilde{\omega}(0)$ and $r(T) = 1/r(0)$. After a few calculations, we find the vector $\boldsymbol{W}$ at the final time T,

$$\boldsymbol{W}(T) = \frac{C}{\sqrt{\sum_{i=1,i \text{ odd}}^{N} r^{i-1}(0)}} \frac{1}{\sqrt{\tilde{\omega}(0)}} \begin{pmatrix} (-1)^{\frac{N-1}{2}} \\ 0 \\ \vdots \\ -r(0)^{\frac{N-3}{2}} \\ 0 \\ r(0)^{\frac{N-1}{2}} \\ i\tilde{\omega}(0)(-1)^{\frac{N-1}{2}} \\ 0 \\ \vdots \\ -i\tilde{\omega}(0)r(0)^{\frac{N-3}{2}} \\ 0 \\ i\tilde{\omega}(0)r(0)^{\frac{N-1}{2}} \end{pmatrix} e^{\frac{i}{\epsilon}\int_0^{\epsilon T} \tilde{\omega}(s)ds} + c.c. \tag{C.19}$$

We compare the vectors $\boldsymbol{W}(0)$ and $\boldsymbol{W}(T)$ and we find that the initial mode is transferred to the other side of the chain with the same amplitude (it is not amplified).

Appendix D

Approximation and closed form formula

The results that are presented in this appendix provide some insight into the results of Chapter 4. First of all, we show here that under some assumptions we get closed form expressions for the pseudospectra. We also get a closed form formula that provides insight into the plateau that the quantity $(\rho_\epsilon - 1)/\epsilon$ shows in Fig. 4.6(b) (recall that ρ_ϵ is the pseudopectral radius). We begin by reminding that the Floquet theorem states that the propagator matrix $\mathbf{\Phi}(\tau, \tau_0)$ is written as the product of two matrices. The first matrix is a π-periodic one and we denoted this matrix as $\mathbf{P}(\tau, \tau_0)$ in Eq. (4.13) of the main text. The second matrix is the exponential $e^{\mathbf{B}(\tau_0)(\tau-\tau_0)}$.

Our assumption is that we do not take into account the periodic matrix $\mathbf{P}(\tau, \tau_0)$. Namely, we assume that the time evolution is governed only by the exponential $e^{\mathbf{B}(\tau_0)(\tau-\tau_0)}$,

$$\mathbf{\Phi}(\tau, \tau_0) \rightarrow e^{\mathbf{B}(\tau_0)(\tau-\tau_0)}. \tag{D.1}$$

To illustrate this assumption, we present in Fig. D.1(a) and (b) the norms $||\mathbf{\Phi}(\tau, 0)||$ and $||e^{\mathbf{B}(0)\tau}||$ for two different sets (δ, q). In Fig. D.1(a) we used the same set as in Fig. 4.1(b) of the main text - green rectangular, namely $q = 0.5072$ and $\delta = 3q$. We remind that this set of parameters returns a Floquet exponent that is equal to $\gamma = 0.9$. In Fig. D.1(b) the parameter q is equal to 1.2389 and again $\delta = 3q$. This choice results in a Floquet exponent that is equal to $\gamma = 0.1$. From Fig. D.1(b) we get that for $\gamma << 1$, the exponential $e^{\mathbf{B}(\tau_0)(\tau-\tau_0)}$ follows closely the propagator. However, this is not the case for $\gamma \approx 1$ (see Fig. D.1(a)). Yet, in both cases the maximum value of the $||e^{\mathbf{B}(0)\tau}||$, namely the quantity $\max_\tau ||e^{\mathbf{B}(0)\tau}||$, is a lower bound for the corresponding maximum of the propagator.

As we mentioned at the beginning of this appendix, at this point we are interested to get an insight into some results that are illustrated in the main text. For that reason, we will set the initial time τ_0 at zero and we will try to get some information for the quantity $||e^{\mathbf{B}(0)\tau}||$ and not for the general $||e^{\mathbf{B}(\tau_0)(\tau-\tau_0)}||$. As we shall see, this simplification will allow us to obtain closed form expressions. First of all, we note that the matrix $\mathbf{B}(0)$ has zero diagonal elements and is therefore

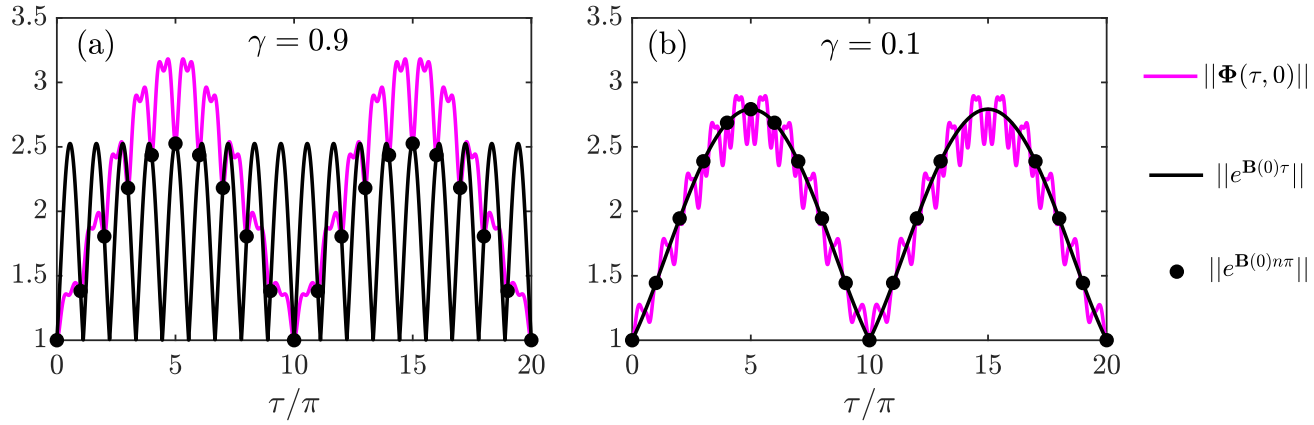

Figure D.1: Shown here are the quantities $||\mathbf{\Phi}(\tau)||$, $||e^{\mathbf{B}(0)\tau}||$ and $||e^{\mathbf{B}n\pi}||$ for two different sets (δ, q). (a) $q = 0.5072$ and $\delta = 3q$ which yields a Floquet exponent $\gamma = 0.9$. (a) $q = 1.2389$ and $\delta = 3q$ which yields a Floquet exponent $\gamma = 0.1$.

written in the form

$$\mathbf{B} = \begin{pmatrix} 0 & a \\ b & 0 \end{pmatrix}. \tag{D.2}$$

This form is due to the symmetry of the matrix $\mathbf{C}(\tau) = \begin{pmatrix} \dot{\omega}/2\omega & \omega \\ -\omega & -\dot{\omega}/2\omega \end{pmatrix}$ in time inversion.

Information regarding the norm $||e^{\mathbf{B}(0)\tau}||$ is provided by the pseudospectrum of the $\mathbf{B}(0)$ matrix. First of all, for a matrix $\mathbf{B}(0)$ with zero diagonal elements, we find that the boundaries of the pseudospectra (which are found from the solution of the equation $||(z - \mathbf{B}(0))^{-1}|| = \epsilon^{-1}$) are given by (we set $z = x + iy$)

$$\begin{cases} y_{1,2} = \sqrt{-ab + \epsilon^2 - x^2 \pm \sqrt{\epsilon^2(a-b)^2 + 4abx^2}}, \ y > 0 \\ y_{3,4} = -\sqrt{-ab + \epsilon^2 - x^2 \pm \sqrt{\epsilon^2(a-b)^2 + 4abx^2}}, \ y < 0 \end{cases} \tag{D.3}$$

An example of these boundaries is illustrated in Fig. D.2 for three values of ϵ. We used the same set of parameters that we also used in Fig. D.1(a). The elements a and b of the $\mathbf{B}(0)$ are found numerically. Notice that these boundaries have the same form as the ones that are shown in Fig. 4.5(a) in Chapter 4.

The pseudospectrum of the $\mathbf{B}(0)$ matrix provides bounds for the $\max_{\tau} ||e^{\mathbf{B}(0)\tau}||$. A lower bound for this quantity is given by the continuous Kreiss constant. More precisely, the following relation holds

$$\max_{\tau} ||e^{\mathbf{B}(0)\tau}|| \geq \max_{\epsilon} [\alpha_\epsilon(\mathbf{B})/\epsilon] \tag{D.4}$$

where α_ϵ is the pseudospectral abscissa - the maximum of the real part of the pseudospectra of

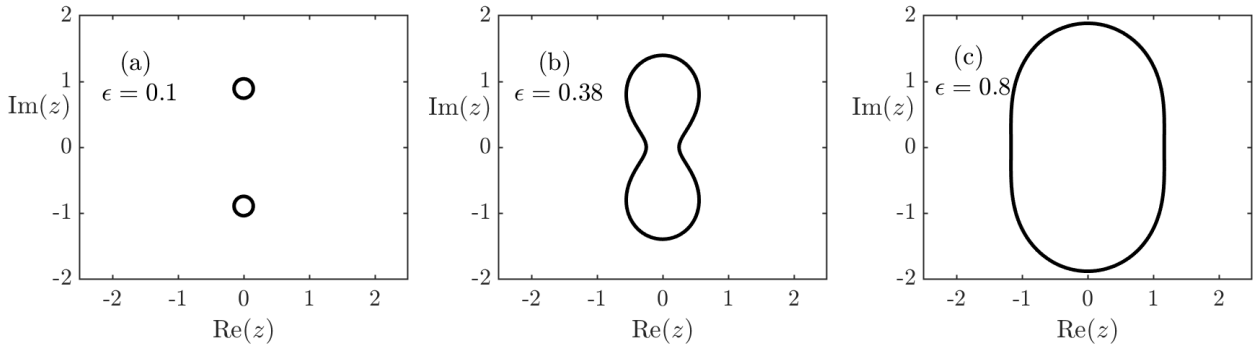

Figure D.2: Shown are the curves $y_{1,2,3,4}$ for the set of parameters (δ, q) that we also used in Fig. D.1(a) and for (a) $\epsilon = 0.01$, (b) $\epsilon = 0.038$ and (c) $\epsilon = 0.08$.

the $\mathbf{B}(0)$ matrix. The quantity that is given at the right hand side of Eq. (C.4) is called the continuous Kreiss constant. Using the curves $y_{1,2,3,4}$ that are given in Eq. (C.3), we can calculate the pseudospectral abscissa. The result is

$$\begin{cases} \alpha_\epsilon = \dfrac{\epsilon|a-b|}{2\sqrt{|ab|}} & \text{for } \epsilon < \dfrac{2|ab|}{|a+b|} \\ \alpha_\epsilon = \sqrt{\epsilon^2 - |ab| + \epsilon|a+b|} & \text{otherwise} \end{cases} \tag{D.5}$$

In Fig. D.3 we present the quantity $\alpha_\epsilon(\mathbf{B})/\epsilon$ as a function of ϵ. Notice that the quantity α_ϵ/ϵ is constant up to a value of ϵ (that is equal to $\tilde{\epsilon} = 2|ab|/|a+b|$) and after that it drops. Therefore, this quantity shows a plateau for small values of ϵ as it was the case in Fig. 4.6(b) in Chapter 4.

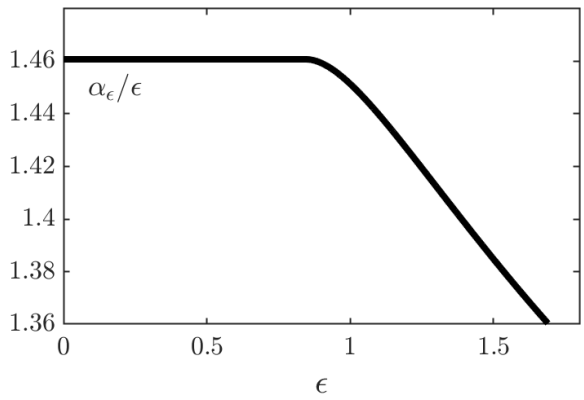

Figure D.3: Once more, we used the set of parameters (δ, q) that we also used in Fig. D.1(a). Shown here is the quantity $\alpha_\epsilon(\mathbf{B})/\epsilon$ as a function of ϵ. The $\max_\epsilon [\alpha_\epsilon(\mathbf{B})/\epsilon]$ is the continuous Kreiss constant and is a bound for the $\max_\tau ||e^{\mathbf{B}(0)\tau}||$.

Bibliography

[1] L. N. Brillouin, *Wave Propagation in Periodic Structures: Electric Filters and Crystal Lattices*. Dover Publications, 1953.

[2] D. Sprung, H. Wu, and J. Martorell, "Scattering by a finite periodic potential," *American Journal of Physics*, vol. 61, p. 1118, 1993.

[3] N. W. Ashcroft and N. D. Mermin, *Solid State Physics*. Holt, Rinehardt and Winston, New York, 1976.

[4] D. J. Griffiths and N. F. Taussig, "Scattering from a locally periodic potential," *American Journal of Physics*, vol. 60, p. 883, 1992.

[5] D. J. Griffiths and C. A. Steinke, "Waves in locally periodic media," *American Journal of Physics*, vol. 69, p. 137, 2001.

[6] P. Markos and C. M. Soukoulis, *Wave propagation: From Electrons to Photonic Crystals and Left-Handed Materials*. Princeton University Press, 2008.

[7] F. Barra and P. Gaspard, "Scattering in periodic systems: from resonances to band structure," *Journal of Physics A: Mathematical and General*, vol. 32, p. 3357, 1999.

[8] X. Huang, Y. Wang, and C. Gong, "Numerical investigation of light-wave localization in optical Fibonacci superlattices with symmetric internal structure," *Journal of Physics: Condensed Matter*, vol. 11, p. 7645, 1999.

[9] X. Huang, S. Jiang, R. Peng, and A. Hu, "Perfect transmission and self-similar optical transmission spectra in symmetric Fibonacci-class multilayers," *Physical Review B*, vol. 63, p. 245104, 2001.

[10] R. Peng, X. Huang, F. Qiu, M. Wang, A. Hu, S. Jiang, and M. Mazzer, "Symmetry-induced perfect transmission of light waves in quasiperiodic dielectric multilayers," *Applied Physics Letters*, vol. 80, p. 3063, 2002.

[11] P. Mauriz, M. S. d. Vasconcelos, and E. L. d. Albuquerque, "Optical transmission spectra in symmetrical Fibonacci photonic multilayers," *Physics Letters A*, vol. 373, p. 496, 2009.

[12] S. V. Zhukovsky, "Perfect transmission and highly asymmetric light localization in photonic multilayers," *Physical Review A*, vol. 81, p. 053808, 2010.

[13] R. Nava, J. Tagüeña-Martínez, J. Del Rio, and G. Naumis, "Perfect light transmission in fibonacci arrays of dielectric multilayers," *Journal of Physics: Condensed Matter*, vol. 21, no. 15, p. 155901, 2009.

[14] P. Kalozoumis, C. Morfonios, F. Diakonos, and P. Schmelcher, "Local symmetries in one-dimensional quantum scattering," *Physical Review A*, vol. 87, p. 032113, 2013.

[15] Y. Lu, R. Peng, Z. Wang, Z. Tang, X. Huang, M. Wang, Y. Qiu, A. Hu, S. Jiang, and D. Feng, "Resonant transmission of light waves in dielectric heterostructures," *Journal of Applied Physics*, vol. 97, 2005.

[16] V. Grigoriev and F. Biancalana, "Bistability, multistability and non-reciprocal light propagation in thue–morse multilayered structures," *New Journal of Physics*, vol. 12, p. 053041, 2010.

[17] P. Kalozoumis, C. Morfonios, N. Palaiodimopoulos, F. Diakonos, and P. Schmelcher, "Local symmetries and perfect transmission in aperiodic photonic multilayers," *Physical Review A*, vol. 88, p. 033857, 2013.

[18] L. L. Sánchez-Soto, J. J. Monzón, A. G. Barriuso, and J. F. Cariñena, "The transfer matrix: A geometrical perspective," *Physics Reports*, vol. 513, p. 191, 2012.

[19] N. Cooper, J. Dalibard, and I. Spielman, "Topological bands for ultracold atoms," *Reviews of Modern Physics*, vol. 91, p. 015005, 2019.

[20] J. K. Asbóth, L. Oroszlány, and A. Pályi, *A short course on topological insulators*. Springer, 2016.

[21] M. V. Berry, "Quantal phase factors accompanying adiabatic changes," *Proceedings of the Royal Society of London. A. Mathematical and Physical Sciences*, vol. 392, p. 45, 1984.

[22] D. Xiao, M.-C. Chang, and Q. Niu, "Berry phase effects on electronic properties," *Reviews of Modern Physics*, vol. 82, p. 1959, 2010.

[23] M. Z. Hasan and C. L. Kane, "Colloquium: Topological insulators," *Reviews of Modern Physics*, vol. 82, no. 4, p. 3045, 2010.

[24] X.-L. Qi and S.-C. Zhang, "Topological insulators and superconductors," *Reviews of Modern Physics*, vol. 83, no. 4, p. 1057, 2011.

[25] E. Prodan and H. Schulz-Baldes, *Bulk and boundary invariants for complex topological insulators*. Springer, 2016.

[26] K. v. Klitzing, G. Dorda, and M. Pepper, "New method for high-accuracy determination of the fine-structure constant based on quantized Hall resistance," *Physical Review Letters*, vol. 45, p. 494, 1980.

[27] R. Süsstrunk and S. D. Huber, "Observation of phononic helical edge states in a mechanical topological insulator," *Science*, vol. 349, p. 47, 2015.

[28] R. Süsstrunk and S. D. Huber, "Classification of topological phonons in linear mechanical metamaterials," *Proceedings of the National Academy of Sciences*, vol. 113, p. E4767, 2016.

[29] L. M. Nash, D. Kleckner, A. Read, V. Vitelli, A. M. Turner, and W. T. Irvine, "Topological mechanics of gyroscopic metamaterials," *Proceedings of the National Academy of Sciences*, vol. 112, p. 14495, 2015.

[30] J. Vila, R. K. Pal, and M. Ruzzene, "Observation of topological valley modes in an elastic hexagonal lattice," *Physical Review B*, vol. 96, p. 134307, 2017.

[31] H. Chen, H. Nassar, A. N. Norris, G. Hu, and G. Huang, "Elastic quantum spin Hall effect in kagome lattices," *Physical Review B*, vol. 98, p. 094302, 2018.

[32] L. Xin, Y. Siyuan, L. Harry, L. Minghui, and C. Yanfeng, "Topological mechanical metamaterials: A brief review," *Current Opinion in Solid State and Materials Science*, vol. 24, p. 100853, 2020.

[33] Z. Yang, F. Gao, X. Shi, X. Lin, Z. Gao, Y. Chong, and B. Zhang, "Topological acoustics," *Physical Review Letters*, vol. 114, p. 114301, 2015.

[34] C. He, X. Ni, H. Ge, X.-C. Sun, Y.-B. Chen, M.-H. Lu, X.-P. Liu, and Y.-F. Chen, "Acoustic topological insulator and robust one-way sound transport," *Nature Physics*, vol. 12, p. 1124, 2016.

[35] G. Ma, M. Xiao, and C. T. Chan, "Topological phases in acoustic and mechanical systems," *Nature Reviews Physics*, vol. 1, p. 281, 2019.

[36] A. Coutant, A. Sivadon, L. Zheng, V. Achilleos, O. Richoux, G. Theocharis, and V. Pagneux, "Acoustic Su-Schrieffer-Heeger lattice: Direct mapping of acoustic waveguides to the Su-Schrieffer-Heeger model," *Physical Review B*, vol. 103, p. 224309, 2021.

[37] A. Coutant, V. Achilleos, O. Richoux, G. Theocharis, and V. Pagneux, "Topological two-dimensional Su-Schrieffer-Heeger analog acoustic networks: Total reflection at corners and corner induced modes," *Journal of Applied Physics*, vol. 129, 2021.

[38] A. Coutant, V. Achilleos, O. Richoux, G. Theocharis, and V. Pagneux, "Subwavelength Su-Schrieffer-Heeger topological modes in acoustic waveguides," *The Journal of the Acoustical Society of America*, vol. 151, p. 3626, 2022.

[39] Z. Wang, Y. Chong, J. D. Joannopoulos, and M. Soljačić, "Observation of unidirectional backscattering-immune topological electromagnetic states," *Nature*, vol. 461, p. 772, 2009.

[40] T. Ozawa, H. M. Price, A. Amo, N. Goldman, M. Hafezi, L. Lu, M. C. Rechtsman, D. Schuster, J. Simon, O. Zilberberg, and I. Carusotto, "Topological photonics," *Reviews of Modern Physics*, vol. 91, p. 015006, 2019.

[41] L. Lu, J. D. Joannopoulos, and M. Soljačić, "Topological photonics," *Nature Photonics*, vol. 8, p. 821, 2014.

[42] M. Hafezi, S. Mittal, J. Fan, A. Migdall, and J. Taylor, "Imaging topological edge states in silicon photonics," *Nature Photonics*, vol. 7, p. 1001, 2013.

[43] T. Ma and G. Shvets, "All-si valley-hall photonic topological insulator," *New Journal of Physics*, vol. 18, p. 025012, 2016.

[44] A. B. Khanikaev, S. Hossein Mousavi, W.-K. Tse, M. Kargarian, A. H. MacDonald, and G. Shvets, "Photonic topological insulators," *Nature Materials*, vol. 12, p. 233, 2013.

[45] P. Delplace, J. Marston, and A. Venaille, "Topological origin of equatorial waves," *Science*, vol. 358, p. 1075, 2017.

[46] N. Perez, P. Delplace, and A. Venaille, "Unidirectional modes induced by nontraditional Coriolis force in stratified fluids," *Physical Review Letters*, vol. 128, p. 184501, 2022.

[47] A. Venaille and P. Delplace, "Wave topology brought to the coast," *Physical Review Research*, vol. 3, p. 043002, 2021.

[48] A. Lagendijk, B. v. Tiggelen, and D. S. Wiersma, "Fifty years of Anderson localization," *Physics Today*, vol. 62, p. 24, 2009.

[49] P. W. Anderson, "Absence of diffusion in certain random lattices," *Physical Review*, vol. 109, p. 1492, 1958.

[50] J. Li, R.-L. Chu, J. K. Jain, and S.-Q. Shen, "Topological Anderson Insulator," *Physical Review Letters*, vol. 102, p. 136806, 2009.

[51] H. Jiang, L. Wang, Q.-f. Sun, and X. Xie, "Numerical study of the topological Anderson insulator in HgTe/CdTe quantum wells," *Physical Review B*, vol. 80, p. 165316, 2009.

[52] C. Groth, M. Wimmer, A. Akhmerov, J. Tworzydło, and C. Beenakker, "Theory of the topological Anderson insulator," *Physical Review Letters*, vol. 103, no. 19, p. 196805, 2009.

[53] H.-M. Guo, G. Rosenberg, G. Refael, and M. Franz, "Topological Anderson insulator in three dimensions," *Physical Review Letters*, vol. 105, p. 216601, 2010.

[54] J. Song and E. Prodan, "AIII and BDI topological systems at strong disorder," *Physical Review B*, vol. 89, p. 224203, 2014.

[55] I. Mondragon-Shem, T. L. Hughes, J. Song, and E. Prodan, "Topological criticality in the chiral-symmetric AIII class at strong disorder," *Physical Review Letters*, vol. 113, p. 046802, 2014.

[56] A. Altland, D. Bagrets, L. Fritz, A. Kamenev, and H. Schmiedt, "Quantum criticality of quasi-one-dimensional topological Anderson insulators," *Physical Review Letters*, vol. 112, p. 206602, 2014.

[57] F. Zangeneh-Nejad and R. Fleury, "Disorder-induced signal filtering with topological metamaterials," *Advanced Materials*, vol. 32, p. 2001034, 2020.

[58] S. Stützer, Y. Plotnik, Y. Lumer, P. Titum, N. H. Lindner, M. Segev, M. C. Rechtsman, and A. Szameit, "Photonic topological Anderson insulators," *Nature*, vol. 560, p. 461, 2018.

[59] E. J. Meier, F. A. An, A. Dauphin, M. Maffei, P. Massignan, T. L. Hughes, and B. Gadway, "Observation of the topological Anderson insulator in disordered atomic wires," *Science*, vol. 362, p. 929, 2018.

[60] C. H. Bennett and S. J. Wiesner, "Communication via one-and two-particle operators on Einstein-Podolsky-Rosen states," *Physical Review Letters*, vol. 69, no. 20, p. 2881, 1992.

[61] S. Bose, "Quantum communication through an unmodulated spin chain," *Physical Review Letters*, vol. 91, no. 20, p. 207901, 2003.

[62] S. Bose, "Quantum communication through spin chain dynamics: an introductory overview," *Contemporary Physics*, vol. 48, no. 1, pp. 13–30, 2007.

[63] D. Loss and D. P. DiVincenzo, "Quantum computation with quantum dots," *Physical Review A*, vol. 57, no. 1, p. 120, 1998.

[64] S. Longhi, "Topological pumping of edge states via adiabatic passage," *Physical Review B*, vol. 99, p. 155150, 2019.

[65] F. Mei, G. Chen, L. Tian, S.-L. Zhu, and S. Jia, "Robust quantum state transfer via topological edge states in superconducting qubit chains," *Physical Review A*, vol. 98, p. 012331, 2018.

[66] S. Longhi, G. L. Giorgi, and R. Zambrini, "Landau–Zener topological quantum state transfer," *Advanced Quantum Technologies*, vol. 2, p. 1800090, 2019.

[67] S. Ganeshan, K. Sun, and S. D. Sarma, "Topological zero-energy modes in gapless commensurate Aubry-André-Harper models," *Physical review letters*, vol. 110, p. 180403, 2013.

[68] N. Lang and H. P. Büchler, "Topological networks for quantum communication between distant qubits," *npj Quantum Information*, vol. 3, p. 47, 2017.

[69] D. Thouless, "Quantization of particle transport," *Physical Review B*, vol. 27, p. 6083, 1983.

[70] H.-I. Lu, M. Schemmer, L. M. Aycock, D. Genkina, S. Sugawa, and I. B. Spielman, "Geometrical pumping with a Bose-Einstein condensate," *Physical Review Letters*, vol. 116, p. 200402, 2016.

[71] S. Nakajima, T. Tomita, S. Taie, T. Ichinose, H. Ozawa, L. Wang, M. Troyer, and Y. Takahashi, "Topological Thouless pumping of ultracold fermions," *Nature Physics*, vol. 12, p. 296, 2016.

[72] M. Lohse, C. Schweizer, O. Zilberberg, M. Aidelsburger, and I. Bloch, "A Thouless quantum pump with ultracold bosonic atoms in an optical superlattice," *Nature Physics*, vol. 12, p. 350, 2016.

[73] M. Lohse, C. Schweizer, H. M. Price, O. Zilberberg, and I. Bloch, "Exploring 4D quantum Hall physics with a 2D topological charge pump," *Nature*, vol. 553, p. 55, 2018.

[74] Y. E. Kraus, Y. Lahini, Z. Ringel, M. Verbin, and O. Zilberberg, "Topological states and adiabatic pumping in quasicrystals," *Physical Review Letters*, vol. 109, p. 106402, 2012.

[75] M. Verbin, O. Zilberberg, Y. Lahini, Y. E. Kraus, and Y. Silberberg, "Topological pumping over a photonic Fibonacci quasicrystal," *Physical Review B*, vol. 91, p. 064201, 2015.

[76] O. Zilberberg, S. Huang, J. Guglielmon, M. Wang, K. P. Chen, Y. E. Kraus, and M. C. Rechtsman, "Photonic topological boundary pumping as a probe of 4D quantum Hall physics," *Nature*, vol. 553, p. 59, 2018.

[77] M. Schroer, M. Kolodrubetz, W. Kindel, M. Sandberg, J. Gao, M. Vissers, D. Pappas, A. Polkovnikov, and K. Lehnert, "Measuring a topological transition in an artificial spin-1/2 system," *Physical Review Letters*, vol. 113, p. 050402, 2014.

[78] W. Ma, L. Zhou, Q. Zhang, M. Li, C. Cheng, J. Geng, X. Rong, F. Shi, J. Gong, and J. Du, "Experimental observation of a generalized Thouless pump with a single spin," *Physical Review Letters*, vol. 120, p. 120501, 2018.

[79] M. Switkes, C. Marcus, K. Campman, and A. Gossard, "An adiabatic quantum electron pump," *Science*, vol. 283, p. 1905, 1999.

[80] M. D. Blumenthal, B. Kaestner, L. Li, S. Giblin, T. Janssen, M. Pepper, D. Anderson, G. Jones, and D. Ritchie, "Gigahertz quantized charge pumping," *Nature Physics*, vol. 3, p. 343, 2007.

[81] M. I. Rosa, R. K. Pal, J. R. Arruda, and M. Ruzzene, "Edge states and topological pumping in spatially modulated elastic lattices," *Physical Review Letters*, vol. 123, p. 034301, 2019.

[82] I. H. Grinberg, M. Lin, C. Harris, W. A. Benalcazar, C. W. Peterson, T. L. Hughes, and G. Bahl, "Robust temporal pumping in a magneto-mechanical topological insulator," *Nature Communications*, vol. 11, p. 974, 2020.

[83] Y. Xia, E. Riva, M. I. Rosa, G. Cazzulani, A. Erturk, F. Braghin, and M. Ruzzene, "Experimental observation of temporal pumping in electromechanical waveguides," *Physical Review Letters*, vol. 126, p. 095501, 2021.

[84] W. Cheng, E. Prodan, and C. Prodan, "Experimental demonstration of dynamic topological pumping across incommensurate bilayered acoustic metamaterials," *Physical Review Letters*, vol. 125, p. 224301, 2020.

[85] E. Torrontegui, S. Ibáñez, S. Martínez-Garaot, M. Modugno, A. del Campo, D. Guéry-Odelin, A. Ruschhaupt, X. Chen, and J. G. Muga, "Shortcuts to adiabaticity," *Advances in Atomic, Molecular, and Optical Physics*, vol. 62, p. 117, 2013.

[86] D. Guéry-Odelin, A. Ruschhaupt, A. Kiely, E. Torrontegui, S. Martínez-Garaot, and J. G. Muga, "Shortcuts to adiabaticity: Concepts, methods, and applications," *Reviews of Modern Physics*, vol. 91, p. 045001, 2019.

[87] M. V. Berry, "Transitionless quantum driving," *Journal of Physics A: Mathematical and Theoretical*, vol. 42, p. 365303, 2009.

[88] M. Demirplak and S. A. Rice, "Adiabatic population transfer with control fields," *The Journal of Physical Chemistry A*, vol. 107, p. 9937, 2003.

[89] M. Demirplak and S. A. Rice, "Assisted adiabatic passage revisited," *The Journal of Physical Chemistry B*, vol. 109, p. 6838, 2005.

[90] M. Demirplak and S. A. Rice, "On the consistency, extremal, and global properties of counterdiabatic fields," *The Journal of Chemical Physics*, vol. 129, 2008.

[91] E. J. Meier, K. Ngan, D. Sels, and B. Gadway, "Counterdiabatic control of transport in a synthetic tight-binding lattice," *Physical Review Research*, vol. 2, p. 043201, 2020.

[92] H. Zhou, Y. Ji, X. Nie, X. Yang, X. Chen, J. Bian, and X. Peng, "Experimental realization of shortcuts to adiabaticity in a nonintegrable spin chain by local counterdiabatic driving," *Physical Review Applied*, vol. 13, p. 044059, 2020.

[93] X. Chen, A. Ruschhaupt, S. Schmidt, A. del Campo, D. Guéry-Odelin, and J. G. Muga, "Fast optimal frictionless atom cooling in harmonic traps: Shortcut to adiabaticity," *Physical Review Letters*, vol. 104, p. 063002, 2010.

[94] X. Chen and J. G. Muga, "Transient energy excitation in shortcuts to adiabaticity for the time-dependent harmonic oscillator," *Physical Review A*, vol. 82, p. 053403, 2010.

[95] J. Werschnik and E. Gross, "Quantum optimal control theory," *Journal of Physics B: Atomic, Molecular and Optical Physics*, vol. 40, p. R175, 2007.

[96] F. M. d'Angelis, F. A. Pinheiro, D. Guéry-Odelin, S. Longhi, and F. Impens, "Fast and robust quantum state transfer in a topological su-schrieffer-heeger chain with next-to-nearest-neighbor interactions," *Physical Review Research*, vol. 2, p. 033475, 2020.

[97] N. Palaiodimopoulos, I. Brouzos, F. Diakonos, and G. Theocharis, "Fast and robust quantum state transfer via a topological chain," *Physical Review A*, vol. 103, p. 052409, 2021.

[98] C. Caloz and Z.-L. Deck-Léger, "Spacetime metamaterials—part I: General Concepts," *IEEE Transactions on Antennas and Propagation*, vol. 68, p. 1569, 2019.

[99] E. Galiffi, R. Tirole, S. Yin, H. Li, S. Vezzoli, P. A. Huidobro, M. G. Silveirinha, R. Sapienza, A. Alù, and J. Pendry, "Photonics of time-varying media," *Advanced Photonics*, vol. 4, p. 014002, 2022.

[100] E. Lustig, Y. Sharabi, and M. Segev, "Topological aspects of photonic time crystals," *Optica*, vol. 5, p. 1390, 2018.

[101] Y. Xiao, D. N. Maywar, and G. P. Agrawal, "Reflection and transmission of electromagnetic waves at a temporal boundary," *Optics Letters*, vol. 39, p. 574, 2014.

[102] J. R. Zurita-Sánchez, P. Halevi, and J. C. Cervantes-González, "Reflection and transmission of a wave incident on a slab with a time-periodic dielectric function $\epsilon(t)$," *Physical Review A*, vol. 79, p. 053821, 2009.

[103] V. Bacot, M. Labousse, A. Eddi, M. Fink, and E. Fort, "Time reversal and holography with spacetime transformations," *Nature Physics*, vol. 12, p. 972, 2016.

[104] E. Galiffi, P. Huidobro, and J. B. Pendry, "Broadband nonreciprocal amplification in luminal metamaterials," *Physical Review Letters*, vol. 123, p. 206101, 2019.

[105] J. Pendry, E. Galiffi, and P. Huidobro, "Gain in time-dependent media—a new mechanism," *JOSA B*, vol. 38, p. 3360, 2021.

[106] M. Lyubarov, Y. Lumer, A. Dikopoltsev, E. Lustig, Y. Sharabi, and M. Segev, "Amplified emission and lasing in photonic time crystals," *Science*, vol. 377, p. 425, 2022.

[107] A. A. Grandi, S. Protière, and A. Lazarus, "Enhancing and controlling parametric instabilities in mechanical systems," *Extreme Mechanics Letters*, vol. 43, p. 101195, 2021.

[108] R. E. Goldstein, "Coffee stains, cell receptors, and time crystals: Lessons from the old literature," *Physics Today*, vol. 71, p. 32, 2018.

[109] G. Teschl, *Ordinary differential equations and dynamical systems*. American Mathematical Soc., 2012.

[110] L. N. Trefethen and M. Embree, *Spectra and Pseudospectra: The Behaviour of Nonnormal Matrices and Operators*. Princeton University Press, 2005.

[111] L. N. Trefethen, A. E. Trefethen, S. C. Reddy, and T. A. Driscoll, "Hydrodynamic stability without eigenvalues," *Science*, vol. 261, p. 578, 1993.

[112] P. J. Schmid, "Nonmodal stability theory," *Annu. Rev. Fluid Mech.*, vol. 39, p. 129, 2007.

[113] B. F. Farrell and P. J. Ioannou, "Generalized stability theory. Part I: Autonomous operators," *Journal of Atmospheric Sciences*, vol. 53, p. 2025, 1996.

[114] G. W. Stewart, "On the early history of the singular value decomposition," *SIAM review*, vol. 35, p. 551, 1993.

[115] N. W. McLachlan, *Theory and Application of Mathieu Functions*. Dover Publications, 1947.

[116] T. T. Koutserimpas, A. Alù, and R. Fleury, "Parametric amplification and bidirectional invisibility in $\mathcal{PT}$-symmetric time-Floquet systems," *Physical Review A*, vol. 97, p. 013839, 2018.

[117] D. Holberg and K. Kunz, "Parametric properties of fields in a slab of time-varying permittivity," *IEEE Transactions on Antennas and Propagation*, vol. 14, p. 183, 1966.

[118] C. M. Bender and S. A. Orszag, *Advanced mathematical methods for scientists and engineers I: Asymptotic methods and perturbation theory*. Springer Science & Business Media, 1999.

[119] A. Merkel, G. Theocharis, O. Richoux, V. Romero-García, and V. Pagneux, "Control of acoustic absorption in one-dimensional scattering by resonant scatterers," *Applied Physics Letters*, vol. 107, 2015.

[120] A.-S. B.-B. Dhia, L. Chesnel, and V. Pagneux, "Trapped modes and reflectionless modes as eigenfunctions of the same spectral problem," *Proceedings of the Royal Society A: Mathematical, Physical and Engineering Sciences*, vol. 474, p. 20180050, 2018.

[121] H. Hernandez-Coronado, D. Krejčiřík, and P. Siegl, "Perfect transmission scattering as a PT-symmetric spectral problem," *Physics Letters A*, vol. 375, p. 2149, 2011.

[122] W.-P. Su, J. R. Schrieffer, and A. J. Heeger, "Solitons in polyacetylene," *Physical Review Letters*, vol. 42, p. 1698, 1979.

[123] R. Chaunsali, E. Kim, A. Thakkar, P. G. Kevrekidis, and J. Yang, "Demonstrating an in situ topological band transition in cylindrical granular chains," *Physical Review Letters*, vol. 119, p. 024301, 2017.

[124] J. Zak, "Berry's phase for energy bands in solids," *Physical Review Letters*, vol. 62, p. 2747, 1989.

[125] X. Shi, I. Kiorpelidis, R. Chaunsali, V. Achilleos, G. Theocharis, and J. Yang, "Disorder-induced topological phase transition in a one-dimensional mechanical system," *Physical Review Research*, vol. 3, p. 033012, 2021.

[126] J. A. Scales and E. S. Van Vleck, "Lyapunov exponents and localization in randomly layered media," *Journal of Computational physics*, vol. 133, p. 27, 1997.

[127] B. M. Manda, V. Achilleos, O. Richoux, C. Skokos, and G. Theocharis, "Wave-packet spreading in the disordered and nonlinear Su-Schrieffer-Heeger chain," *Physical Review B*, vol. 107, p. 184313, 2023.

[128] T. Caneva, T. Calarco, and S. Montangero, "Chopped random-basis quantum optimization," *Physical Review A*, vol. 84, p. 022326, 2011.

[129] T. Caneva, M. Murphy, T. Calarco, R. Fazio, S. Montangero, V. Giovannetti, and G. E. Santoro, "Optimal control at the quantum speed limit," *Physical Review Letters*, vol. 103, p. 240501, 2009.

[130] I. Brouzos, I. Kiorpelidis, F. Diakonos, and G. Theocharis, "Fast, robust, and amplified transfer of topological edge modes on a time-varying mechanical chain," *Physical Review B*, vol. 102, p. 174312, 2020.

[131] M. Devaud, V. Leroy, J.-C. Bacri, and T. Hocquet, "The adiabatic invariant of the n-degree-of-freedom harmonic oscillator," *European Journal of Physics*, vol. 29, p. 831, 2008.

[132] C. Godsil, "State transfer on graphs," *Discrete Mathematics*, vol. 312, p. 129, 2012.

[133] M. Abramowitz and I. A. Stegun, *Handbook of mathematical functions with formulas, graphs, and mathematical tables*. Dover Publications, 1965.

[134] A. H. Nayfeh, *Introduction to perturbation techniques*. Wiley, 1993.

[135] L. Ruby, "Applications of the Mathieu equation," *American Journal of Physics*, vol. 64, p. 39, 1996.

[136] P. J. Schmid and D. S. Henningson, *Stability and Transition in Shear Flows*. Springer, New York, 2001.

[137] T. T. Koutserimpas and R. Fleury, "Electromagnetic waves in a time periodic medium with step-varying refractive index," *IEEE Transactions on Antennas and Propagation*, vol. 66, p. 5300, 2018.

[138] B. F. Farrell and P. J. Ioannou, "Generalized stability theory. Part II: Nonautonomous operators," *Journal of Atmospheric Sciences*, vol. 53, p. 2041, 1996.

[139] M. V. Berry, "Mode degeneracies and the Petermann excess-noise factor for unstable lasers," *Journal of Modern Optics*, vol. 50, p. 63, 2003.

[140] V. Achilleos, Y. Aurégan, and V. Pagneux, "Scattering by finite periodic $\mathcal{PT}$-symmetric structures," *Physical Review Letters*, vol. 119, p. 243904, 2017.

[141] Z.-Q. Zhang, B.-L. Wu, J. Song, and H. Jiang, "Topological Anderson insulator in electric circuits," *Physical Review B*, vol. 100, p. 184202, 2019.

[142] A. MacKinnon and B. Kramer, "The scaling theory of electrons in disordered solids: Additional numerical results," *Zeitschrift für Physik B Condensed Matter*, vol. 53, p. 1, 1983.

Περίληψη

Η αλληλεπίδραση των κυμάτων με μέσα που διαθέτουν χωρικές ή/και χρονικές διακυμάνσεις οδηγεί σε ενδιαφέρουσα φαινομενολογία. Σε αυτό το πλαίσιο, στη παρούσα διατριβή μελετώνται τέσσερα κυματικά φαινόμενα: δύο που εμφανίζονται σε χωρικά μεταβαλλόμενα μέσα και δύο σε χρονικά μεταβαλλόμενα μέσα. Συγκεκριμένα:

Στο κεφάλαιο 1 διερευνούμε την ανθεκτικότητα των συντονισμών πλήρους διέλευσης που υποστηρίζονται σε ένα περιοδικό σύστημα σκέδασης με καθρεπτικά συμμετρικά κελιά, σε ασύμμετρες διαταραχές. Ως πρώτο βήμα, υπολογίζουμε τη διόρθωση στους κυματικούς αριθμούς των προσπιπτόντων κυμάτων που αντιστοιχούν στους συντονισμούς πλήρους διέλευσης (σε πρώτη τάξη θεωρίας διαταραχών). Στη συνέχεια, μελετάμε μια διαταραχή που αποτελείται από σκεδαστές Dirac και δείχνουμε πώς συντονισμοί πλήρους διέλευσης εμφανίζονται και υπό τη παρουσία διαταραχής που έχει κατάλληλα σχεδιαστεί. Τέλος, αποκαλύπτουμε μια σύνδεση μεταξύ δύο φαινομενικά ανεξάρτητων συντονισμών πλήρους διέλευσης του μη διαταραγμένου συστήματος σκέδασης, η οποία οφείλεται στην κατοπτρική συμμετρία των κελιών.

Στο κεφάλαιο 2 υπολογίζουμε το μήκος εντοπισμού των τοπολογικά εντοπισμένων καταστάσεων που υποστηρίζονται σε μια διμερή αλυσίδα μάζας-ελατηρίου η οποία έχει τυχαίες διακυμάνσεις στις σταθερές των ελατηρίων της. Απουσία διαταραχών, η διμερή αλυσίδα που θεωρούμε διαθέτει χειραλική συμμετρία και μη τετριμμένα τοπολογικά χαρακτηριστικά. Υπό την παρουσία ισχυρής χειραλικής διαταραχής το μήκος εντοπισμού των τοπολογικά εντοπισμένων καταστάσεων αποκλίνει, υπονοώντας ότι μια τοπολογική αλλαγή φάσης λαμβάνει χώρα και η οποία προκαλείται αποκλειστικά από τη διαταραχή.

Το μοντέλο που χρησιμοποιούμε στο κεφάλαιο 3 είναι πάλι μια διμερής αλυσίδα μάζας-ελατηρίου. Σε αυτό το κεφάλαιο ωστόσο, χρησιμοποιούμε αυτό το σύστημα σε ένα διαφορετικό πλαίσιο, καθώς ο στόχος μας εδώ είναι να μεταφέρουμε μια τοπολογικά εντοπισμένη κατάσταση από τη μια άκρη της αλυσίδας στην άλλη. Για να επιτύχουμε μια τέτοια μεταφορά επιτρέπουμε στις σταθερές των ελατηρίων να μεταβάλλονται με το χρόνο, καθιστώντας έτσι την αλυσίδα χρονικά μεταβαλλόμενη (η αλυσίδα που χρησιμοποιούμε στο κεφάλαιο 2 είναι στατική). Μας ενδιαφέρει επίσης να επιτύχουμε τη μεταφορά γρήγορα και για το σκοπό αυτό χρησιμοποιούμε μια βέλτιστη μέθοδο ελέγχου. Ξεπερνώντας το αδιαβατικό όριο, σχεδιάζουμε ένα πρωτόκολλο για τις χρονικά μεταβαλλόμενες σταθερές των ελατηρίων που έχει ως αποτέλεσμα μια γρήγορη και ανθεκτική μεταφορά και ακόμη περισσότερο οδηγεί στην ενίσχυση της μεταφερόμενης τοπολογικής κατάστασης.

Για να κατανοήσουμε το φαινόμενο της ενίσχυσης σε μια χρονικά μεταβαλλόμενη πλατφόρμα, στο κεφάλαιο 4 εξετάζουμε τη διάδοση ενός κύματος σε ένα μέσο με χρονικά περιοδικό δείκτη διάθλασης και με δυναμική που διέπεται από την εξίσωση Mathieu. Η εξίσωση Mathieu διαθέτει τόσο ευσταθείς όσο και ασταθείς λύσεις και διερευνούμε την παροδική ενίσχυση των ευσταθών της λύσεών. Αναζητούμε τη μέγιστη δυνατή παροδική ενίσχυση βελτιστοποιώντας στις αρχικές συνθήκες καθώς και στον αρχικό χρόνο. Εξετάζουμε επίσης αρκετές ποσότητες του ϵ-ψευδοφάσματος του μονόδρομου πίνακα – του πίνακα που διαδίδει τις αρχικές συνθήκες σε μία περίοδο – και παρέχουμε αριθμητικά δεδομένα που δείχνουν ότι η μέγιστη δυνατή ενίσχυση καθορίζεται μόνο από τον μονόδρομο πίνακα.

Τέλος, στο κεφάλαιο 5, συνοψίζουμε τα ευρήματά μας και συζητάμε περαιτέρω ερευνητικά ερωτήματα που ανοίγονται. Η παρούσα εργασία συνοδεύεται από τέσσερα παραρτήματα. Κάθε ένα από αυτά τα παραρτήματα αντιστοιχεί σε καθένα από τα τέσσερα κεφάλαια. Ειδικότερα: Στο παράρτημα Α παρέχουμε τις αναλυτικές αποδείξεις ορισμένων σχέσεων που δίνονται στο κεφάλαιο 1. Στο παράρτημα Β δίνουμε ορισμένες λεπτομέρειες σχετικά με τη μέθοδο του πίνακα μεταφοράς που χρησιμοποιούμε στο κεφάλαιο 2. Στο Παράρτημα Γ, αποδεικνύουμε – χρησιμοποιώντας τη μέθοδο WKB – ότι αν οι σταθερές των ελατηρίων της διμερούς αλυσίδας που εξετάζουμε στο κεφάλαιο 3 αλλάζουν αργά στο χρόνο, τότε η μεταφορά της τοπολογικά εντοπισμένης κατάστασης γίνεται με επιτυχία. Τέλος, στο παράρτημα Δ δίνουμε κάποιες εκφράσεις σε κλειστή μορφή, οι οποίες μας βοηθούν να κατανοήσουμε καλύτερα ορισμένα αποτελέσματα που παρουσιάζονται στο κεφάλαιο 4.

Résumé

L'interaction des ondes avec des milieux possédant des fluctuations spatiales et/ou temporelles conduit à une phénoménologie intéressante. Dans ce cadre, dans la présente thèse quatre phénomènes ondulatoires sont étudiés: deux se produisant dans des milieux variant dans l'espace et deux dans des milieux variant dans le temps. Spécifiquement:

Dans le chapitre 1, nous étudions la robustesse aux perturbations asymétriques des résonances de transmission parfaite (PTRs) supportés dans un système de diffusion périodique fini construit à partir d'une cellule à symétrie miroir. En première étape, nous calculons la correction aux nombres d'onde des ondes incidentes qui correspondent à ces PTR (dans la théorie des perturbations du premier ordre). Par la suite, nous considérons une perturbation constituée de diffuseurs de Dirac et montrons comment des PTR pourraient encore apparaître dans le cas perturbé avec une conception appropriée de la perturbation. Enfin, nous révélons une connexion entre deux PTR apparemment indépendants de la configuration non perturbée, qui réside dans la symétrie miroir des cellules.

Dans le chapitre 2, nous calculons la longueur de localisation des modes de bord topologiques qui sont supportés dans une chaîne mécanique masse-ressort possédant des fluctuations aléatoires de ses paramètres de rigidité. En l'absence de désordre, la chaîne dimère que nous considérons présente une symétrie chirale et des caractéristiques topologiques non triviales. En présence d'un fort désordre chiral, la longueur de localisation diverge, ce qui implique une transition de phase topologique induite uniquement par le désordre. Le modèle que nous utilisons au chapitre 3 est encore une fois une chaîne masse-ressort dimère. Cependant, dans ce chapitre, nous utilisons cette configuration sous un angle différent, puisque notre objectif ici est de transférer un état de bord à travers la chaîne. Pour réaliser un tel transfert, nous laissons les couplages des ressorts varier avec le temps, rendant ainsi la chaîne dépendante du temps (la chaîne que nous utilisons au chapitre 2 est statique). Nous cherchons également à effectuer le transfert rapidement, et à cette fin, nous utilisons une méthode de contrôle optimal. Au-delà de la limite adiabatique, nous concevons un protocole pour les couplages variables dans le temps qui aboutit à un transfert rapide et robuste et conduit encore plus à une amplification du mode de bord transféré.

Pour comprendre le phénomène d'amplification dans une plateforme variable dans le temps, nous considérons au chapitre 4 la propagation d'une onde dans un milieu à indice de réfraction périodique et dont la dynamique des ondes est régie par l'équation de Mathieu. L'équation de Mathieu contient à la fois des solutions stables et instables et nous explorons les caractéristiques

d'amplification transitoire de ses solutions stables. Nous recherchons l'amplification transitoire maximale possible en optimisant les conditions initiales ainsi que le démarrage initial du processus. Nous utilisons également plusieurs quantités du ϵ-pseudospectre de la matrice de monodromie – la matrice qui propage les conditions initiales sur une période – et nous fournissons la preuve numérique que les caractéristiques globales d'amplification sont fournies simplement par la matrice de monodromie.

Enfin, dans le chapitre 5, nous résumons nos découvertes et discutons de nos perspectives futures. Cette thèse est accompagnée de quatre annexes. Chacune de ces annexes correspond à chacun des quatre chapitres. En particulier : dans l'annexe A, nous fournissons les preuves analytiques de certaines relations données au chapitre 1. Dans l'annexe B, nous donnons quelques détails concernant la méthode de matrice de transfert que nous utilisons au chapitre 2. Dans l'Annexe C, nous prouvons – en utilisant la méthode WKB – que si les couplages de la chaîne dimère que nous considérons au chapitre 3 varient lentement dans le temps, alors le processus de transfert s'effectue avec succès. Enfin, dans l'Annexe D, nous fournissons des expressions sous forme fermée qui nous aident à mieux comprendre certains résultats présentés au chapitre 4.

Titre : Phénomènes ondulatoires dans des milieux spatiaux ou temporels unidimensionnels

Mots clés : résonances de transmission parfaites, longueur de localisation, transfert non adiabatique, équation de Mathieu, pseudospectrum

Résumé : L'interaction des ondes avec des milieux possédant des fluctuations spatiales et/ou temporelles conduit à une phénoménologie intéressante. Dans ce cadre, dans la présente thèse quatre phénomènes ondulatoires sont étudiés: deux se produisant dans des milieux variant dans l'espace et deux dans des milieux variant dans le temps. Nous commençons par explorer la diffusion des ondes par une configuration spatialement périodique finie sujette à des perturbations. Nous nous concentrons sur les résonances de transmission parfaite (PTR) et nous développons une méthode pour les préserver sous des perturbations asymétriques. L'analyse effectuée révèle une connexion par paire entre les PTR d'une configuration de diffusion spatialement périodique avec des cellules à symétrie miroir. Dans le même contexte de milieux variant spatialement, nous calculons la longueur de localisation des modes de bord topologiques qui sont supportés dans une chaîne mécanique masse-ressort possédant des fluctuations aléatoires de ses paramètres de rigidité. En présence d'un fort désordre chiral, la longueur de localisation diverge, ce qui implique une transition de phase topologique induite uniquement par le désordre.

Dans une prochaine étape, nous considérons le cas où les couplages de la chaîne masse-ressort mécanique varient avec le temps de manière déterministe. Ce système variable dans le temps peut alors servir de plate-forme pour transférer un mode de bord topologique. Au-delà de la limite adiabatique, nous concevons un protocole pour les couplages variables dans le temps qui aboutit à un transfert rapide et robuste et conduit encore plus à une amplification du mode de bord transféré. Pour éclairer le phénomène d'amplification dans une plateforme variable dans le temps, nous explorons la propagation d'une onde dans un milieu à indice de réfraction périodique et dont la dynamique des ondes est régie par l'équation de Mathieu. L'onde présente une amplification transitoire en raison de la nature non normale de la matrice de propagation et nous fournissons la preuve numérique que les caractéristiques d'amplification globales sont fournies simplement par la matrice de monodromie.

Title : Wave phenomena in one-dimensional space or time varying media

Keywords : perfect transmission resonances, localization length, non-adiabatic state transfer, Mathieu equation, pseudospectrum

Abstract : The interaction of waves with media possessing spatial or/and temporal fluctuations leads to interesting phenomenology. Within this framework, in the present thesis four wave phenomena are studied: two occurring in spatially-varying media and two in time-varying media. We begin by exploring wave scattering by a finite spatially-periodic setup that is subject to perturbation. Our focus is on perfect transmission resonances (PTRs) and we develop a method for preserving them under asymmetric perturbations. The performed analysis reveals a pairwise connection between PTRs of a spatially-periodic scattering setup with mirror symmetric cells. In the same context of spatially varying media, we compute the localization length of the topological edge modes that are supported in a mechanical mass-spring chain possessing random fluctuations of its stiffness parameters. In the presence of strong chiral disorder the localization length diverges, implying a topological phase transition that is induced purely by disorder.

As a next step we consider the case where the couplings of the mechanical mass-spring chain vary with time in a deterministic way. Then this time-varying system can serve as a platform for transferring a topological edge mode. Going beyond the adiabatic limit, we design a protocol for the time-varying couplings that results in a fast and robust transfer and even more leads to amplification of the transferred edge mode. To shed light into the phenomenon of amplification in a time-varying platform, we explore the propagation of a wave in a medium with time-periodic refractive index and with wave dynamics governed by the Mathieu equation. The wave exhibits transient amplification due to the non normal nature of the propagator matrix and we provide numerical evidence that the global amplifying features are provided merely by the monodromy matrix.